Microwave Measurement System for Breast Cancer Imaging: An Experimental Prototype Towards Time-Domain Inverse Scattering

by

Lin M.C. van Nieuwstadt

A dissertation submitted in partial fulfillment
of the requirements for the degree of
Doctor of Philosophy
(Electrical Engineering)
in The University of Michigan
2011

Doctoral Committee:

Professor Mahta Moghaddam, Co-Chair
Professor Christopher Ruf, Co-Chair
Professor Paul Carson
Assistant Professor Anthony Grbic

To my family

ACKNOWLEDGEMENTS

I owe much of the accomplishments of this doctoral degree to my family and friends, and to my advisors, mentors, colleagues, and fellow graduate student cohorts at the University of Michigan. This endeavor began with the motivation to contribute towards the progress in developing a safer and less expensive breast cancer detection method. It took the technical guidance and patience of my advisor, Professor Mahta Moghaddam, as well as the guidance of Professors Paul Carson and Christopher Ruf to achieve this dissertation research. I am grateful for my colleagues David Boprie and Steven Rogacki at Space Physics Research who helped me fabricate and test the experimental hardware. My fellow graduate student friends and post-doctoral fellows have given generous hours of their time to help and encourage me, including Maha Ali, Steven Clarkson, Xueyang Duan, Adel Elsherbini, Mario Fabiilli, Yuriy Goykhman, Mark Haynes, Ju Seop Lee, John Stang, Mehrnoosh Vahidpour, Jacqueline Vitaz, and Clare Ward.

I would like to acknowledge the NASA Harriett G. Jenkins Pre-doctoral Fellowship Program for providing three years of financial support. I am also grateful for the financial support of the University of Michigan Center for the Education of Women (CEW), Rackham Graduate School, Electrical Engineering Computer Science Department, and the National Science Foundation CBET Program within the Engineering Directorate.

The uniquely personal nature of the doctoral dissertation is such that it would not have been possible for me to succeed without the support of my family and friends. The love and unconditional backing of my husband Michiel have been central to my emotional and mental well-being. The love and boundless energy of my children Tara, Saskia, and Koen

provided daily reminders of my priorities. As for my parents, their gift of an unburdened childhood helped form the resilience and confidence I needed to persist in completing this doctoral degree. At the risk of omitting names, I would like to attempt to acknowledge our friends who have journeyed with us these past five years: the Campbell-Massell family, the Dorje-Tsering family, the Galia family, the van Megen family, the Naik-Desai family, the Semer family, the Torres family, and the Tremonti family. My gratitude goes to our friends who have shared with us family dinners, morning walks, and miles of carpool rides. I share the achievements of this doctoral degree with all of you.

TABLE OF CONTENTS

LIST OF FIGURES

Figure

CHAPTER 1

Introduction

Detection of malignant breast tumors at their earliest stage, when they are less than 5mm in diameter, remains a challenge. Microwave imaging at frequencies of 1-4 GHz seeks to address the limitations of the existing detection modalities, which include X-ray mammography, ultrasound, and magnetic resonance imaging (MRI) and all their various imaging modes.. The challenge of imaging at these frequencies, however, is resolving tumors when they are 5mm or smaller. A microwave imaging algorithm under development at the University of Michigan shows the potential to achieve this resolution with a time-domain inverse scattering technique. This thesis research seeks to validate for the first time several key components of the experimental system to support this imaging approach, including the system analytic design, experimental implementation, and data acquisition.

The specific contributions of this dissertation are the design and development of such a system through:

1. The construction of a numerical system sensitivity analysis tool. A practical system analysis tool, capable of fast system dynamic range computation, has been lacking in the field of microwave breast imaging [4].

2. The design and demonstration of a low-dispersion ultra wideband (UWB) antenna as a critical component of a recently developed 3D time-domain non-linear super-

resolution inverse scattering imaging technique. With the numerous UWB antenna research efforts on-going, the study of phase linearity over the wide operating frequency has previously not been specifically presented [5].

3. Development of biologically compatible matching media for optimum coupling of antenna source signals to imaging targets [6].

4. Integration of the above elements into a representative laboratory-based measurement system, to demonstrate the feasibility of the UWB microwave imaging measurements and their sensitivities [7].

The overall objective is the proof-of-concept for a high-fidelity measurement of the scattered waves due to a transmitted ultra-wideband microwave signal, traveling through a 'microwave tissue-mimicking' environment including a matching medium and tumor-like phantoms.

A microwave imaging (MWI) system offers the potential for specific diagnosis of malignant versus benign tumors, at energy levels that do not induce harm to tissues, and at lower cost than the currently widely used diagnostic tools. In a microwave image, the difference between malignant and benign tumors is quantified based on the difference in permittivity values of these two types of tissues. This potential ability to remotely distinguish between malignant and benign tumors could possibly find cancers earlier and reduce the number of invasive biopsies. The other potential benefit of a MWI diagnostic system is access to early breast cancer detection for a larger segment of the population due to its lower equipment cost. The highly competitive commercial radio frequency (RF) electronics industry has helped push down the prices of electronic devices, including the components that would be used to mass produce these MWI systems.

MWI systems seek to address the limitations of today's standard techniques for breast cancer detection: X-ray mammography, ultrasound (US), and magnetic resonance imaging (MRI). In the case of X-ray mammography, this diagnostic tool poses the potentially

significant health risk of delivering ionizing radiation to breast tissues as discussed in a recently published reports by the U.S. Preventive Services Task Force [1] [8]. Results of this study, weighing the risks of exposure to X-ray radiation versus benefits of early breast cancer detection, recommends, controversially, that mammogram screening should start bi-annually when women reach the age of 50 rather than 40. They argue that the risk of cumulative exposure to X-rays over the additional ten years between ages 40 and 50, may not outweigh the benefit of early breast cancer detection for this age group. This recommendation is in-line with the World Health Organization's recommendation of annual/bi-annual mammograms starting at the age of 50, but it is strongly debated by many other organizations (American Cancer Society 2003 recommendation, Canadian Task Force on Preventive Health Care 2001 recommendation, American College of Obstretrics and Gynecology 2003 recommendation, American College of Radiology and Society of Breast Imaging) [9]. Such discrepancies in X-ray screening recommendations motivate the research to develop imaging methods that would eliminate the radiation exposure risk factor. Further, mammography suffers from a high rate of false positives (see Figure 1.1) resulting in only about 10% of positive biopsies in this age group and of low sensitivity in dense breasts. Other drawbacks of mammography - pain associated with breast compression during procedure, anxiety and distress over false positive results - are considered temporary and only a modest a deterrent for patient's use of this diagnostic tool.

In the case of ultrasound, the images contain too many artifacts and ambiguities (such as shadowing, speckle, and non-quantified contrasts). These issues often result in insufficient effective resolutions, as well as a lack of specificity in distinguishing malignant and benign masses, and distinguishing between normal background tissue and suspected masses. Furthermore, in standard ultrasound, which, in the United States, is typically used as a secondary diagnostic tool for suspicious mammograms, the image quality and interpretations are highly operator-dependent. In the case of MRI, the main disadvantage is its operating cost, with annual maintenance and cryogens of perhaps 15% of its purchase price, plus nu-

Table 2. **Age-Specific Screening Results From the BCSC**

Screening Result	Age Group				
	40–49 y	50–59 y	60–69 y	70–79 y	80–89 y
Outcomes per screening round (per 1000 screened), *n**					
False-negative mammography result	1.0	1.1	1.4	1.5	1.4
False-positive mammography result	97.8	86.6	79.0	68.8	59.4
Additional imaging	84.3	75.9	70.2	64.0	56.3
Biopsy	9.3	10.8	11.6	12.2	10.5
Screening-detected invasive cancer	1.8	3.4	5.0	6.5	7.0
Screening-detected DCIS	0.8	1.3	1.5	1.4	1.5
Yield of screening per screening round, *n*					
Patients undergoing mammography to diagnose 1 case of invasive breast cancer†	556	294	200	154	143
Patients undergoing additional imaging to diagnose 1 case of invasive breast cancer‡	47	22	14	10	8
Patients undergoing biopsy to diagnose 1 case of invasive breast cancer§	5	3	2	2	1.5

BCSC = Breast Cancer Surveillance Consortium; DCIS = ductal carcinoma in situ.
* Calculated from BCSC data of regularly screened women on the basis of results from a single screening round. Rates of additional imaging and biopsies may be underestimated because of incomplete capture of these examinations by the BCSC.
† 1 per rate of screening-detected invasive cancer.
‡ Rate of additional imaging per rate of screening-detected invasive cancer.
§ Rate of biopsy per rate of screening-detected invasive cancer.

Figure 1.1: Age Specific Screening Results [1]

merous trained staff per patient. The long examination time and use of contrast agent also do not meet traditional standards of screening devices. This may be true for the high risk (1-2% incidence) group in which it is now recommended, or the 0.5% of that group which might not be detected as soon by mammography plus ultrasound. The advantage of MRI over alternative imaging might disappear completely in high risk patients when high resolution microwave imaging is included with mammography plus ultrasound. When applied to breast cancer detection, currently MRI suffers from a rather high rate of false positive diagnosis. MRI machines remain expensive to procure and require substantial infrastructure (such as space, ventilation, and floor support) to set up. Access to this imaging tool is rather limited and may result in delay in time for testing.

Chapter 2 of this dissertation introduces the background and motivation for pursuing studies in MWI as it is applied to early breast cancer detection. On-going research studies in the field of MWI for breast cancer detection are described, with the emphasis on the 3D super-resolution time domain inverse scattering imaging technique being pursued at the

University of Michigan. As the objective is to implement a prototype experimental system, the research work must begin with the determination of the system parameters. Chapter 3 describes a system sensitivity analysis tool that uses the aggregate T-matrix recursive algorithm to model the gross characteristics of the forward scattering process for the UWB system. Optimum system design parameters are quantified with this model through a series of simulations over a wide range of relevant hardware and target parameters. With the system parameters such as operating frequency range, expected system dynamic range, and useful ranges of view angles specified, the critical components of the hardware system can be developed. One major component is the UWB antennas, to be used both as signal source radiating elements and the receiver of scattered waves. The UWB antennas are described in Chapter 4. Chapter 5 describes the next major component - the coupling medium, designed to maximize signal coupling from the antenna radiating elements to the breast tissues. Optimum source signal coupling to the breast tissue is essential if any signal scattered off of malignant tumors inside the breast tissue is to be detected. Chapter 6 describes the integrated imaging system experimental set up and presents measurement data. Lastly, chapter 7 concludes the thesis with research topic proposals for future work.

CHAPTER 2

Overview of Microwave Imaging Applied to Breast Cancer Detection

2.1 Dielectric Properties Contrast Study

The application of MWI to breast cancer detection rests on the premise that there exists a detectable contrast between the relative permittivity of malignant breast tissues and normal breast tissues at microwave frequencies. Numerous studies of the electromagnetic dielectric properties of biological tissues at microwave frequencies have shown that the dielectric constant contrast between malignant and benign breast tissues is sufficient to suggest MWI as a useful diagnostic tool for early stage breast cancer detection [10] [11] [12] [13] [14] [15] [16] [17] [18]. These earlier studies suggest the contrast in dielectric constant and conductivity between benign and malignant breast tissues is at least an order of magnitude, see Figure 2.1. Only one *in-vitro* study of measurements done at 3.2 GHz [13] suggested that *in-vivo* imaging would not be able to distinguish between the dielectric properties of benign and malignant tissues. However, later studies suggested that the dielectric constant contrast between malignant and benign tumors is closer to 1.5:1 ratio [3] [19] [20].

One recent study in particular [3], involved a large sample of benign breast tissues

acquired during breast reduction surgeries. The study involved 93 patients and collected measurements from over 400 benign tissue samples, with dielectric constant data measured in the 0.5-20 GHz frequency range. Results of this study show the wider range in normal tissue dielectric properties. The dielectric heterogeneity of the breast tissues was found to be larger than that reported by earlier studies. As data in Figure 2.2 show, the dielectric properties of normal tissues have a wide range of values depending on tissue type. The solid lines show dielectric properties of 85-100% adipose tissues, while the top lines show 0-30% and 31-84% adipose tissues. The system analysis simulations done for this dissertation work use data for the lower adipose content tissues, more common in the older women screened more consistently. Data in Figures 2.1 and 2.2 do show agreement - note that the contrast between the malignant tissues dielectric properties and the recently measured benign tissues dielectric properties in Figure 2.2 is smaller than previously reported by [16]. The primary reason is that the spread in dielectric property values of the benign tissues is wider than previously reported.

Most human breast tissue data were measured *in-vitro*, with one non-invasive *in-vivo* MWI system operating at 900MHz [21]; however, this study did not look at the dielectric contrast between malignant and benign tissue. With practically all breast tissue dielectric contrast studies done *in-vitro*, the question is whether this dielectric constant contrast would be distinguishable in *in-vivo* MWI measurements. At least one study [6] has looked into this question with animal subjects. Their findings reported no significant difference between *in-vitro* and *in-vivo* dielectric constant measurements for frequencies above 1GHz. Observed dielectric properties differences were within their experimental error of 3%. Planned future research at the University of Michigan will attempt to answer this question through *in-situ* dielectric constant measurements during needle-core breast biopsy procedures, which is outlined in Chapter 7.

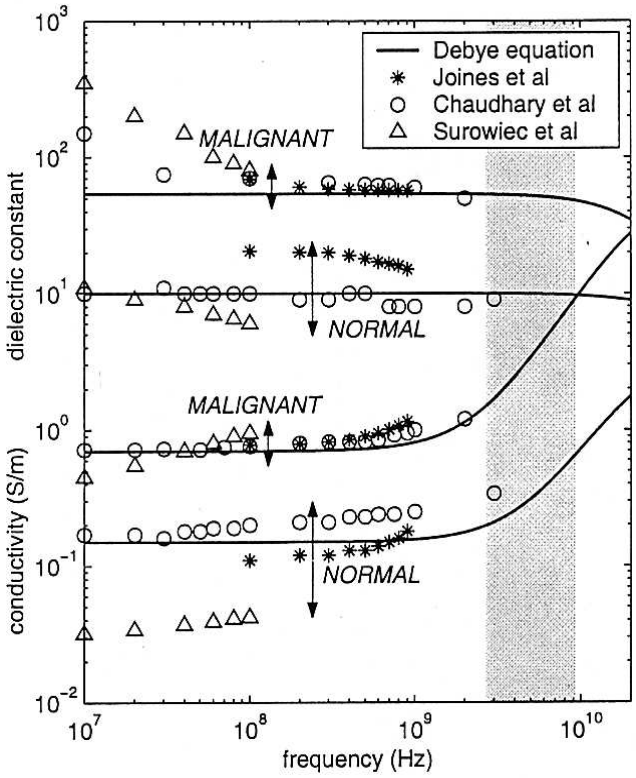

Figure 2.1: Measured dielectric properties of malignant and normal breast tissues, *in vitro* (single-pole Debye curve fits) [2].

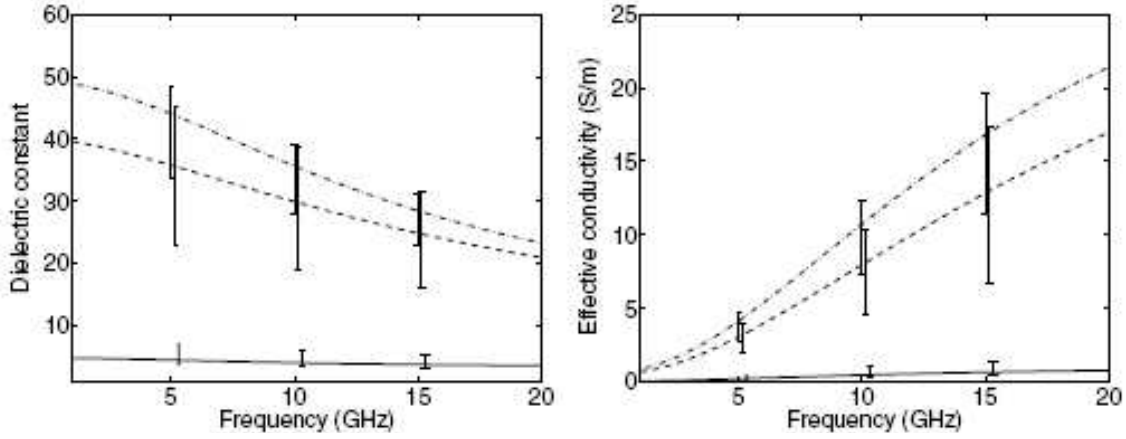

Figure 2.2: Measured dielectric properties of normal breast tissues [3].

2.2 Progress of Microwave Imaging Systems

Proceeding on the assumption that MWI techniques will be able to distinguish between malignant and benign breast tissues, many active and passive MWI systems have been proposed [22] [23] [24] [25] [21] [26] [27] [28] [18] [19] [29]. Most systems have focused on active microwave imaging techniques. Each of these systems carries its own set of limitations, which motivates the research effort resulting in the contributions presented in this dissertation.

One microwave imaging system developed at Dartmouth College has been used in clinical experiments [21] [30] [31] [32]. Using a microwave tomographic imaging technique, the system is built with an array of monopole antennas operating in the 300-1300 MHz range, mounted on a 15cm diameter ring inside an imaging tank filled with coupling fluid. Patients are positioned lying face down, prone position, with breasts submerged inside imaging tank filled with the coupling liquid. Their 2007 report detailed that their coupling fluid is composed of water-glycerin mixture. They have shown only coarse mapping of the breast's dielectric properties to date. They are currently exploring system studies at higher frequencies in an attempt to refine their image resolution. They further reported that at frequencies higher than their current 1300MHz operating frequency, they will need to formulate a more suitable coupling liquid. Measured data of the water-glycerin mixture shown in Figures 5.20 and 5.21 (taken as part of the coupling medium development work within this dissertation) verified the Darthmouth group's concerns over the nonlinear increase in conductivity as frequency increases. The coupling medium developed in this thesis seeks to meet the need for a suitable microwave breast imaging matching liquid. Another tomographic imaging technique proposed by Northeastern University uses ultra wideband pulse illuminations in order to achieve sub-millimeter target resolution and a time-reversal finite-difference time-domain (FDTD) algorithm to generate the 3D microwave image [33] [34]. To date, there has been no known experimental validation of this imaging technique. A third group at Duke University has developed experimental validation [35] for their inverse scat-

tering imaging technique [36] [37] [38] - which uses the biconjugate-gradient fast Fourier transform algorithm for their forward model. The inverse scattering problem is solved at various discrete frequencies - 800MHz, 3GHz and 6GHz. Their focus is on the ability to invert high contrast dielectric properties in the breast tissue and resolve sub-millimeter malignant lesions. While they showed the ability to resolve high contrast dielectric properties (contrast of 3:1), recent studies into the contrast in dielectric properties between malignant and benign tumors suggest that dielectric contrast may be as low as 1.5:1 between the two types of tissues.

Another group of imaging techniques proposed by the Universities of Wisconsin, Calgary and Victoria, uses the confocal imaging technique [2] [29]. This UWB radar technique uses FDTD methods to compute the signal backscatter from scattering targets illuminated by ultra wideband pulses, with both cases of supine and prone positioning of the patient considered. From this starting point, two research directions emerged.

The first is microwave imaging via space-time beamforming (MIST) [22] [23] [24] pursued at the University of Wisconsin, and then later at Northernwestern University. The second technique, tissue sensing adaptive radar (TSAR) [39] [40] is being pursued by the group at the University of Calgary. With the MIST system, the objective is to identify the presence and location of the malignant tumors by processing the backscatter ultra wideband received signals illuminated at scattering tumor objects. A post-processing beamformer is used to coherently and incoherently delay-and-sum the received scattered signal: the coherently summed signal would identify the location of the scattering object. With this technique a strong contrast in dielectric constants of target objects is assumed. However, recent studies reveal that contrast between malignant (generally higher permittivity values) and benign (generally lower permittivity values) tissue is not as large as earlier suggested. MIST backscattered signal maps would face the challenge of providing specificity of the imaged objects - dense benign tissues residing adjacent to fatty tissue could be interpreted as malignant tissue.

The TSAR system pursued at the University of Calgary focuses on late-time signal clutter noise reduction techniques [39] [40] [41]. The objective here is to filter out the skin effects by employing an adaptive correlation method combined with a recursive least squares filter algorithm. For both the MIST and TSAR experimental systems, oil is used for the coupling medium, which presents a rather large permittivity mismatch at the oil-skin interface (permittivity contrast of $\sim 2:35$ for oil and skin, respectively). With the TSAR operating frequency covering the range of 1-10 GHz, the effect of 1-2mm skin thickness must be taken into account. Second generation experimental validation is on-going at Calgary, to continue to improve signal clutter problem through skin effect substraction.

At the University of Michigan, the 3D non-linear time-domain super resolution inverse scattering imaging technique developed in [42] has shown simulated resolutions of less than 5mm using the frequency band of 0.8-3 GHz. The objective of this technique to generate dielectric properties map of the breast, with the desired resolution of better than 5mm for early stage cancer detection. The particular contribution of this dissertation work is to provide the an experimental setup and proof of concept data collection scheme that will lead to validation of this time-domain super resolution imaging technique. This image reconstruction method solves the non-linear integral equation of scattered field using Born-type iterations and time-domain data. It shows the ability to resolve dielectric contrast as low as 10% and target sizes smaller than 5mm. This promising result motivates the fabrication of the hardware experimental system. The MWI system built here shows the feasibility of collecting the necessary data for this high-resolution imaging technique. While the data collected by this system have not yet been used with the imaging algorithm to form an image, it has been shown that the data with required properties can be produced.

CHAPTER 3

System Sensitivity Analysis

Prerequisite to any systematic development of a remote sensing instrument is the development of a simulation tool for a comprehensive parametric trade-off study. In particular, the following parameters are considered in generating the design trade space: tissue dielectric constant contrast (malignant vs. benign tumors); signal attenuation through target tissues; frequency band of operation; polarization of source and scattered fields; range of observation angles (i.e., locations of transmitters and receivers); location and number/density of potential tumors (single vs. multiple tumors in clusters and dispersed). The motivation for developing the system simulator, a 3D forward solver, is versatility and fast system response, enabling a computationally feasible simulation of scattering in a 3D region that is several wavelengths in each dimension.

The 3D forward solver generates expected scattered field strengths due to random or patterned clusters of spheres embedded inside a homogeneous background. The solver is built with multiple spheres arranged in meaningful combinations and locations to approximate the tumors. Although tumors are generally not spherical, a collection of spheres can be used to approximate the arbitrary shapes of lesions. Using spheres as building blocks for the target tumors allows the forward solver to use the T-matrix (Transition matrix) recursive algorithm [43].

3.1 The T-matrix for single sphere scattering

The development of the system simulator model begins with the case of a single dielectric sphere scatterer, using the T-matrix technique. The T-matrix is defined by [44]

$$\bar{E}^{scat} = \bar{\bar{T}} \cdot \bar{E}^{inc} \tag{3.1}$$

The task now is to derive an expression for the 3D vector T-matrix for spherical waves so to be able to calculate the scattered fields due to known incident fields. Derivation starts with the Helmholtz wave equation in spherical coordinates and then employs the Debye potentials notation to arrive at the expressions for the electric and magnetic fields. The Helmholtz wave equation states

$$(\nabla^2 + k^2)\Psi(r,\theta,\phi) = 0 \tag{3.2}$$

In the spherical coordinate system, the wave equation takes the form

$$\frac{1}{r^2}\frac{\partial}{\partial r}(r^2\frac{\partial \Psi}{\partial r}) + \frac{1}{r^2\sin\theta}\frac{\partial}{\partial \theta}(\sin\theta\frac{\partial \Psi}{\partial \theta}) + \frac{1}{r^2\sin\theta}\frac{\partial^2 \Psi}{\partial \phi^2} + k^2\Psi = 0 \tag{3.3}$$

with the elementary spherical wave function in the form of [45]

$$\Psi(r,\theta,\phi) = \begin{cases} j_n(kr) \\ h_n(kr) \end{cases} \quad P_n^m(\cos\theta)e^{im\phi} \tag{3.4}$$

Expressing the wave equation in terms of a magnetic vector potential $\bar{A}$ and electric vector potential $\bar{F}$

$$(\nabla^2 + k^2)\frac{\bar{A}}{r} = 0 \tag{3.5}$$

and

$$(\nabla^2 + k^2)\frac{\bar{F}}{r} = 0, \tag{3.6}$$

the electric and magnetic fields can then be found in terms of the Debye potentials:

$$\bar{E} = \nabla \times (\bar{r}\pi_m) - \frac{1}{i\omega\varepsilon}\nabla \times \nabla \times (\bar{r}\pi_e) \tag{3.7}$$

$$\bar{H} = \nabla \times (\bar{r}\pi_e) + \frac{1}{i\omega\mu}\nabla \times \nabla \times (\bar{r}\pi_m) \tag{3.8}$$

with the Debye potentials defined as $\bar{r}\pi_m = \bar{F}$ and $\bar{r}\pi_e = \bar{A}$.

From equations (3.7) and (3.8), the components of the fields are found to be:

$$\bar{E}_r = \frac{i}{\omega\varepsilon}\left(\frac{\partial^2}{\partial r^2} r\pi_e + k^2 r\pi_e\right) \tag{3.9}$$

$$\bar{E}_\theta = \frac{i}{\omega\varepsilon}\frac{1}{r}\frac{\partial^2}{\partial r \partial\theta} r\pi_e + \frac{1}{\sin\theta}\frac{\partial}{\partial\phi}\pi_m \tag{3.10}$$

$$\bar{E}_\phi = \frac{i}{\omega\varepsilon}\frac{1}{r\sin\theta}\frac{\partial^2}{\partial r \partial\phi} r\pi_e - \frac{\partial}{\partial\theta}\pi_m \tag{3.11}$$

$$\bar{H}_r = -\frac{i}{\omega\mu}\left(\frac{\partial^2}{\partial r^2} r\pi_m + k^2 r\pi_m\right) \tag{3.12}$$

$$\bar{H}_\theta = -\frac{i}{\omega\mu}\frac{1}{r}\frac{\partial^2}{\partial r \partial\theta} r\pi_m + \frac{1}{\sin\theta}\frac{\partial}{\partial\phi}\pi_e \tag{3.13}$$

$$\bar{H}_\phi = -\frac{i}{\omega\mu}\frac{1}{r\sin\theta}\frac{\partial^2}{\partial r \partial\phi} r\pi_m - \frac{\partial}{\partial\theta}\pi_e \tag{3.14}$$

Consider now a plane wave incident onto a dielectric sphere located at the origin. For convenience of applying boundary conditions at the surface of the spherical scatterer, following the spherical geometry of scattering objects, the incident plane wave is expanded in terms of spherical wave functions:

$$E^{inc} = \hat{x}E_0 e^{ikz} = \hat{x}E_0 e^{ikr\cos\theta} = \hat{x}E_0 \sum_{n=0}^{\infty} (-i)^{-n}(2n+1) j_n(kr) P_n(\cos\theta) \tag{3.15}$$

The incident wave is arbitrarily x-directed, traveling in the z-direction. Re-writing the incident fields in terms of their Debye potentials:

$$\pi_e^{inc} = -\frac{E_0 \cos\phi}{\omega\mu r} \sum_{n=1}^{\infty} \frac{(-i)^{-n}(2n+1)}{n(n+1)} \hat{J}_n(kr) P_n^1(\cos\theta) \tag{3.16}$$

$$\pi_m^{inc} = \frac{E_0 \sin\phi}{kr} \sum_{n=1}^{\infty} \frac{(-i)^{-n}(2n+1)}{n(n+1)} \hat{J}_n(kr) P_n^1(\cos\theta) \tag{3.17}$$

Similarly, the scattered fields can be expressed in terms of their Debye potentials:

$$\pi_e^{scat} = -\frac{E_0 \cos\phi}{\omega\mu r} \sum_{n=1}^{\infty} a_n \hat{H}_n(kr) P_n^1(\cos\theta) \tag{3.18}$$

$$\pi_m^{scat} = \frac{E_0 \sin\phi}{kr} \sum_{n=1}^{\infty} b_n \hat{H}_n(kr) P_n^1(\cos\theta) \tag{3.19}$$

where $\hat{J}_n(kr) = krj_n(kr)$ and $\hat{H}_n(kr) = krh_n(kr)$

Inserting the Debye potentials into equations (3.9) to (3.14), for the incident and scattered fields, results in:

$$\bar{E}_r^{inc} = \frac{i}{\omega\varepsilon}\left(-\frac{E_0 \cos\phi}{\omega\mu}\right)k^2 \sum_{n=1}^{\infty} W_n[\hat{J}_n''(kr) + \hat{J}_n(kr)] P_n^1(\cos\theta) \tag{3.20}$$

$$\begin{aligned}\bar{E}_\theta^{inc} = {} & \frac{i}{\omega\varepsilon}\left(-\frac{E_0 \cos\phi}{\omega\mu r}\right)k \sum_{n=1}^{\infty} W_n \hat{J}_n'(kr) \frac{(n\cos\theta P_n^1(\cos\theta) - (n+1)P_{n-1}^1(\cos\theta))}{\sqrt{1-\cos^2\theta}} \\ & + \frac{1}{\sin\theta}\frac{E_0 \cos\phi}{kr} \sum_{n=1}^{\infty} W_n \hat{J}_n(kr) P_n^1(\cos\theta)\end{aligned} \tag{3.21}$$

$$\begin{aligned}\bar{E}_\phi^{inc} = {} & \frac{i}{\omega\varepsilon}\frac{1}{\sin\theta}\left(\frac{E_0 \sin\phi}{\omega\mu r}\right)k \sum_{n=1}^{\infty} W_n \hat{J}_n'(kr) P_n^1(\cos\theta) \\ & - \left(\frac{E_0 \sin\phi}{kr}\right) \sum_{n=1}^{\infty} W_n \hat{J}_n(kr) \frac{(n\cos\theta P_n^1(\cos\theta) - (n+1)P_{n-1}^1(\cos\theta))}{\sqrt{1-\cos^2\theta}}\end{aligned} \tag{3.22}$$

$$\bar{E}_r^{scat} = \frac{i}{\omega\varepsilon}\left(-\frac{E_0 \cos\phi}{\omega\mu}\right)k^2 \sum_{n=1}^{\infty} a_n[\hat{H}_n^{(1)\prime\prime}(kr) + \hat{H}_n(kr)] P_n^1(\cos\theta) \tag{3.23}$$

$$\bar{E}_{\theta}^{scat} = \frac{i}{\omega\varepsilon}(-\frac{E_0\cos\phi}{\omega\mu r})k\sum_{n=1}^{\infty} a_n\hat{H}_n^{(1)\prime}(kr)\frac{(n\cos\theta P_n^1(\cos\theta)-(n+1)P_{n-1}^1(\cos\theta))}{\sqrt{1-\cos^2\theta}} + \frac{1}{\sin\theta}\frac{E_0\cos\phi}{kr}\sum_{n=1}^{\infty} b_n\hat{H}_n^{(1)}(kr)P_n^1(\cos\theta) \tag{3.24}$$

$$\bar{E}_{\phi}^{scat} = \frac{i}{\omega\varepsilon}\frac{1}{\sin\theta}(\frac{E_0\sin\phi}{\omega\mu r})k\sum_{n=1}^{\infty} a_n\hat{H}_n^{(1)\prime}(kr)P_n^1(\cos\theta) - (\frac{E_0\sin\phi}{kr})\sum_{n=1}^{\infty} b_n\hat{H}_n^{(1)}(kr)\frac{(n\cos\theta P_n^1(\cos\theta)-(n+1)P_{n-1}^1(\cos\theta))}{\sqrt{1-\cos^2\theta}} \tag{3.25}$$

where

$$W_n = \frac{(-i)^{-n}(2n+1)}{n(n+1)} \tag{3.26}$$

Applying boundary conditions on the surface of the dielectric sphere, coefficients a_n and b_n are found to be:

$$a_n = W_n\frac{-\sqrt{\varepsilon_s\mu}\hat{J}'_n(ka)\hat{J}_n(k_sa)+\sqrt{\varepsilon\mu}\hat{J}_n(ka)\hat{J}'_n(k_sa)}{\sqrt{\varepsilon_s\mu}\hat{H}'_n(ka)\hat{J}_n(k_sa)-\sqrt{\varepsilon\mu}\hat{H}_n(ka)\hat{J}'_n(k_sa)} \tag{3.27}$$

$$b_n = W_n\frac{-\sqrt{\varepsilon_s\mu}\hat{J}_n(ka)\hat{J}'_n(k_sa)+\sqrt{\varepsilon\mu}\hat{J}'_n(ka)\hat{J}_n(k_sa)}{\sqrt{\varepsilon_s\mu}\hat{H}_n(ka)\hat{J}'_n(k_sa)-\sqrt{\varepsilon\mu}\hat{H}'_n(ka)\hat{J}_n(k_sa)} \tag{3.28}$$

where

k_s = wave number of dielectric sphere

k = wave number of background

$\mu = \mu_0$

a = diameter of dielectric sphere

Since the T-matrix is defined to be $\bar{E}^{scat} = \bar{\bar{T}}\cdot\bar{E}^{inc}$, the single sphere scattering T-matrix is essentially the first two Mie scattering coefficient, or

$$\bar{\bar{T}}_e = \text{diag}\left\{\frac{-\sqrt{\varepsilon_s\mu}\hat{J}'_n(ka)\hat{J}_n(k_sa)+\sqrt{\varepsilon\mu}\hat{J}_n(ka)\hat{J}'_n(k_sa)}{\sqrt{\varepsilon_s\mu}\hat{H}'_n(ka)\hat{J}_n(k_sa)-\sqrt{\varepsilon\mu}\hat{H}_n(ka)\hat{J}'_n(k_sa)}\right\} \tag{3.29}$$

$$\bar{\bar{T}}_m = \text{diag}\left\{ \frac{-\sqrt{\varepsilon_s\mu}\hat{J}_n(ka)\hat{J}'_n(k_sa) + \sqrt{\varepsilon\mu}\hat{J}'_n(ka)\hat{J}_n(k_sa)}{\sqrt{\varepsilon_s\mu}\hat{H}_n(ka)\hat{J}'_n(k_sa) - \sqrt{\varepsilon\mu}\hat{H}'_n(ka)\hat{J}_n(k_sa)} \right\} \tag{3.30}$$

The single sphere scattering forward model was implemented using both Matlab and F90, carrying the assumption that the incident E-field is in the form of plane waves.

3.2 Multiple scattering: 3D-vector T-matrix

The system simulator modeling tool was then extended to the case of multiple spheres, employing a 3D-vector T-matrix technique [46] [47], based on the scalar derivation in [43]. First, the coordinate system is reviewed, as presented in Figure 3.1. The vector $\bar{r}$ locates the observation point. It is assumed that the background environment is homogeneous. In formulating the solution for multiple scatterers, the observation point is assumed to be farther away from the system's origin than any of the individual scatterers. For each scatterer, the single sphere solution applies for a scatterer located at the origin of coordinate system as was derived above, or

$$\pi_e^{scat} = -\frac{E_0 \cos\phi}{\omega\mu r} \sum_{n=1}^{\infty} Te_n W_n \hat{H}_n(kr) P_n^1(\cos\theta) \tag{3.31}$$

$$\pi_m^{scat} = \frac{E_0 \sin\phi}{kr} \sum_{n=1}^{\infty} Tm_n W_n \hat{H}_n(kr) P_n^1(\cos\theta) \tag{3.32}$$

where $\hat{J}_n(kr) = krj_n(kr)$ and $\hat{H}_n(kr) = krh_n(kr)$. For each scatterer placed at locations $\bar{r}_2$ ... $\bar{r}_q$, the Addition Theorem is applied.

At this point, the spherical Addition Theorem is reviewed for completeness. The Addition Theorem states:

$$\hat{H}_0(k \mid r - r_1 \mid) = \sum_{n=1}^{\infty} (2n+1) \begin{cases} \hat{J}_n(kr_1)\hat{H}_n(kr)P_n(\cos\xi) & \text{for } r_1 < r \\ \hat{H}_n(kr_1)\hat{J}_n(kr)P_n(\cos\xi) & \text{for } r < r_1 \end{cases} \tag{3.33}$$

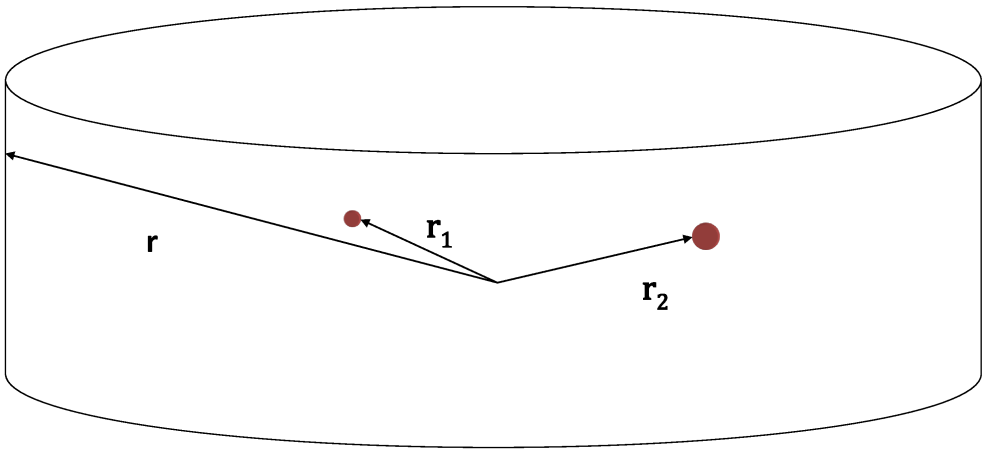

Figure 3.1: Multiple Scattering Coordinate Definition.

where

$$P_n(\cos\xi) = \sum_{m=1}^{n} \varepsilon_m \frac{(n-m)!}{(n+m)!} P_n^m(\cos\theta) P_n^m(\cos\theta_1)\cos m(\phi-\phi_1) \tag{3.34}$$

$$\varepsilon_m = \begin{cases} 1, & m = 0 \\ 2, & m > 0 \end{cases} \tag{3.35}$$

Since $\bar{r}_1 < \bar{r}$ the solution for the single scatterer located at $\bar{r}_1$ is then:

$$\pi_{e_{r1}}^{scat} = -\frac{E_0\cos\phi}{\omega\mu r} \sum_{n=1}^{\infty} Te_{1(1)_n} W_n(2n+1)\hat{J}_n(kr_1)\hat{H}_n(kr)P_n(\cos\xi) \tag{3.36}$$

Similarly, if a scatterer is located at $\bar{r}_2$ then its single sphere solution is given by:

$$\begin{aligned} \pi_{e_{r2}}^{scat} = &-\frac{E_0\cos\phi}{\omega\mu r} \sum_{n=1}^{\infty} Te_{2(1)_n} W_n(2n+1)\hat{J}_n(kr_1)\hat{H}_n(kr) \\ &\sum_{m=1}^{\infty} \varepsilon_m \frac{(n-m)!}{(n+m)!} P_n^m(\cos\theta) P_n^m(\cos\theta_2)\cos m(\phi-\phi_2) \end{aligned} \tag{3.37}$$

When two scatterers are present as in Figure 3.1, with $\bar{r}$ = observation point, then the scattered fields from scatterer 1 become additional incident field components for scatterer

2 and vice versa. Considering only first-order scattering (multiple scattering is considered negligible), the Debye potentials from scatterer 1 and 2 due to the presence of the other scatterer can be written as:

(Notation: $T_{i(q)}$ is the T-matrix of the i^{th} element due to the q-scatterers)

$$\begin{aligned}\pi^{scat}_{e_{r1(2)}} = &-\frac{E_0\cos\phi}{\omega\mu r}\sum_{n=1}^{\infty} Te_{1(1)_n}(2n+1)\hat{H}_n(kr) \\ &[\hat{J}_n(kr_1)P_n(\cos\xi_1)W_n + Te_{2(1)_n}\hat{J}_n(kr_2)P_n(\cos\xi_2)W_n]\end{aligned} \tag{3.38}$$

and

$$\begin{aligned}\pi^{scat}_{e_{r2(2)}} = &-\frac{E_0\cos\phi}{\omega\mu r}\sum_{n=1}^{\infty} Te_{2(1)_n}(2n+1)\hat{H}_n(kr)\cdot \\ &[\hat{J}_n(kr_2)P_n(\cos\xi_2)W_n + Te_{1(1)_n}\hat{J}_n(kr_1)P_n(\cos\xi_1)W_n]\end{aligned} \tag{3.39}$$

where

$$P_n(\cos\xi_i) = \sum_{m=1}^{n} 2\frac{(n-m)!}{(n+m)!}P_n^m(\cos\theta)P_n^m(\cos\theta_i)\cos m(\phi-\phi_i) \tag{3.40}$$

The total scattered fields in terms of the Debye potentials would then be

$$\pi^{scat}_{e_{total}} = \pi^{scat}_{e_{r1(2)}} + \pi^{scat}_{e_{r2(2)}} \tag{3.41}$$

To derive the aggregate T-matrix for q-scatterers, we start with the derivation of the T-matrices for individual i^{th} scatterer in the presence of the remaining scatterers, $\bar{\bar{T}}e_{i(q-1)}$. Applying the recursive algorithm outlined in equations (9) and (10) of [47], the T-matrices of individual scatterers are derived below, with calculations repeated for each wave mode n:

(Notation: $Te_{i(q)}$ is the T-matrix of the i^{th} scatterer due to q-scatterers.)

$$\begin{aligned}\bar{\bar{T}}_{q(q)} \cdot \hat{J}_n(kr_q)P_n(\cos\xi_q) = \\ [\bar{\bar{I}} - \bar{\bar{T}}_{q(1)} \sum_{i=1}^{q-1} \hat{H}_n(kr_i)P_n(\cos\xi_i)\bar{\bar{T}}_{i(q-1)} \cdot \hat{H}_n(kr_i)P_n(\cos\xi_i)]^{-1} \cdot \bar{\bar{T}}_{q(1)} \\ \cdot [\hat{J}_n(kr_q)P_n(\cos\xi_q) + \sum_{i=1}^{q-1} \hat{H}_n(kr_i)P_n(\cos\xi_i)\bar{\bar{T}}_{i(q-1)} \cdot \hat{J}_n(kr_i)P_n(\cos\xi_i)]\end{aligned} \tag{3.42}$$

$$\begin{aligned}\bar{\bar{T}}_{i(q)} \cdot \hat{J}_n(kr_i)P_n(\cos\xi_{qi}) = \bar{\bar{T}}_{i(q-1)} \\ \cdot [\hat{J}_n(kr_i)P_n(\cos\xi_i) + \hat{H}_n(kr_{i,q})P_n(\cos\xi_{i,q}) \cdot \bar{\bar{T}}_{q(q)} \cdot \hat{J}_n(kr_q)P_n(\cos\xi_q)]\end{aligned} \tag{3.43}$$

Re-writing (3.42) in terms of α and β matrices used in [44], result in:

$$\begin{aligned}\bar{\bar{T}}_{q(q)} \cdot \bar{\bar{\beta}}_{q(0)} = [\bar{\bar{I}} - \bar{\bar{T}}e_{q(1)} \sum_{i=1}^{q-1} \bar{\bar{\alpha}}_{q(i)} \cdot \bar{\bar{T}}_{i(q-1)} \cdot \bar{\bar{\alpha}}_{i(q)}]^{-1} \cdot \bar{\bar{T}}_{q(1)} \\ \cdot [\bar{\bar{\beta}}_{q(0)} + \sum_{i=1}^{q-1} \bar{\bar{\alpha}}_{q(i)} \cdot \bar{\bar{T}}_{i(q-1)} \cdot \bar{\bar{\beta}}_{i(0)}]\end{aligned} \tag{3.44}$$

Figure 3.2 depicts the role of α and β matrices in translating between the scattering locations and the coordinate reference. Equation (3.43) can now be applied to evaluate the scattered field of the individual q^{th} scatterer in the presence of the other scatterers in the system. Specifically, this can be expressed as:

$$\begin{bmatrix} \pi^{scat}_{e_{r_{i(q)}}} \\ \pi^{scat}_{m_{r_{i(q)}}} \end{bmatrix} = \bar{\bar{T}} \cdot \begin{bmatrix} \pi^{inc}_{e_{r_{i(q)}}} \\ \pi^{inc}_{m_{r_{i(q)}}} \end{bmatrix} \tag{3.45}$$

where $\pi^{inc}_{e_{r_{i(q)}}}$ and $\pi^{inc}_{m_{r_{i(q)}}}$ are defined by equations (3.16) and (3.17).

Extending equation (3.41) to q-scatterers:

$$\pi^{scat}_{e_{total}} = \sum_{i=1}^{q} \pi^{scat}_{e_{r_{i(q)}}} \tag{3.46}$$

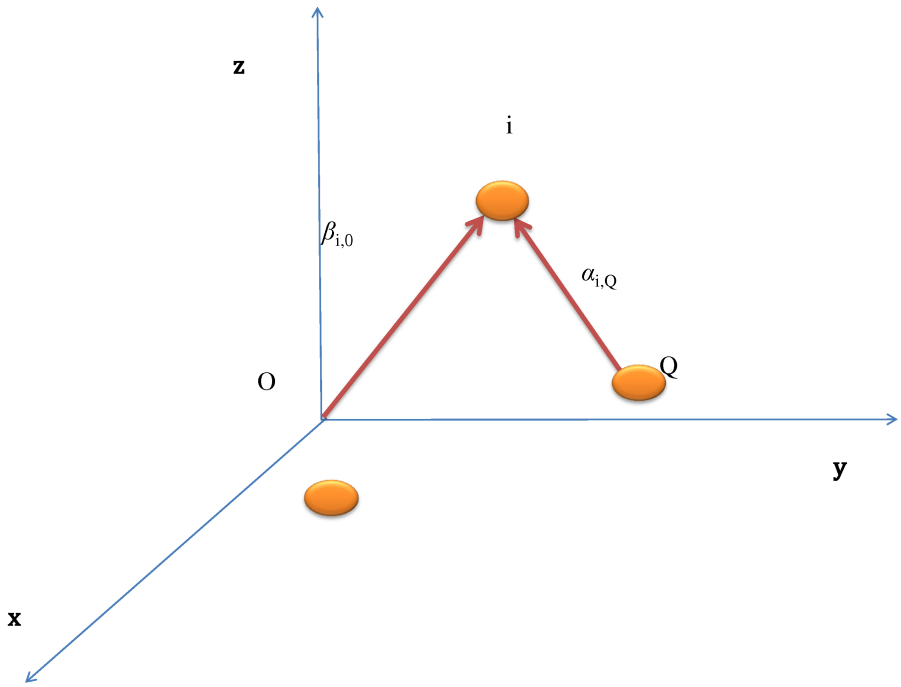

Figure 3.2: Multiple Scattering: T-matrix recursive algorithm

The aggregate T-matrix for the system of q scatterers is defined by

$$\bar{\bar{T}}_{total} = \sum_{i=1}^{q} \text{diag}\left\{\hat{H}_n(kr_q)P_n(\cos\xi_{0,q})\right\} \cdot \bar{\bar{T}}_{i(q)} \cdot \text{diag}\left\{\hat{J}_n(kr_q)P_n(\cos\xi_{q,0})\right\} \tag{3.47}$$

In terms of α and β matrices, equation (3.47) can be written as follows:

$$\bar{\bar{T}}_{total} = \sum_{i=1}^{q} \bar{\bar{\beta}}_{0(i)} \cdot \bar{\bar{T}}_{i(q)} \cdot \bar{\bar{\beta}}_{i(0)} \tag{3.48}$$

Re-writing $\bar{\bar{T}}_{q(q)}$ in terms of $\bar{\bar{T}}_{total}$, the equation takes the form:

$$\begin{aligned} &\bar{\bar{T}}_{q(q)} \cdot \hat{J}_n(kr_q)P_n(\cos\xi_q) = \\ &\quad [\bar{\bar{I}} - \bar{\bar{T}}_{q(1)}\hat{H}_n(kr_q)P_n(\cos\xi_q)\bar{\bar{T}}_{total-1} \cdot \hat{H}_n(kr_q)P_n(\cos\xi_q)]^{-1} \cdot \bar{\bar{T}}_{q(1)} \\ &\quad \cdot [\hat{J}_n(kr_q)emphP_n(\cos\xi_q) + \hat{H}_n(kr_q)P_n(\cos\xi_q)\bar{\bar{T}}_{total-1}] \end{aligned} \tag{3.49}$$

or equivalently

$$\begin{aligned}\bar{\bar{T}}_{q(q)} \cdot \bar{\bar{\beta}}_{q(0)} = \\ [\bar{\bar{I}} - \bar{\bar{T}}_{q(1)} \cdot \bar{\bar{\alpha}}_{q(0)} \cdot \bar{\bar{T}}_{total-1} \cdot \bar{\bar{\alpha}}_{0(q)}]^{-1} \cdot \bar{\bar{T}}_{q(1)} \\ \cdot [\bar{\bar{\beta}}_{q(0)} + \bar{\bar{\alpha}}_{q(0)} \bar{\bar{T}}_{total-1}]\end{aligned} \tag{3.50}$$

Finally, the aggregate T-matrix recursive algorithm is given by:

$$\begin{aligned}\bar{\bar{T}}_{total} = \bar{\bar{T}}_{total-1} + [\text{diag}\left\{\hat{J}_n(kr_q)P_n(\cos\xi_q)\right\} + \bar{\bar{T}}_{total-1} \cdot \text{diag}\left\{\hat{H}_n(kr_q)P_n(\cos\xi_q)\right\}] \\ \cdot \bar{\bar{T}}_{q(q)} \cdot \text{diag}\left\{\hat{J}_n(kr_q)P_n(\cos\xi_q)\right\}\end{aligned} \tag{3.51}$$

or equivalently

$$\bar{\bar{T}}_{total} = \bar{\bar{T}}_{total-1} + [\bar{\bar{\beta}}_{0(q)} + \bar{\bar{T}}_{total-1} \cdot \bar{\bar{\alpha}}_{0(q)}] \cdot \bar{\bar{T}}_{q(q)} \cdot \bar{\bar{\beta}}_{q(0)} \tag{3.52}$$

With these aggregate T-matrices, the scattered fields are readily calculated using equations (3.23) to (3.25).

3.3 System Analysis Results

The objective of this forward model is to gain a better understanding of the quantitative contributions of the various system parameters to the overall system behavior. These parameters include frequency of operation, radius and angle of observation, contrast in tissue permittivity, signal attenuation through target tissue, number and location of target tumors. The system simulation model is built in such a manner as to isolate the effects of the various parameters from each other, i.e., as one specific parameter is studied, the rest of the parameters are kept constant.

The simulation coordinate system is depicted in Figure 3.3. It consists of a breast skin

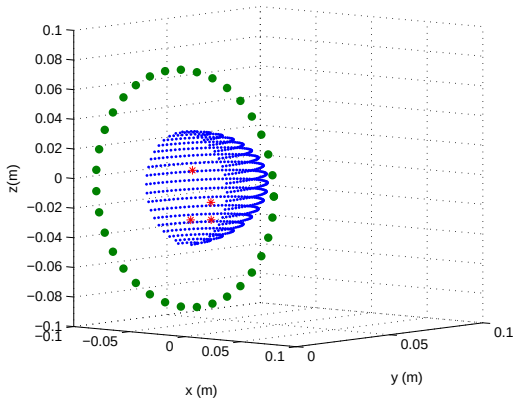

Figure 3.3: Coordinate system setting for orientation and location of spherical skin model and malignant tumors.

model built from multiple very-small spheres, arranged in a hemisphere with a radius of 4cm. The observation points are marked by the 'green' or outer ring of spheres at a radius of 8cm from the origin of the coordinate system. The smaller domain size was chosen to expedite computation time. The tissue dielectric properties for healthy breast tissues are taken from the 2007 large-scale *in-vitro* study [3]. Malignant tumors are represented by spheres placed inside the 4cm-radius hemisphere. The dielectric constants of the cancerous cells are assigned multiplicative contrast ratios to the healthy tissue dielectric constant values, ranging from $1.1 \cdot \varepsilon_{normaltissue}$ up to $\varepsilon_{malignant} = 80$. Due to a lack of consistent published data for conductivity of malignant tumors, $\sigma_{malignant}$, the cancerous conductivity values are set to conductivity values of normal tissue. The permittivity of skin, ε_{skin}, is taken from [12] for dry skin, namely, $\varepsilon_{skin} = 35$, with conductivities ranging from 0.635 S/m at 1 GHz to 2 S/m at 5 GHz.

3.3.1 Frequency

The principal starting point for a system parameter study is its frequency range of operation. Considering that human tissue is relatively lossy at microwave frequencies, the primary objective is to quantify the feasibility of a MWI system to operate at the higher frequencies necessary to give the desired resolution of 5mm to detect early-stage tumor.

The simulation set-up is depicted in Figure 3.3: the 'skin' is composed of multiple spheres arranged in a hemisphere of 4cm radius, skin thickness (diameter of spheres) is 2mm, ε_{skin} = 35, antennas are located 4cm away from breast skin, two 1cm tumors are placed inside the breast.

Two cases are presented for analysis of system operating frequency, with the objective of understanding system sensitivity over the wide range of measured normal tissue dielectric values (see Figure 2.2). The first case uses the higher dielectric values with coupling medium matched to these dielectric values for optimum transfer of energy to the breast tissue. Specifically, these $\varepsilon_{normaltissue}$ values are (see Figure 2.2):

- frequency = 1 GHz, ε_{tissue} = 45 + i1
- frequency = 2 GHz, ε_{tissue} = 44 + i2
- frequency = 3 GHz, ε_{tissue} = 43 + i2.5
- frequency = 4 GHz, ε_{tissue} = 42 + i3
- frequency = 5 GHz, ε_{tissue} = 40 +i3.5

The second case uses dielectric properties at the lower end of the range, $\varepsilon_{normaltissue}$ = 20, with coupling medium dielectric properties as shown in Figures 5.22 and 5.23.

Simulation results for first case (see Figure 3.4) show that the higher frequency of 5GHz will result in higher contrast between received signal when comparing the no-tumor and tumor cases, but at a much lower received power level. Already at 5 GHz, the received signal level at a depth of 8cm (radius of observation) is near -80dBm at best. Higher frequencies and larger depths (and larger breast radii) would result in even smaller scattered signal levels. At the lower frequencies, the received signal level is substantially higher, but the amplitude of the scattered field becomes progressively smaller. At 1 GHz, the scattered field is about 2dB. The observations up to this point would suggest that the practical op-

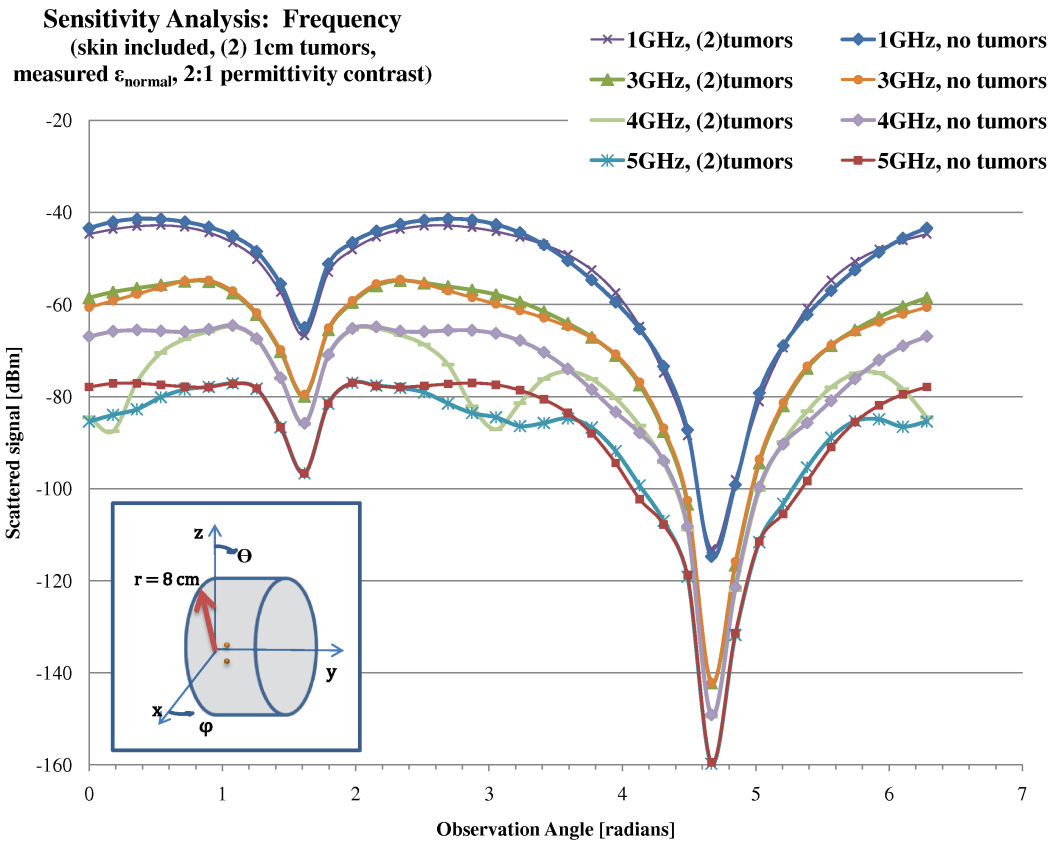

Figure 3.4: Simulated signal levels at 1GHz, 3GHz, 4GHz, and 5GHz, with and without the presence of two-1cm tumors. Dielectric properties are from Figure 2.2.

erating frequency range for the MWI imaging system reside at best in the 1-5 GHz range, even for 1cm (not the target 5mm) tumors.

Similar results are observed in Figure 3.5 for the case where normal tissue permittivity values are lower. Higher frequencies show better contrast in received signals for higher sensitivity towards presence of malignant tumors, again at the expense of lower overall signal strength. In comparison to results of the first case, simulated signal levels at the higher frequencies are still within practical detectable range - primarily due to the lower conductive losses of the coupling medium. Detailed discussion of this low loss coupling medium will be given in Chapter 5.

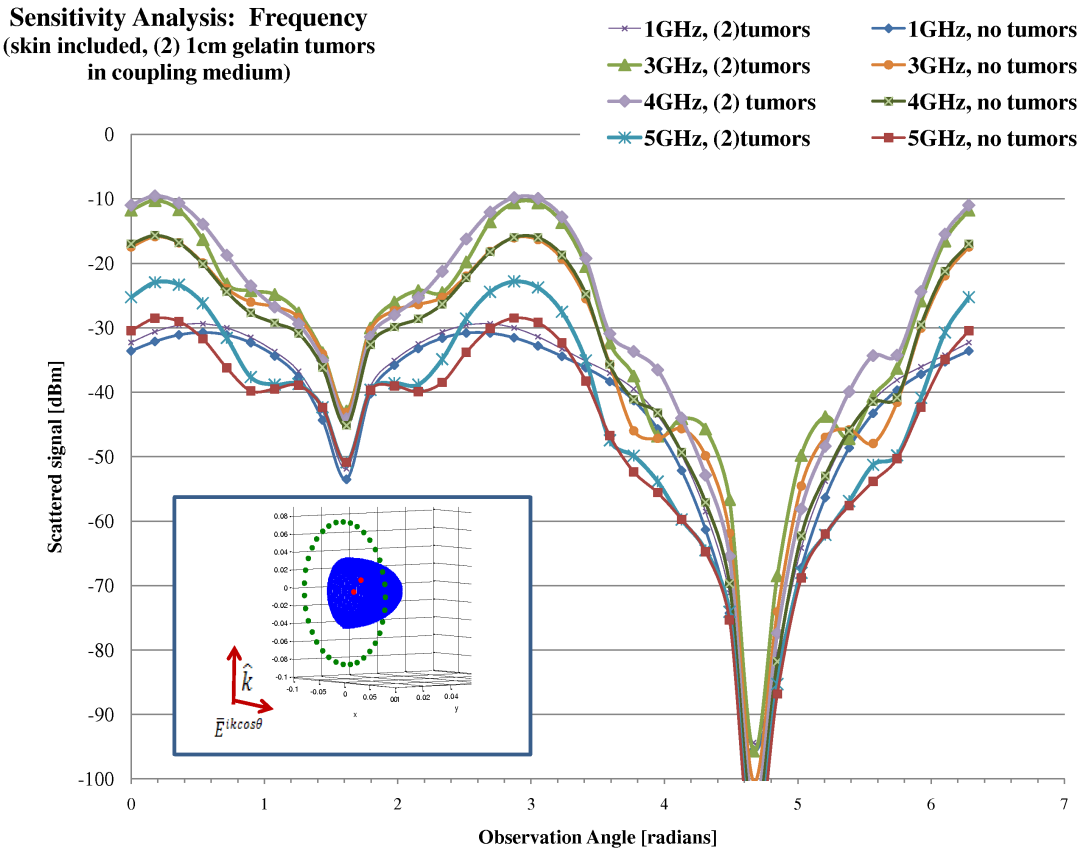

Figure 3.5: Simulated signal levels at 1GHz, 3GHz, 4GHz, and 5GHz, with and without the presence of two-1cm tumors. $\varepsilon_{normaltissue} \sim 20$.

3.3.2 Number, Size, and Location of Lesions

The next case study is the quantitative understanding of the system sensitivity towards the numbers, sizes, and locations of randomly placed tumors. A handful representative cases are included for this sensitivity study. Keeping the antenna locations constant, size and thickness of breast skin constant, tumor parameters were varied - number, size, and location. The following observations are noted from Figure 3.6:

1. Comparing the second and third curves of Figure 3.6: the expected signal shows good sensitivity to the location of the tumor, even for small tumor sizes. Signal strength at the varying observation angles reflect this sensitivity toward tumor location.

2. Comparing the fourth, fifth, and sixth curves of Figure 3.6: expected signal shows adequate sensitivity to the number and sizes of tumors.

The single-receiver scattering measurement is more sensitive to larger tumor sizes, as expected, but still even for a small tumor size there is measurable sensitivity. Since the inversion algorithm uses several measurements (not just at one receiver) to locate and characterize the unknown object, all that is needed is for the tumor to be detectable at each receiver, which is the case here.

3.3.3 Permittivity Contrast

Focusing at one of the operating frequencies - 3 GHz, the system analysis tool is then used to study the system dynamic range at varying contrasts between normal tissue and malignant tumor permittivity values. As expected, when the contrast between the permittivity values is small, for example $1.1 : 1$, it becomes more difficult to detect the presence of tumors with a single measurement; see Figure 3.7. Two study cases are presented here:

- Two 1cm tumors with permittivity contrasts of 3:1 and 1.5:1 with respect to background tissue (second and third curves of Figure 3.7).

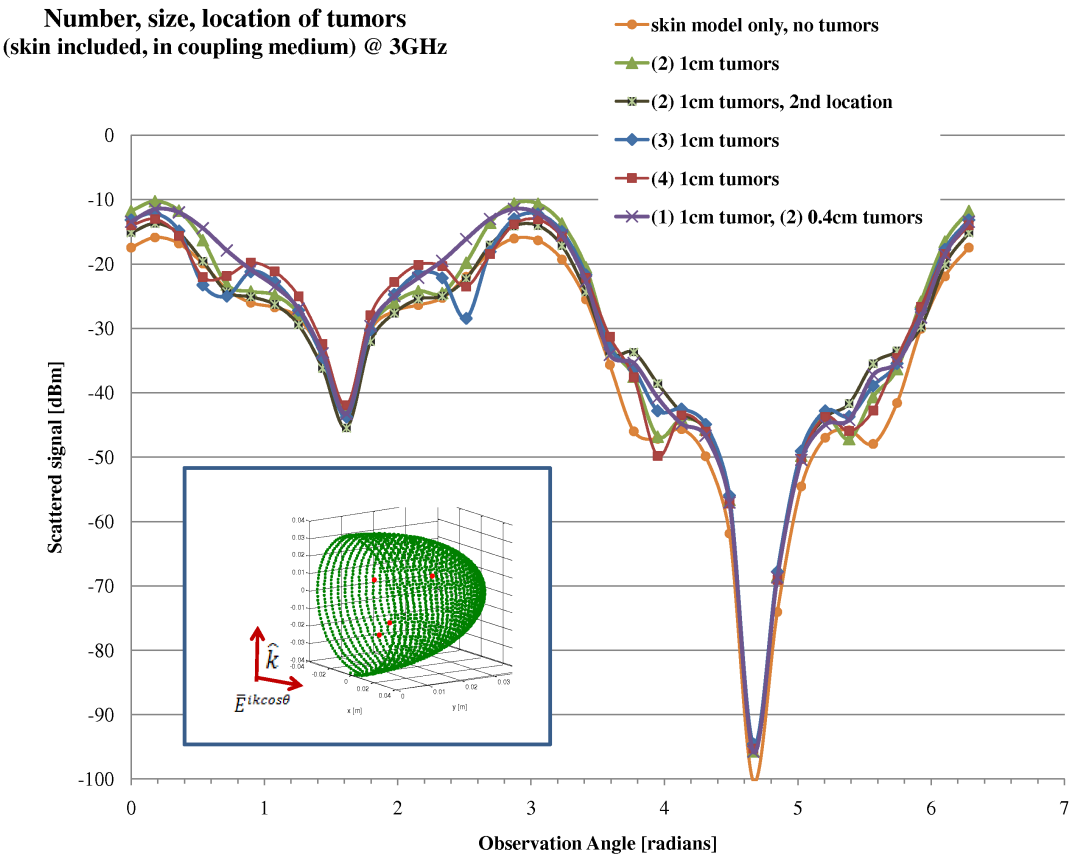

Figure 3.6: Simulated signal levels at 3GHz: varying tumor (number), size, and locations. ε_{tumor} = 65 + i2.5 tumors.

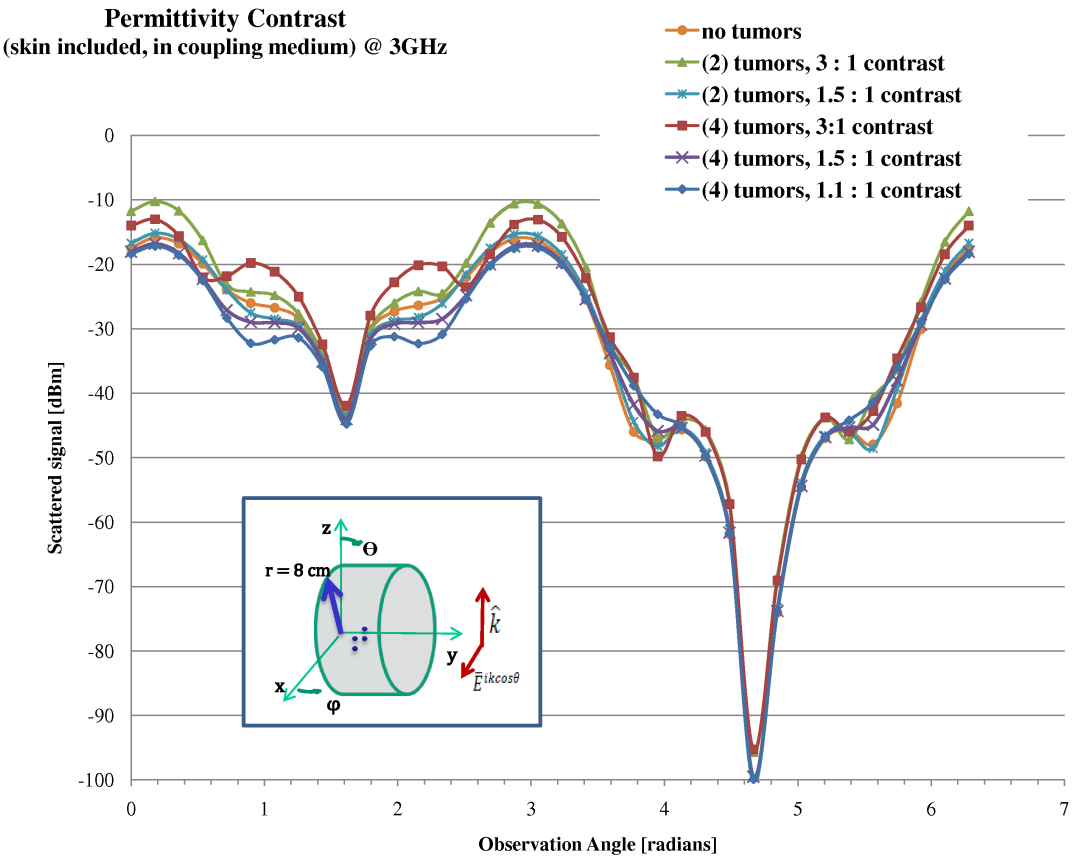

Figure 3.7: Simulated signal levels at 3GHz: permittivity contrast studies with 1cm tumors inside skin model.

- Four 1cm tumors with permittivity contrasts of 3:1, 1.5:1, and 1.1:1 with respect to background tissue (fourth, fifth, and sixth curves of Figure 3.7).

The result from the 1.1:1 contrast study is suggesting that it would be a challenge to detect small contrast in permittivity values. However, using more than one receiver with the varying observation angles of these receivers would address this issue. For simulation results shown in Figure 3.7, all other system parameters (except for tumor permittivity values) were kept unchanged from the previous simulation: radius of skin hemisphere is 4cm, skin thickness is 2mm, antennas are located 4cm away from breast skin, ε_{skin} = 35, tumor size of 1cm.

3.3.4 Summary of System Sensitivity Analysis

From the system sensitivity analysis presented this chapter, the system parameters are determined: frequency of operation, system signal dynamic range, and the need for a low loss coupling medium between signal sources and the breast skin and tissues. The frequency of operation is determined to be 1-4 GHz, with the desire to include operation up to 5 Hz. The operating frequency dictates the bandwidth of the antennas to be used as signal sources. The system dynamic range is set to the average received signal at 4 GHz in the range of 70dB, with assumptions: radius of skin hemisphere is 4cm, skin thickness is 2mm, antennas are located 4cm away from breast skin, two 1cm tumors are placed inside the breast, and with higher dielectric properties values for normal tissues given above. Studies of the system dynamic range specifies the permittivity and the conductivity range of values for the coupling medium. The permittivity of the coupling medium should be matched to the skin's relative permittivity of 35. The conductivity of the coupling medium should be minimized to minimize signal losses between signal radiated by the antennas and the target breast tissue.

CHAPTER 4

Ultra Wide Band (UWB) Antennas

4.1 Introduction

The primary requirement for the UWB imaging antennas to be used in the 3D time-domain non-linear super resolution inverse scattering microwave imaging techniques [42] is low dispersive behavior (linear phase) over the operating bandwidth of 1-4 GHz. The bandwidth requirement was established from the system parametric studies discussed in the previous chapter. Simulation results of the effect of dispersion are presented in Figure 4.1. Three imaging input pulses are shown in Figure 4.1 (a): ideal, ideal spread by 16% and ideal spread by 25%. Two known targets are present in the system, see Figure 4.1 (b). Figure 4.1 (c) shows the recovered image when an ideal input pulse is incident on the two known targets. However as the recovered image on Figure 4.1 (d) shows, a pulse that is spread by 16% would recover the targets with some degradation in the recovered image. When the pulse is further spread to 25%, recovered targets images are poor. From these observations, the maximum pulse spreading criteria is set to 16%.

Secondary objectives for this imaging antenna include being conformal to the human body and having a physical size compatible for breast imaging purposes. The design and test results of the UWB for the time-domain imaging technique are presented in the last two sections of this chapter, where first the prototype imaging antennas are optimized to radiate

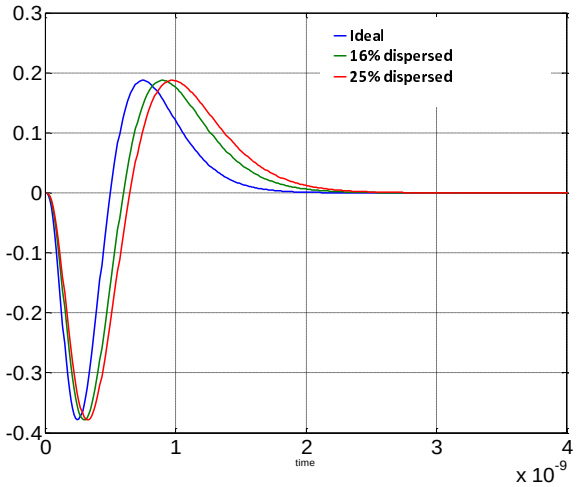

(a) Time-domain pulses

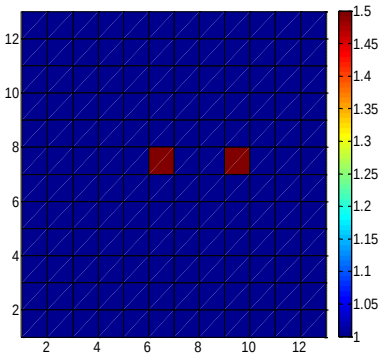

(b) Known targets

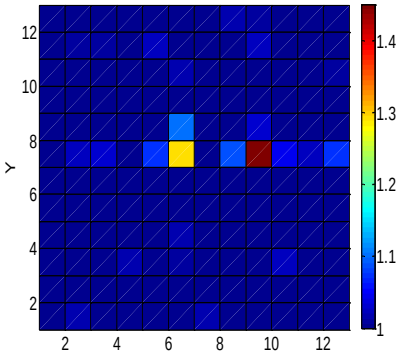

(c) Recovered with ideal pulse

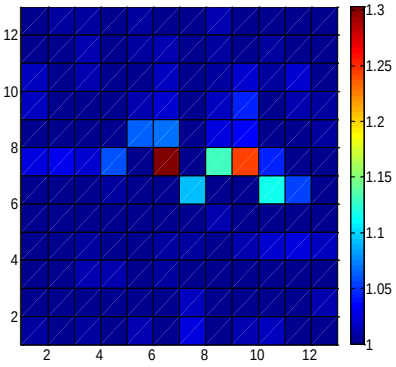

(d) Recovered with 16% pulse spreading

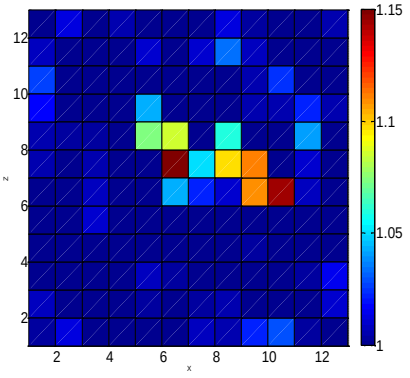

(e) Recovered with 25% pulse spreading: resolution is lost

Figure 4.1: Simulated effect of pulse spreading on recovered images

in ‘free space,’ followed by the final design optimized to radiate inside ‘tissue-mimicking’ coupling medium. However, the discussion of the UWB design details should start with definition of UWB, a brief history of these antennas, and an overview of UWB antenna designs.

The generally accepted definition of UWB antennas bandwidth follows the 1990 Defense Advanced Research Projects Agency (DARPA) report and more recently the 2003 Federal Communications Commission (FCC) publication [48]:

$$bw = 2\frac{f_H - f_L}{f_H + f_L} \geq \begin{cases} 0.25 DARPA \\ 0.2 FCC \end{cases} \tag{4.1}$$

UWB antennas have received renewed interest since the 2002 FCC allocation of the 3.1-10.6 GHz spectrum for unlicensed UWB applications. Most of the UWB antenna applications have been directed to the wireless communication industry. Taking advantage of these developments, the UWB antennas are finding new applications in microwave medical imaging as well. This chapter focuses on the design, fabrication, and testing of tapered, planar, elliptical dipoles operating in the 1-4 GHz frequency range - as part of the experimental demonstration for the 3D time-domain inverse scattering imaging technique. To begin, an overview of UWB antennas is included to provide historical context and technical motivation for the selection of the proposed UWB antenna design.

4.2 Overview of UWB Antennas

The study of published work in UWB antennas revealed that most UWB antenna applications are focused on wide-band communication and/or surveillance systems. The physical topologies of antennas for communication systems are mostly of the planar or conformal type. With the objective of an microwave imaging application in mind - in particular, of having physically small antennas - the scope of the literature study was directed

mainly toward planar antennas. While communication antennas share the physical size and bandwidth objectives with our microwave imaging antenna, they do not have specific requirements on dispersion properties. For this high resolution imaging application using time-domain pulses, a maximum pulse spreading requirement of 16% was imposed as discussed earlier.

In one UWB overview study [49], a number of antennas were presented including the loaded antennas (dipole, bicone, TEM horn, log period, Archimedean spiral) and conventional wideband antennas (volcano smoke, diamond dipole, mono-filar helix, conical spiral, monoloop, quad-ridge circular horn). In the cases of loaded antennas, [49] modeled the behavior of these antennas to mimic traveling waves by adding loads. In all cases, the transmitted and received wave signals were simulated with no experimental results presented. Most of the antennas were non-planar, except for the physically large Vivaldi antennas and the circular disc dipole. In the latter case, only simulation results were included. Another overview study [50] presented several microstrip UWB antennas. The wideband frequency magnitude data was discussed, with little mention of the phase linearity performance of these planar antennas. With regard to phase linearity over a wide bandwidth, the article specifically mentioned that Vivaldi antennas would give the most linear phase behavior. However, Vivaldi antennas are inherently large in physical size. Furthermore, the results in the previous paper [49] showed otherwise, in that the phase of the Vivaldi antenna was far from linear as evidenced by substantial pulse dispersion.

In focusing on planar UWB antennas, a large number of papers are readily available. Common to the antennas aimed at wireless communications applications, is the absence of measured phase data [51] [52] [53] [54] [55] [56] [57] [58] [59] [60]. One paper did present phase studies, although only simulated results [61]. Gain and efficiency are the dominant parameters for such communication systems. Although these antennas cover a higher frequency range of 3-11 GHz, they can potentially be scaled to the imaging frequency range of 1-4 GHz if phase linearity can be assured.

As for the antennas intended for medical therapeutic applications, the design focus is on addressing the signal matching and coupling into tissues and ease of handling [62]. The antenna designs introduced for medical imaging begin to address the time-domain signal fidelity [63], although some of these antennas are not planar [64]. In the case of the 'dark eyes' antenna in [63], experimental validation has yet to be done. The 3-10 GHz elliptical dipole for in-body implant, presented in [65], was optimized for a data communication link rather than imaging. Their study showed a shift in frequency response of the antenna in air versus in-body since it took into account the dispersive property of tissues; however, phase information was lacking. One other study [66] showed fidelity studies between two time domain signals - again for wireless communications purposes. Time-domain signal spreading would not be acceptable for our 3D super resolution inverse scattering imaging technique.

Lastly, a set of papers discussed a design methodology for dispersionless UWB antenna design [67] [68]. This design methodology is presently in theoretical study phase - it has developed some antenna design suggestions, but it has yet to implement and test such design theory.

This overview discussion on the subject of UWB antennas for medical applications would not be complete without the mention of the miniaturized pyramidal horn antenna for the space-time beam-forming imaging technique developed at the University of Wisconsin [23], and the UWB tissue-sensing-adaptive-radar antenna developed at the University of Calgary [25]. These two antennas exhibit a wide operating frequency range (though no phase linearity data were documented), however the planar physical attributes of the tapered elliptical dipole antennas proposed in this thesis are better suited for the breast imaging application.

At the conclusion of the literature study, it was apparent that no existing antenna would satisfy both the wide bandwidth and phase linearity requirements of the 3D non-linear time-domain super resolution inverse scattering technique. The research focus was then directed

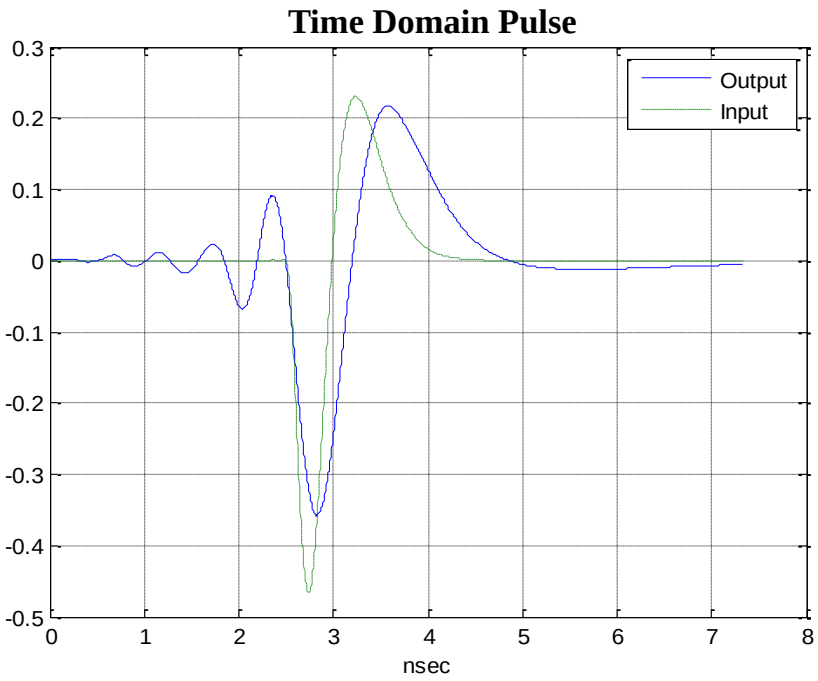

Figure 4.2: Time-domain pulse transmission through a pair of identical elliptical dipoles: 'spreading' effect on the output signal

to the design, fabrication, and testing of a low-dispersion UWB antenna - starting with prototype antennas optimized to radiate into free space, followed by the design adaptation of the low-dispersion antennas for operation in tissue-coupling medium.

4.3 Imaging Antenna Design

The design objective is to achieve a low-dispersion, 1-4 GHz planar antenna by taking into consideration the end-to-end time-domain behavior of the imaging system when pairs of these antennas are employed. The critical requirement as applied to the inversion technique is linear phase over the operating frequency band. Figure 4.2 illustrates the adverse effect of a reported phase-linear UWB [51] - even a slight non-linearity in phase over the frequency band of interest would result in signal 'spreading' of nearly 20%. This signal 'spreading' is not acceptable for the super-resolution algorithm technique - where time-domain signal spreading must be contained to less than 16%.

The design approach was to select a planar antenna that can meet most of our physical requirements and then design in the electrical properties to meet our inverse scattering phase-linearity-over-frequency criterion. The planar elliptical dipole antenna was selected for its small size (relative to wavelength), which is among the major contributing factors to its low dispersive property [51] [48] [50] [66]. Further, the selection of the elliptical dipole topology was motivated by an earlier study [62] which cited the advantages of 'ring'-type or circular geometry for on-body coupling of microwave energy. These geometries typically can provide good impedance match and low energy leakage away from target tissue - there are no sharp corners or edges where current concentrates would reduce antenna coupling efficiency. This simpler 'ring' type geometry would readily lend itself to conformal breast tissue imaging antennas compared to the 'end-fire' type geometries such as the family of tapered slot antennas. However, this elliptical dipole antenna does not meet our imaging technique requirement in terms of time-domain pulse 'spreading'. The time-domain behavior of a wide-band signal transmitted through two identical elliptical dipoles has been shown in Figure 4.2.

The antenna design focus remains to be the phase linearity of antenna response throughout the source pulse frequency content to preserve the shape of the input pulse as it is transmitted through the antenna into the breast target region. The investigation of phase linearity has been lacking in the previously reported studies. The design procedure was to model the steady-state antenna performance with Ansoft's High Frequency System Simulator (HFSS). The frequency domain simulated transmission data were then weighted by the frequency spectrum of the source pulse used by the time-domain inversion algorithm - to determine the antenna's time-domain behavior as discussed below. The optimum antenna physical parameters were derived from the trade-off among phase linearity, input amplitude match bandwidth, and transmitted signal amplitude flatness over the spectrum.

The starting values for the elliptical radiating elements radius and axial ratios were determined by the frequency spectrum of the input pulse. A distinguishing feature of this

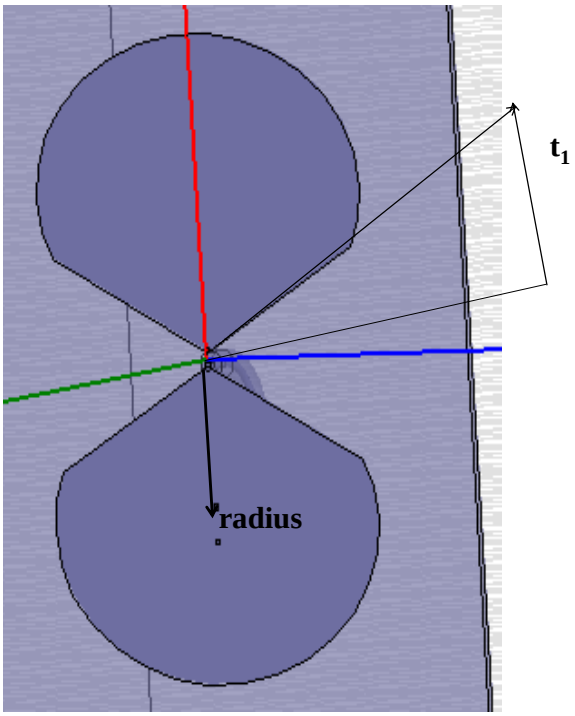

Figure 4.3: Tapered elliptical dipole UWB antenna design

antenna design is the introduction of tapering geometry into the ellipses, at the wave input to the radiating elements, with the intention to produce more linear phase behavior from the exiting waves. Taper dimension is defined as

$$taper = \arcsin \frac{1 - t_1}{50mm} \tag{4.2}$$

t1 = 1mm means no taper is added to the elliptical radiators. Results of the parametric studies are to follow; the final antenna design has a minor radius of 23mm, with ratio of major radius of 1.35, and a tapering factor of 26mm. The parametric study followed the map outlined in Figure 4.4.

To start, input match S11 phase linearity was studied over the minor radius range of 16mm $<$ radius $<$ 27mm, at a fixed ratio and with no taper added, in parallel with the study of the competing criteria of S21 magnitude flatness. Figures 4.5, 4.6, and 4.7 illus-

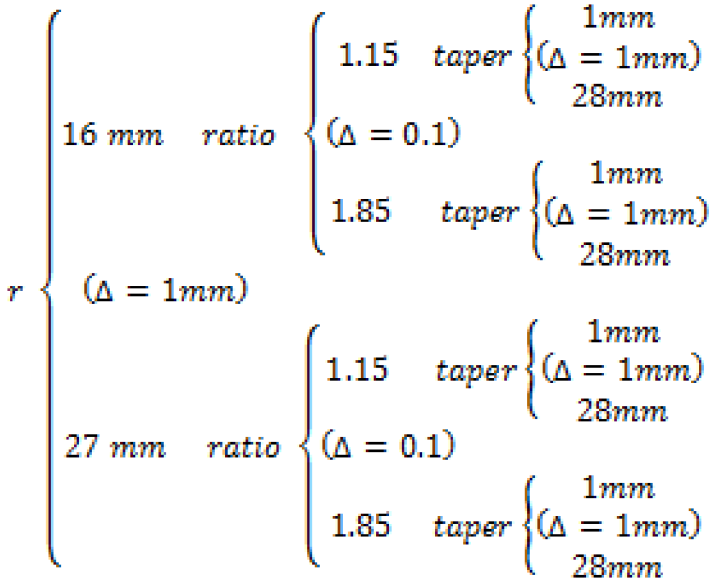

Figure 4.4: Parameters study map: radius is varied from 16mm < radius < 27mm, ratio is varied from 1.15 < ratio < 1.85, taper is varied from 1mm < taper < 26mm

trate the antenna match/linearity and transmission amplitude flatness trade off. As radius increases, S11 phase becomes less linear (see Figure 4.5) over frequency of interest. The best input match was observed for minor radius between 20-23mm (see Figure 4.6). This improvement in input match results in better S21 signal transmission, i.e. flatter amplitude variation, over the 1-4 GHz frequency range as seen in Figure 4.7. S21 signal transmission is between two identical transmit and receive antennas. The initial conclusion is then to focus on the mid-values of 20 - 23mm for the minor radius size.

The next study was phase linearity versus radius axial ratio, as axial ratio is varied from 1.15 to 1.85. As observed by comparing Figures 4.8 and 4.9, there is less effect on phase linearity due to varying the ellipse axial ratio on the smaller radius of 18mm than on the larger radius of 23mm. Focusing on the minor radius of 23mm (see Figure 4.9), it was observed that the lower axial ratio show better S11 phase linearity.

At fixed radius sizes, it was observed that antenna input match improves with increasing axial ratio, see Figures 4.10 and 4.11. Again this corresponds to better signal transmission behavior - flatter amplitude variation over frequency of interest, see Figures 4.12 and 4.13.

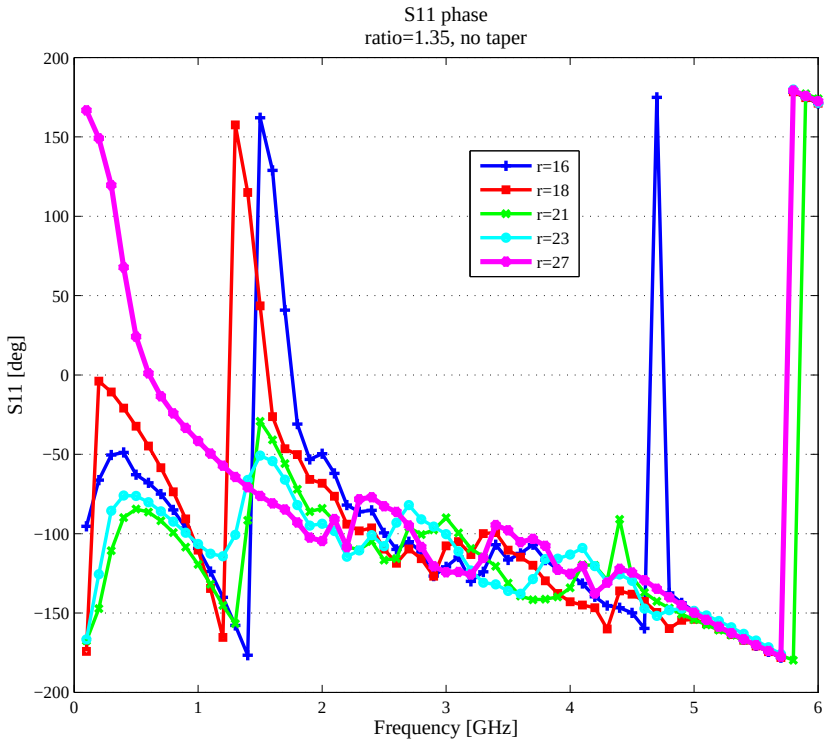

Figure 4.5: S11 [phase] at fixed axial ratio = 1.35 and minor radius = 16mm $<$ radius $<$ 27mm, with no tapering factor.

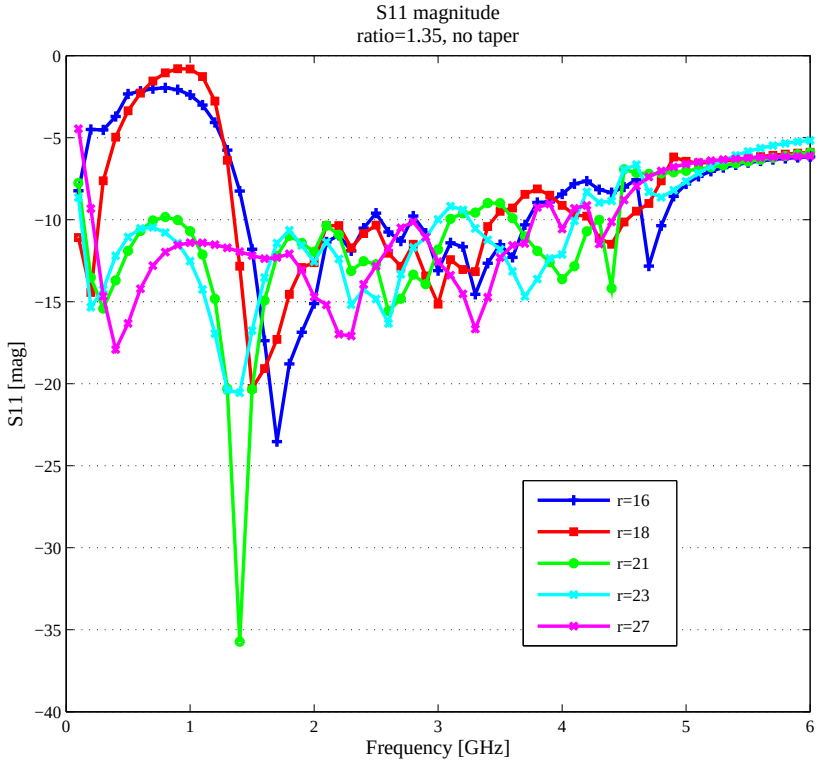

Figure 4.6: S11 [magnitude] at fixed axial ratio = 1.35 and minor radius = 16mm $<$ radius $<$ 27mm, with no tapering factor

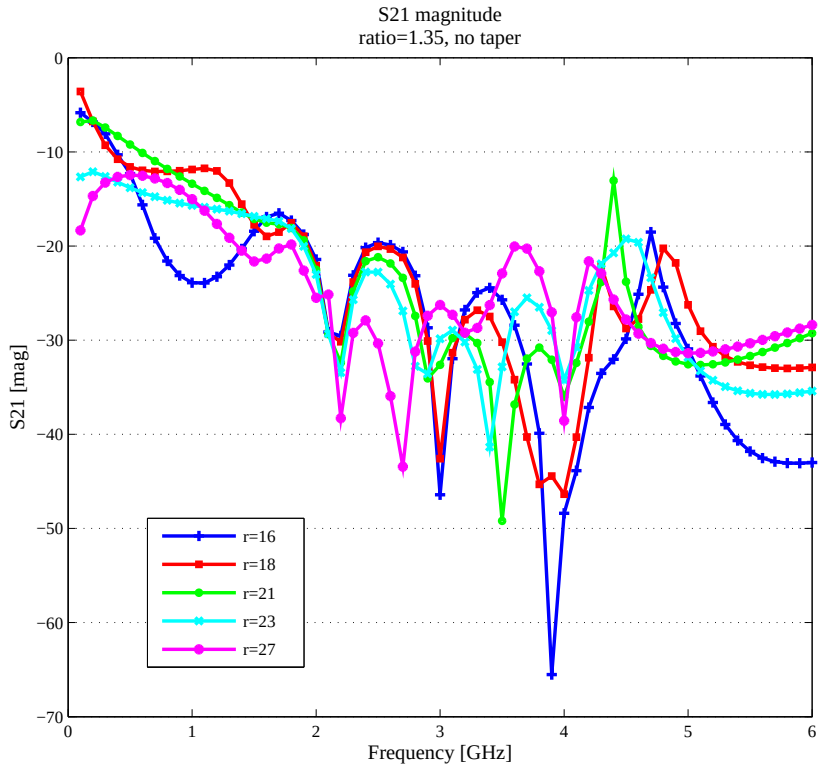

Figure 4.7: S21 [magnitude]: two identical transmit/receive antennas with axial ratio = 1.35 and minor radius = 16mm $<$ radius $<$ 27mm

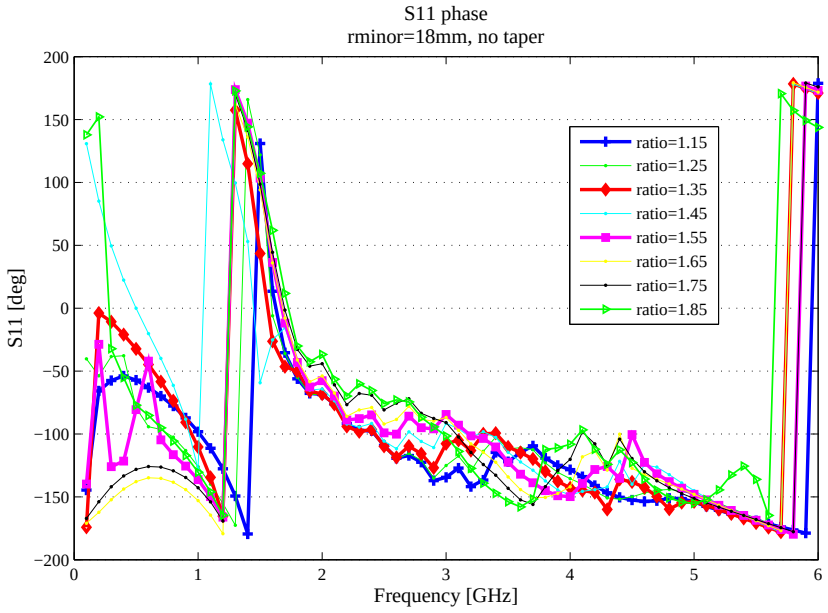

Figure 4.8: S11 [phase]: 1.15 $<$ axial ratio $<$ 1.85, minor radius=18mm, with no tapering factor

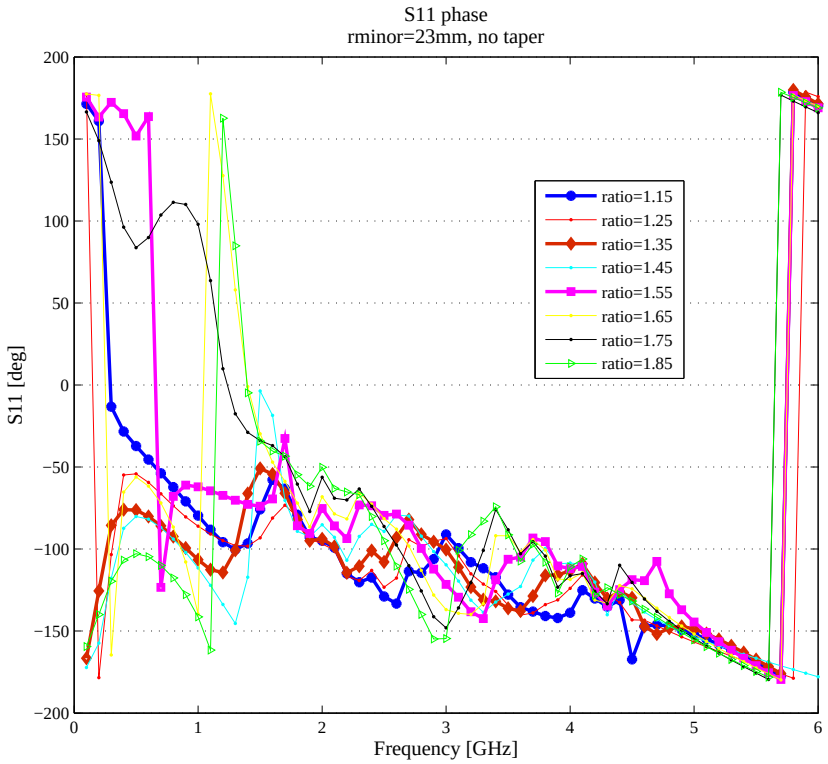

Figure 4.9: S11 [phase]: 1.15 < axial ratio < 1.85, minor radius = 23mm, with no tapering factor

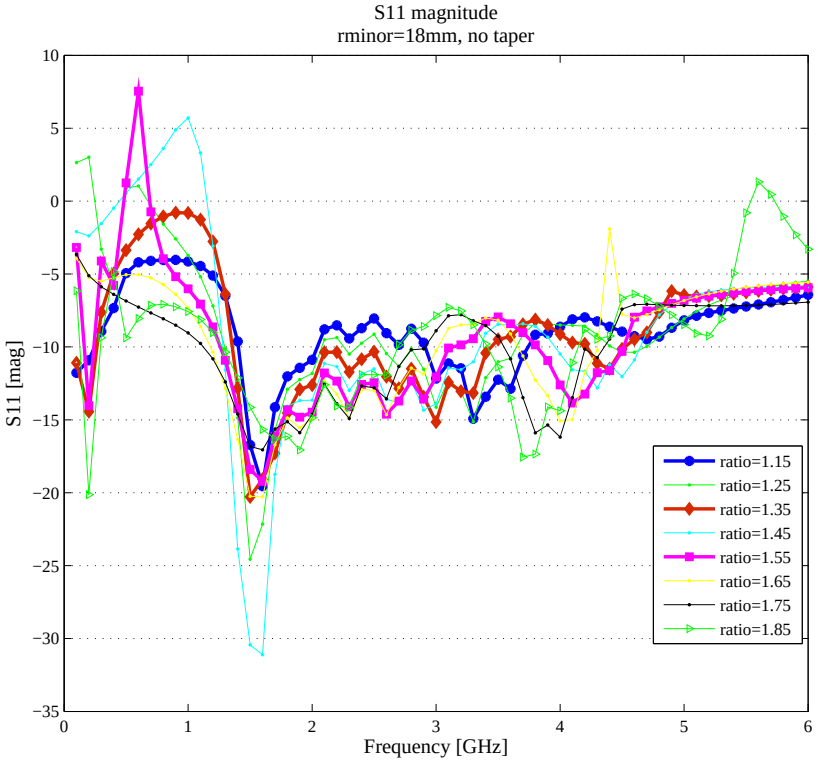

Figure 4.10: S11 [magnitude]: 1.15 $<$ axial ratio $<$ 1.85, minor radius = 18mm, with no tapering factor

Proceeding from earlier conclusion, the parametric study focused on the largest ratio to accommodate S21 magnitude flatness with the least compromise of S11 phase linearity to settle at axial ratio of 1.35.

Progressing with the antenna design, the next step is to study the antenna's time-domain behavior. At this point, two antenna parameters have been determined: minor radius of 23mm, eccentricity ratio of 1.35.

A simulation tool was developed for the purpose of time-domain signal analysis. The frequency spectrum of the inverse scattering algorithm's input pulse is passed through two identical (transmit and receive) antennas separated by a distance of 25cm - arbitrarily determined to be a practical system physical extent for the analysis in 'free space'. As the antenna design is adapted later to radiate inside the imaging tank filled with liquid cou-

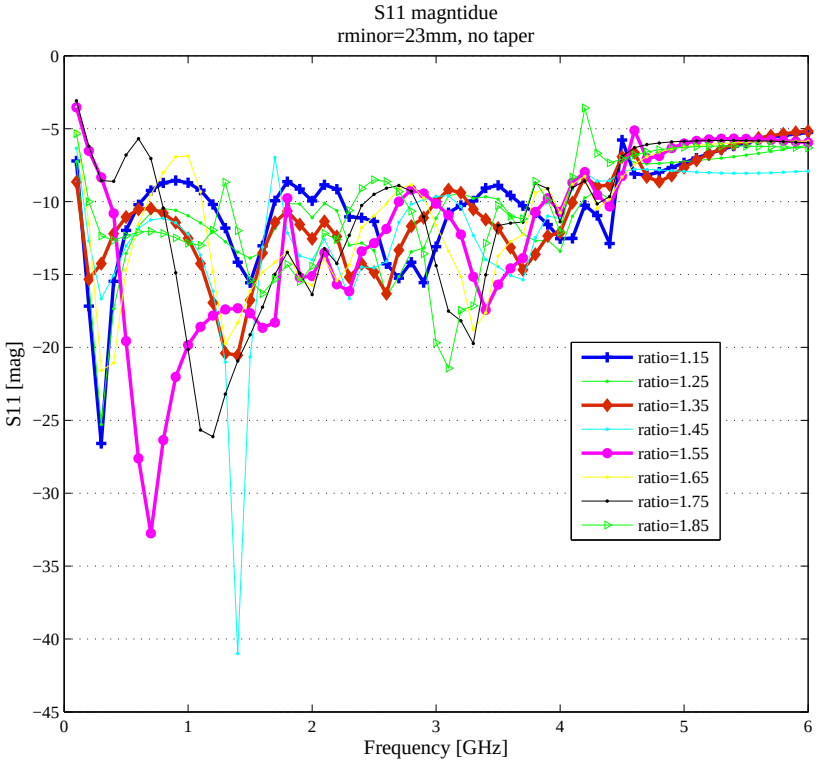

Figure 4.11: S11 [magnitude]: 1.15 $<$ axial ratio $<$ 1.85, minor radius = 23mm, with no tapering factor

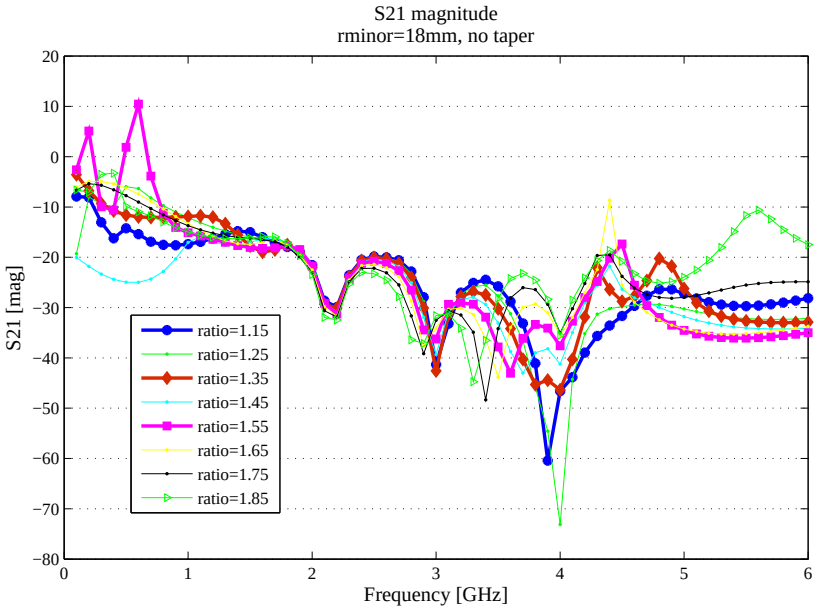

Figure 4.12: S21 [magnitude]: 1.15 $<$ axial ratio $<$ 1.85, minor radius = 18mm, with no tapering factor

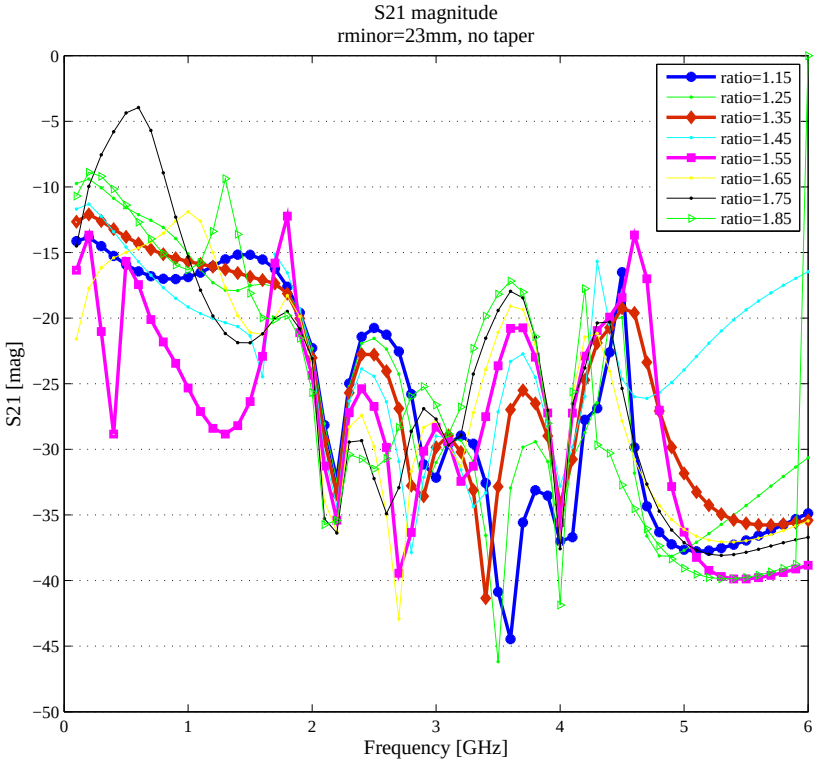

Figure 4.13: S21 [magnitude]: 1.15 $<$ axial ratio $<$ 1.85, minor radius = 23mm, with no tapering factor

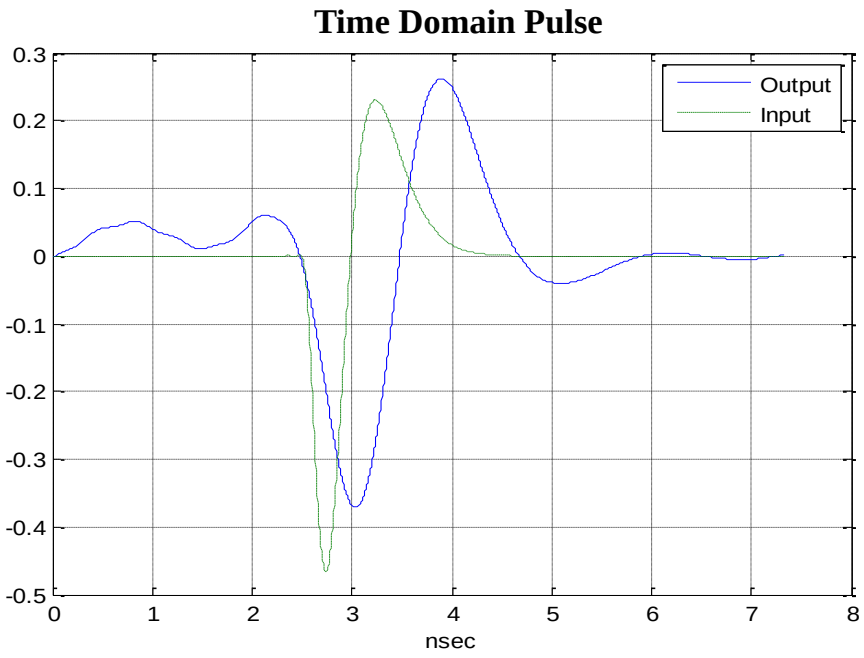

Figure 4.14: Time-domain pulse transmission through a pair of identical elliptical dipoles, radius = 23mm, axial ratio = 1.35: 'spreading' on the output signal

pling medium, this separation distance will be revisited and set to 10cm and 15cm. The frequency content of the received pulse is then transformed to its time-domain signal. This received pulse is compared to the original input pulse. The time domain analysis tool is useful in quantifying the time-domain behavior of the various antenna design iterations - to arrive at the selected antenna design parameters to realize. At each of parametric design studies above, the simulated S21 response is passed through the time-domain analysis tool. For the antenna design above, its time-domain response still showed similar 'spreading' effect, see Figure 4.14, as in previously reported studies [69]. At this point, the parametric studies were iterated with the introduction of tapering geometry to the elliptical radiating elements. The effect of adding the tapering geometry on the phase linearity is shown in Figure 4.15. Tapering factor of 26mm seemed to show the best phase linearity over the frequency band of interest. Figure 4.16 shows the expected pulse from a pair of antennas with taper added to the elliptical radiating elements.

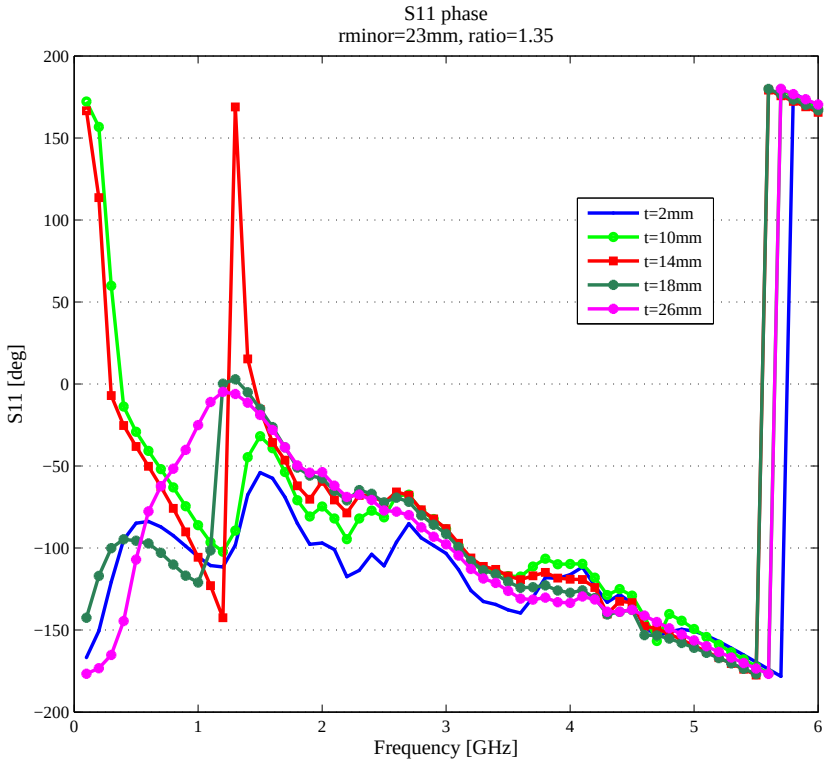

Figure 4.15: S11 [phase]: axial ratio = 1.35, minor radius = 23mm, 2mm $<$ taper $<$ 26mm

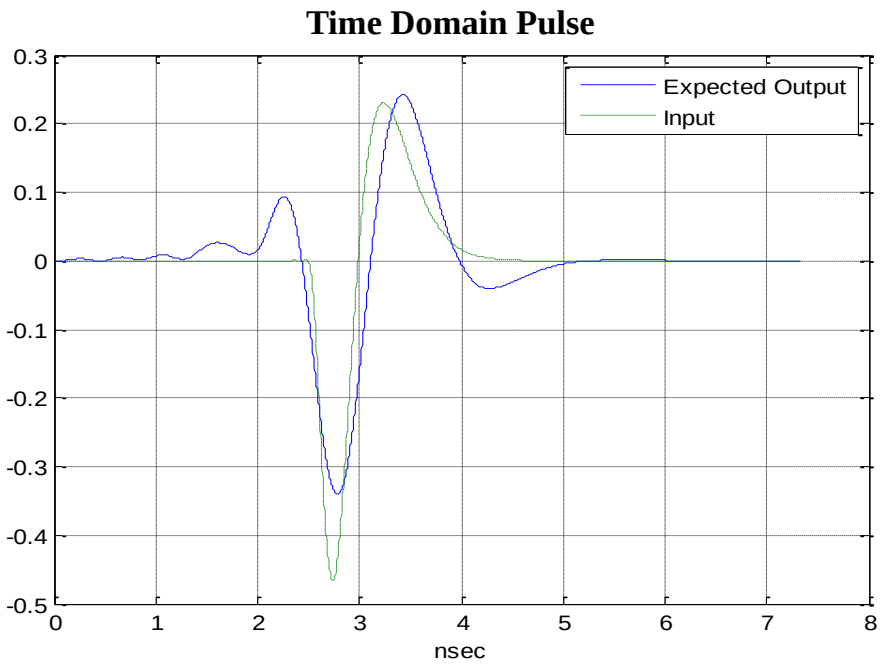

Figure 4.16: Time-domain pulse transmission through a pair of identical elliptical dipoles, radius = 23mm, axial ratio = 1.35: expected output pulse with tapering factor of 26mm added

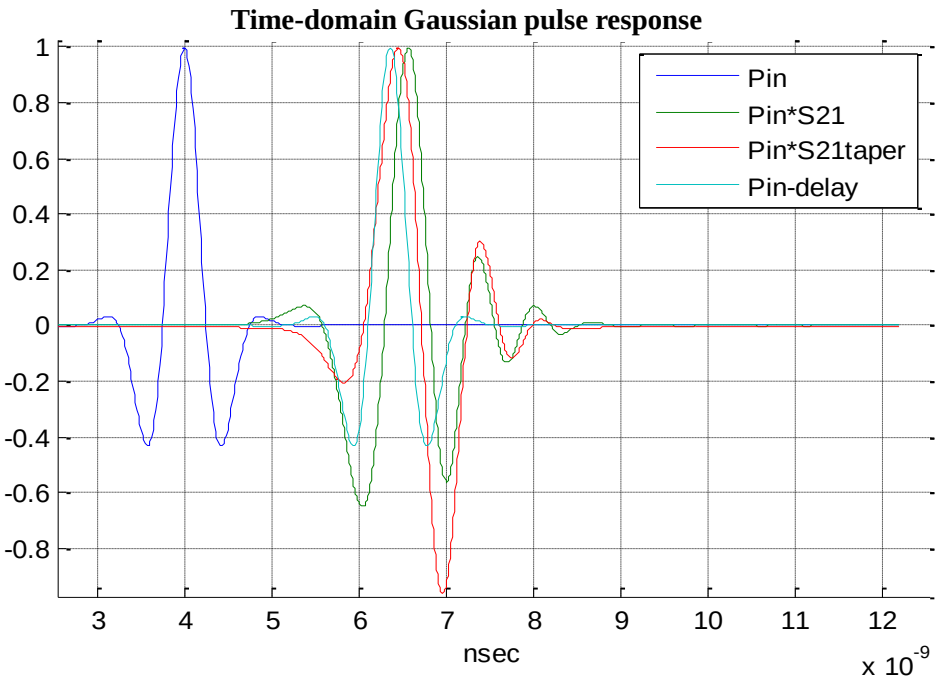

Figure 4.17: Time-domain pulse transmission through a pair of identical elliptical dipoles, radius = 23mm, axial ratio = 1.35: expected output pulse with tapering added

For all the time-domain simulations reported so far, the 'input' pulse shown in Figure 4.2 was arbitrarily selected. However, for practicality of antenna measurements with a vector network analyzer (VNA), a Gaussian pulse is used. When a Gaussian pulse is applied, effect of tapering is shown in Figure 4.17. In the future, a full-fledged active microwave system needs to be built with arbitrary pulse waveform generation capability.

In summary, the optimum antenna design for free-space radiation has a minor radius of 23mm, axial ratio of 1.35 and tapering factor of 26mm.

4.4 'Free-space' Imaging Antenna Results

Proceeding with the hardware implementation of the imaging antennas, two prototype antennas were fabricated on Rogers TMM6. This first set of antennas was optimized to radiate into free space. These antennas were meant to serve as the intermediate step to-

ward the final imaging antenna design, which will be optimized to radiate inside the tissue coupling medium. Figure 4.18 shows the physical details of the UWB antennas. Among the challenges to be solved with these air-prototype antennas were the fabrication details. As with any antenna fabrication, the details of coupling energy from the signal source to the radiating element(s) need careful design. As the required bandwidth of the antenna increases, the design of the antenna feed becomes a more critical part of the antenna. The approach taken here was to maintain TEM signal propagation up to the direct feed points of the two radiating tapered ellipses. At the feed point, however, the coaxial line provides an unbalanced coupling. A 'balun' was then added to reduce leakage current on the coaxial line's outer conductor. Simulation results showed that the best leakage current return is via a balun that is fed into the center of the 'positive voltage' radiating ellipse. The S-parameters were measured using a vector network analyzer, Agilent N5230A PNA-L . For practicality of measurements, a Gaussian pulse was used. The measured received pulse as shown in Figure 4.19, showed the low-dispersive behavior of the tapered elliptical dipole antenna. The transmitted 1.23ns pulse is spread to 1.32ns at the receiver which is an 7% spreading, while the non-tapered antennas would spread the pulse by 8.5%. Although this difference may seem insignificant, it is not negligible when antennas are adapted to radiate inside the liquid coupling medium (see experimental results discussion in Chapter 6).

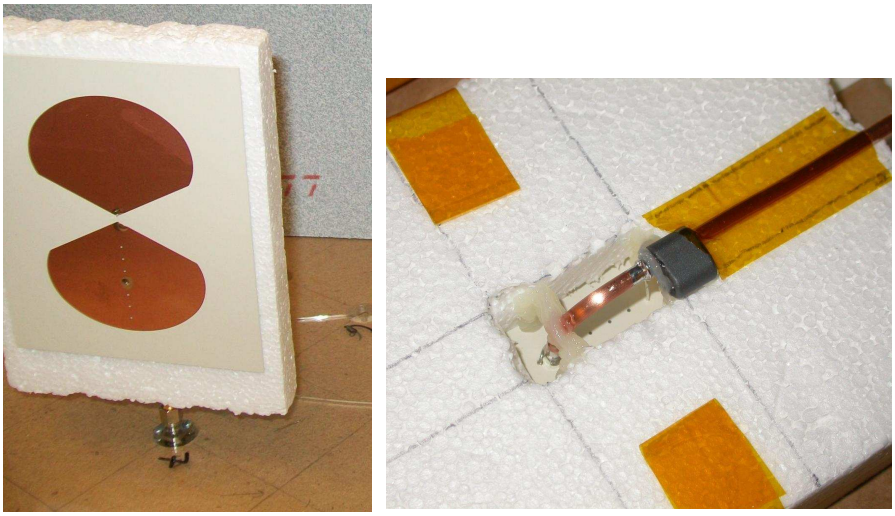

Figure 4.18: Imaging Antenna: on Rogers TMM6 substrate

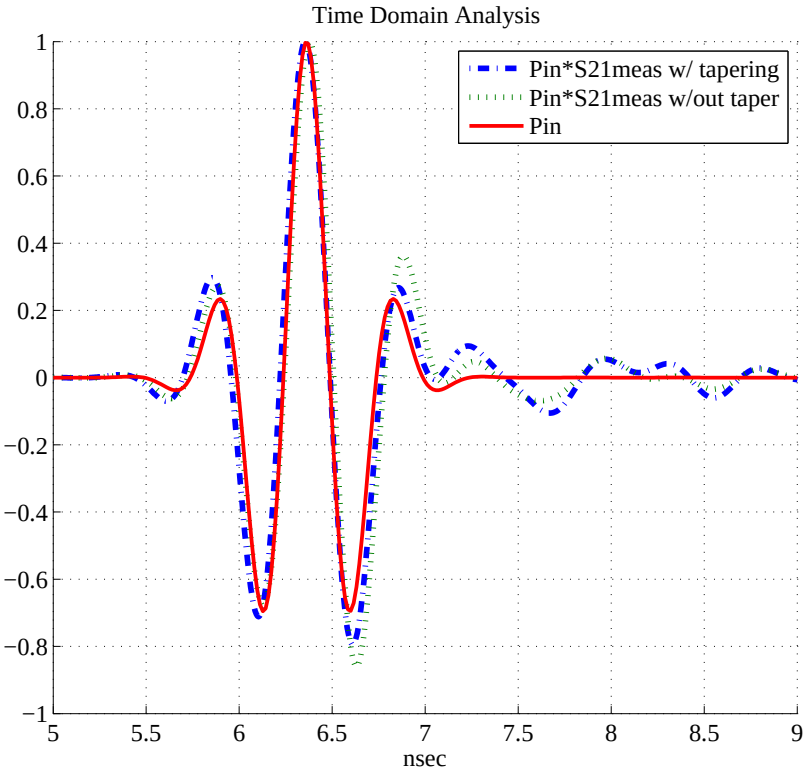

Figure 4.19: Measured Received Pulse, with and without taper added

4.5 Imaging Antenna Design Adaption and Results - In Coupling Medium

With the air-prototype UWB antennas results showing acceptable low-dispersive behavior, the work progressed to optimize the UWB antenna to radiate inside a tissue coupling medium. As shown Figure 5.1 - in verification of the findings of others [21] [27] [35]- signal mismatch losses at the air-skin interface is too large to allow microwave signals to propagate to any useful depth for imaging into the breast tissue. The objective was to adapt the free-space design of the tapered elliptical dipoles to radiate in a medium with permittivity similar to the skin interface ε_{skin} = 35. Following the same steps as the air-prototype antenna design, the first parameter to be studied was the radius. With antenna size largely determined by the radiation environment, and because progress in the coupling medium design was on-going in parallel, the strategy was to optimize antenna radius to operate in a range of $25 < \varepsilon_{couplingmedium} < 35$. The design specifics of the coupling medium are discussed in Chapter 5 of this thesis.

To start, the antenna size was directly scaled from its optimum free-space design to sizes for optimum radiation in the coupling medium. In the process of simulating the first few cases of radius optimization in a lossy coupling medium environment, it was observed that simulation run-time was too long for practicality. In attempt to reduce simulation run-time, the effect of conductive losses of the coupling medium on the antenna's input match was studied. HFSS simulation of two identical antennas placed in a lossy and lossless coupling medium showed little effect on S11 phase and magnitude of the coupling medium's conductive losses, see Figure 4.20. Simulation run time was, however, significantly longer when the radiation box has conductive losses. The conductive losses were therefore not taken into account in the initial HFSS design optimization of this adapted antenna design, so as to be able to perform a comprehensive parametric design study to arrive at optimum antenna radius, axial ratio, and tapering factor. Once the optimum antenna design was

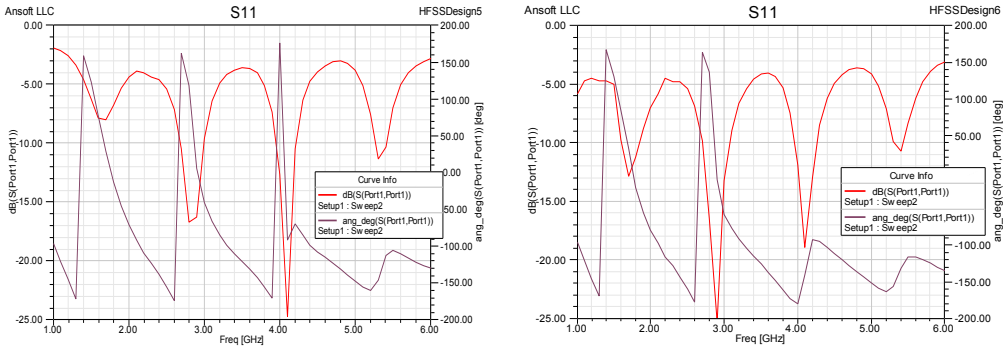

Figure 4.20: Simulated S11, magnitude and phase, when antennas radiate inside coupling medium: [left]=lossless, [right]=lossy)

determined, the conductive losses of the coupling medium were taken into account in the simulations of through signal propagations to further verify expected antenna performance. One more note, the 'fast' frequency sweep analysis was employed throughout the design iterations of the coupling-medium antennas for the practicality of shorter HFSS simulation run-time. For comparison charts between simulated and measured data as shown in Figures 4.26 to 4.33, 'discrete' frequency sweep analysis was employed to generate the 'simulated' results. In general 'discrete' frequency sweep analysis would give more accurate results, but the simulation run-time was simply prohibitively time-consuming for the number of parametric design cases needed to be studied for the antenna design adaptation.

Proceeding with the design trade to determine optimum antenna radius, Figures 4.21 and 4.22 show the simulation results of antenna input match for $\varepsilon_{couplingmedium}$ = [25, 35]. Larger radii values (5mm $<$ radius $<$ 12mm) were studied for the lower permittivity value of 25 and and smaller radii values (4mm $<$ radius $<$ 10mm) for permittivity of 35. The conclusion was to select an antenna minor radius of 10mm, which showed the best linearity in the frequency range of interest and the optimum compromise in magnitude of input match.

Once radius was determined, next came the iterative process to determine the optimal axial ratio and tapering factor. First set of simulations aimed to determined whether smaller

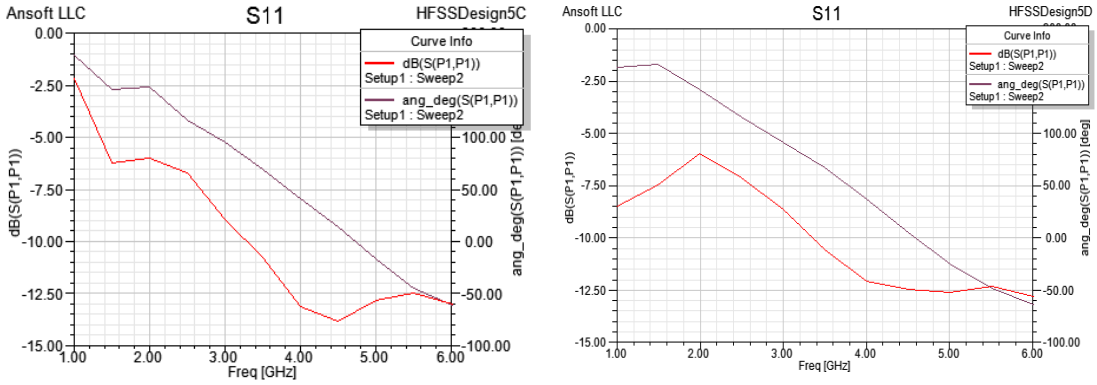

Figure 4.21: Simulation data for $\varepsilon_{couplingmedium}$ = 25, radius was varied from 5mm [left] to 12mm [right]

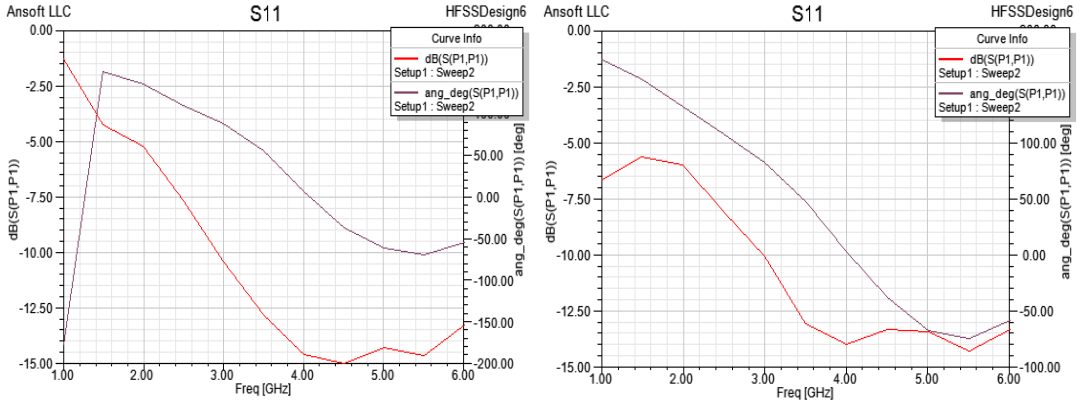

Figure 4.22: Simulation data for $\varepsilon_{couplingmedium}$ = 35, radius was varied from 4mm [left] to 10mm [right])

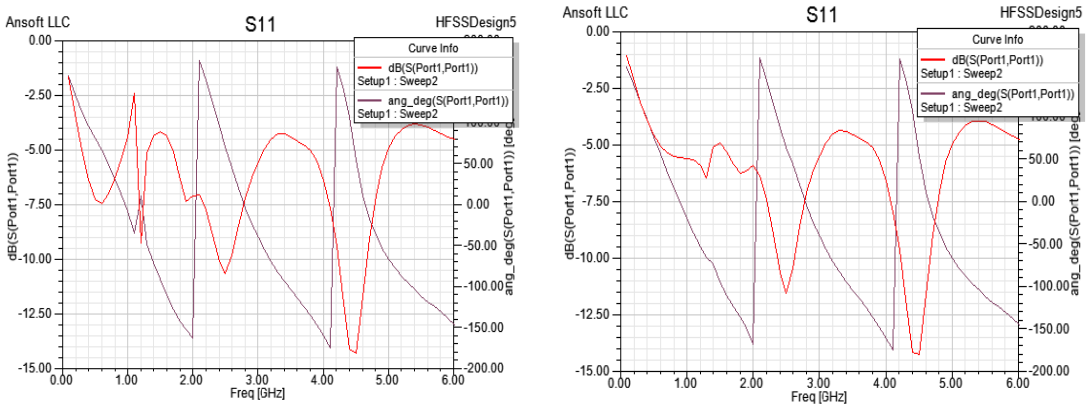

Figure 4.23: Simulation data for axial ratio study, minor radius = 10mm, no tapering factor: axial ratio = 1.35 [left] to axial ratio = 1.75 [right]

or larger axial ratio would result in good input match without compromising phase linearity over the frequency band of interest. Then optimum tapering factor was studied at various fixed axial ratio with fixed radius. These two steps are repeated to arrive at the optimum axial ratio and tapering factor. Keeping a fixed radius and without any tapering, results in Figure 4.23 show that the higher axial ratio of 1.75 is preferred. Setting axial ratio at 1.75, keeping minor radius at 10mm, a range of tapering factor was applied, see Figure 4.24. With the 'free-space' antenna, best tapering factor was 26mm. However, for the antennas to be used inside the coupling medium, the higher tapering factor showed non-linearity in the 1-2 GHz range, see Figure 4.24 . Tapering factor of 16mm was then selected for the next iteration of axial ratio. Keeping the tapering factor at 16mm and radius at 10mm, the next iteration showed optimum axial ratio to be 1.55, Figure 4.25. The final antenna design parameters are then: minor radius = 10mm, axial ratio = 1.55, tapering factor = 16mm. It should be noted that the optimum axial ratio shifted from 1.35 for the 'free-space' antennas, to 1.55 for the final antenna to be used with coupling medium. Similarly, the optimum tapering factor shifted from 26mm for the 'free-space' antennas to 16mm for the final antennas. As work on the coupling medium was on-going in parallel, the final antenna designs did not take into account the conductive losses of the coupling liquid.

Proceeding to the building of the final antennas, four antenna designs were fabricated

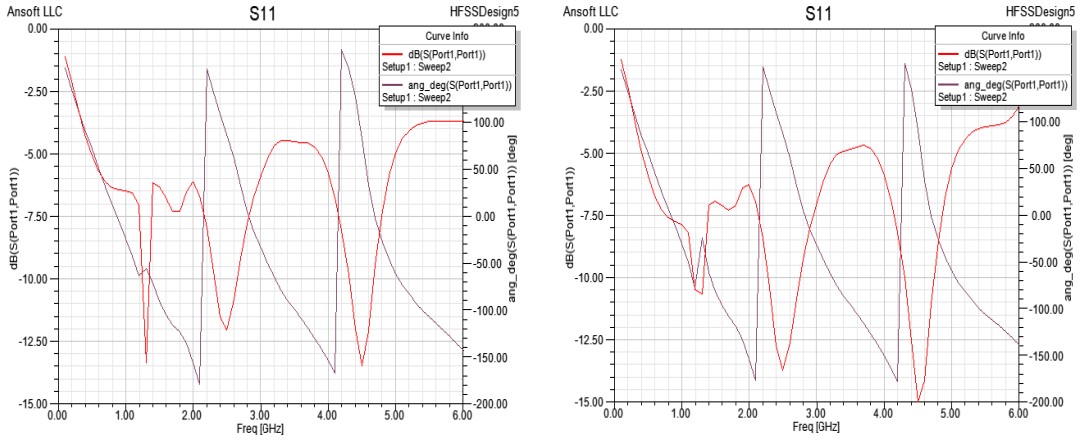

Figure 4.24: Simulation data for tapering factor study, minor radius = 10mm, axial ratio = 1.75: tapering factor = 16mm [left] to tapering factor = 25mm [right]

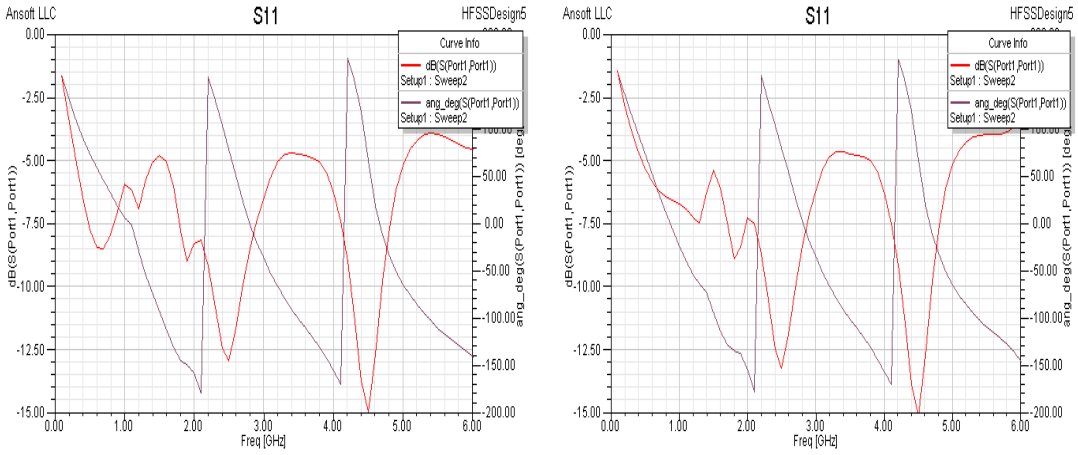

Figure 4.25: Simulation data for axial ratio study, minor radius = 10mm, tapering factor = 16mm: axial ratio = 1.35 [left] to axial ratio = 1.55 [right]

- primarily to plan for potential unknown factors associated with the coupling medium. Specifically, a pair of each of these four designs were fabricated: minor radius = 8mm and 10mm, with tapering factor of 16mm and 26mm for each of the two antenna sizes. Potential unknowns associated with the coupling medium at the time of the antenna fabrication included: permittivity variability among the one-liter batches of emulsion, emulsion chemical stability over time, permittivity stability over time (emulsions are produced in one-liter batches over a period of several weeks). Details on the coupling medium emulsion will be discussed in the next chapter.

Antenna measurements were made with antennas submerged in a tank filled with coupling medium having permittivity and conductivity characteristics as shown in Figures 5.22 and 5.23. Figures 4.26 to 4.33 show the measured antenna data compared to simulated results. For the simulated results shown in these charts, dielectric properties of the coupling medium were included so proper comparisons can be shown. The S11 magnitude plots show a consistent frequency off-set with all four antenna designs, but in general the measured data are in acceptable agreement with the simulated results. The measured S11 phase data showed better agreement with the simulated results, for all four antenna designs. Discussions on the dispersion behavior of these antennas will be presented in Chapter 6.

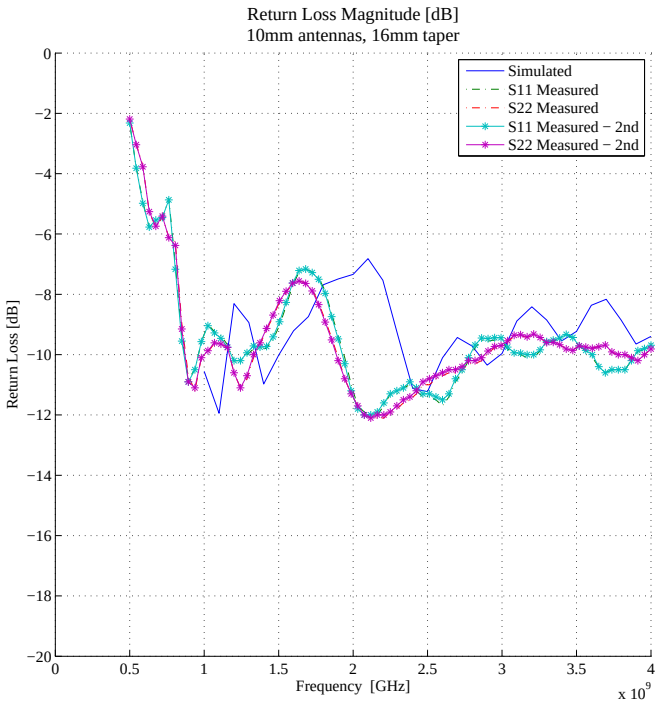

Figure 4.26: S11 [magnitude]: Measured vs. simulated: minor radius = 10mm, taper = 16mm

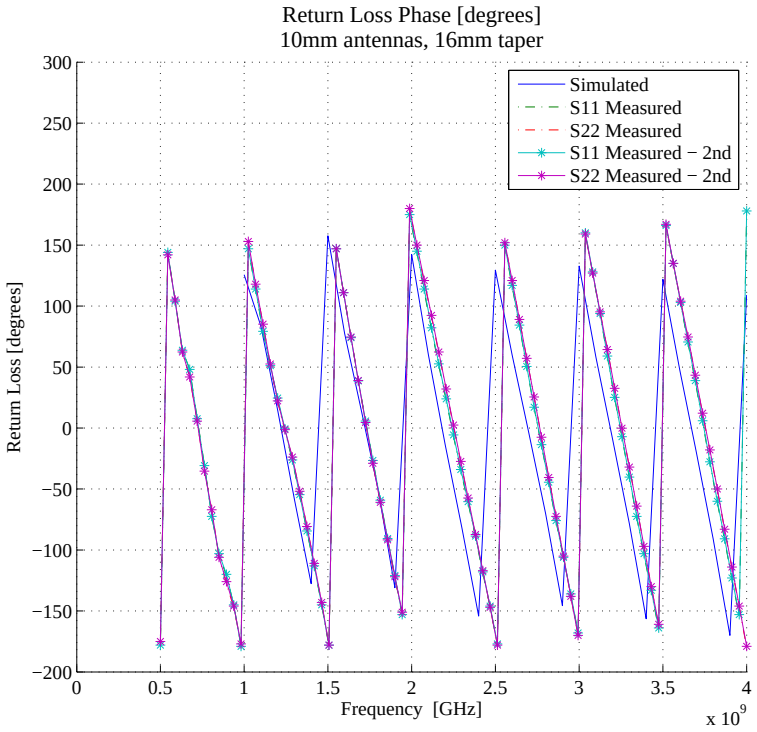

Figure 4.27: S11 [phase]: Measured vs. simulated: minor radius = 10mm, taper = 16mm

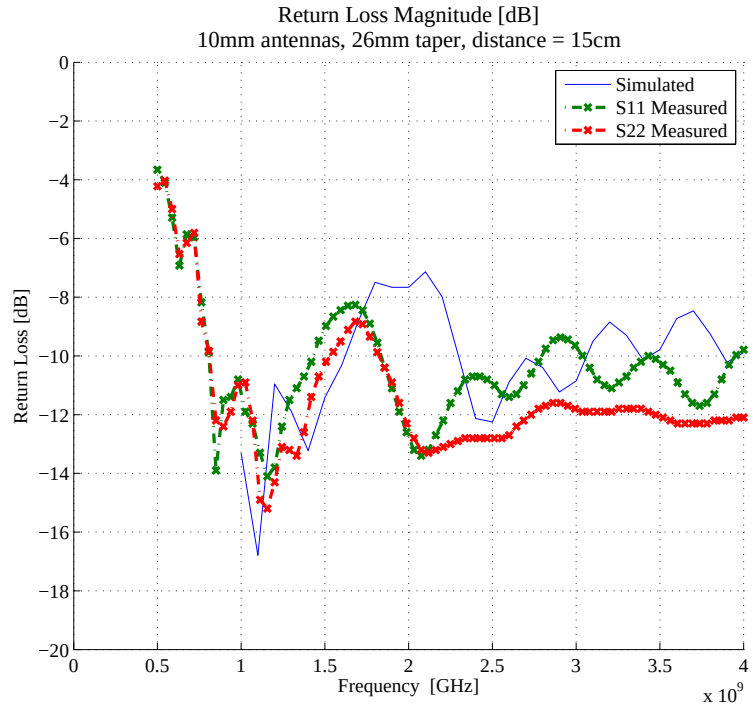

Figure 4.28: S11 [magnitude]: Measured vs. simulated: minor radius = 10mm, taper = 26mm

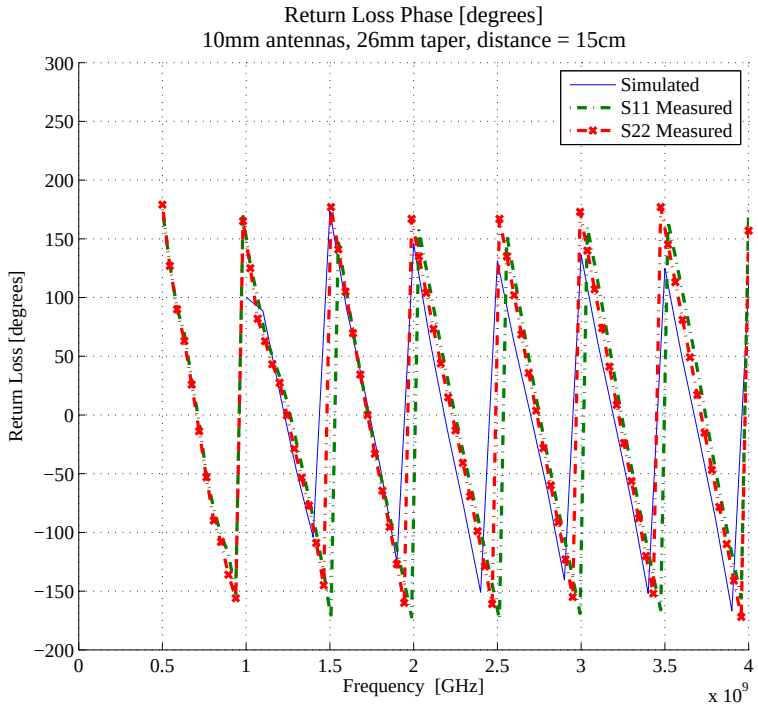

Figure 4.29: S11 [phase]: Measured vs. simulated: minor radius = 10mm, taper = 26mm

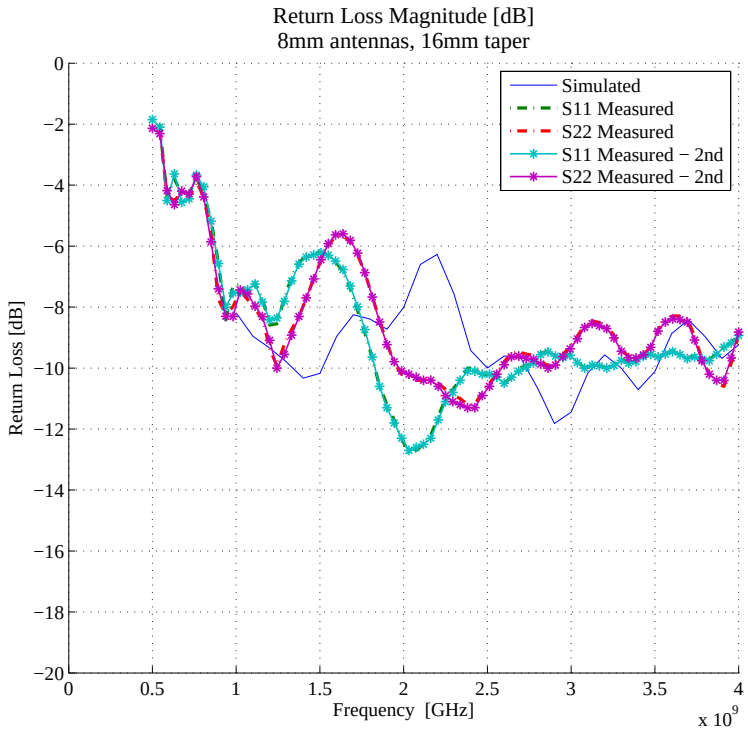

Figure 4.30: S11 [magnitude]: Measured vs. simulated: minor radius = 8mm, taper = 16mm

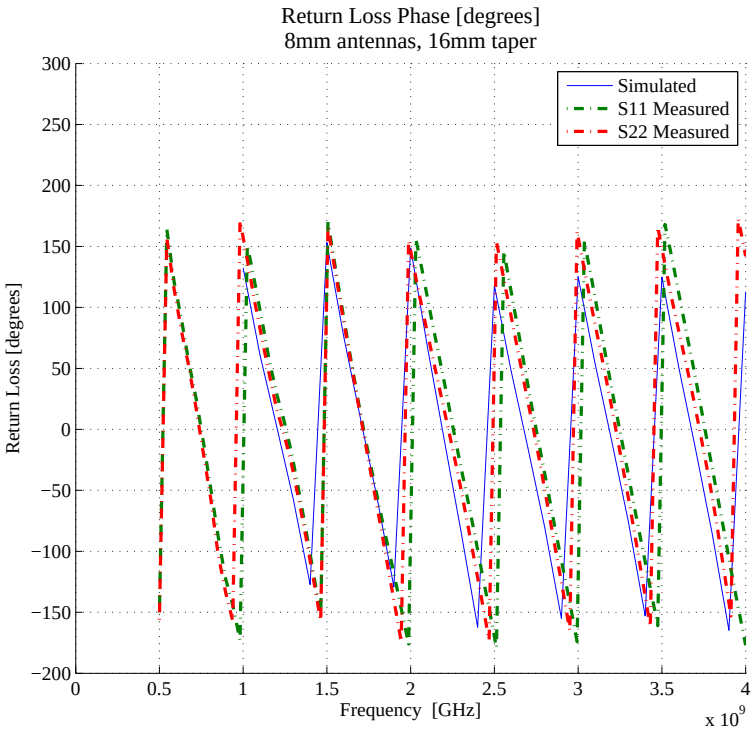

Figure 4.31: S11 [phase]: Measured vs. simulated: minor radius = 8mm, taper = 16mm

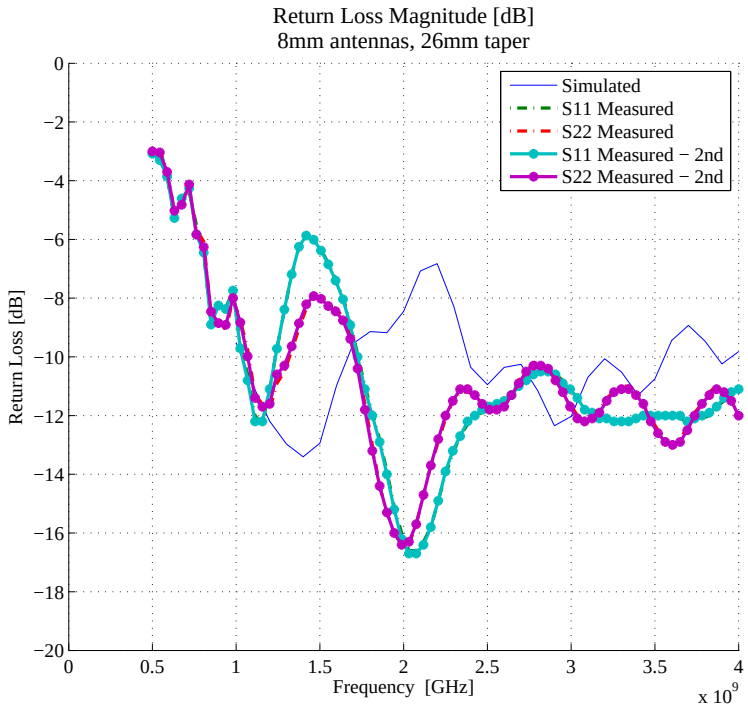

Figure 4.32: S11 [magnitude]: Measured vs. simulated: minor radius = 8mm, taper = 26mm

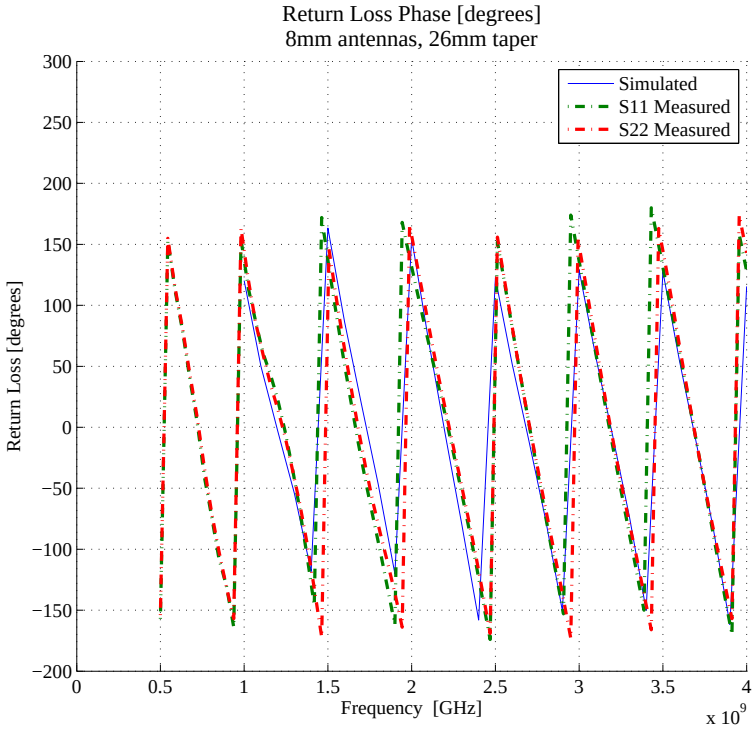

Figure 4.33: S11 [phase]: Measured vs. simulated: minor radius = 8mm, taper = 26mm

CHAPTER 5

Tissue Coupling Medium

This chapter details the research and empirical development of the next critical component of the microwave imaging system: the tissue coupling medium. The purpose of the coupling medium is to reduce signal losses due to mismatch scattering between air and skin. As many previous studies have reported [21] [27] [35], without a matching coupling medium, most of the signal source would be reflected at the air-skin interface. Simulation results (using the developed T-matrix based system analysis tool) summarized in Figure 5.1 illustrate that with a large mismatch in the permittivity of skin and the transmission medium, the embedded 'tumor' represented with a high dielectric constant sphere, cannot be distinguished. This is the case when the coupling medium is free-space. As permittivity of the coupling medium approaches that of the skin's (the last two curves in Figure 5.1), the tumor-mimicking spheres begin to able to be detectable.

A secondary potential application for this coupling medium is for combined microwave and ultrasound imaging. It would be desirable to develop one coupling medium which can be used for imaging purposes in both modalities. For the ultrasound application, low viscocity is desired. The research effort began with the verification of a reliable dielectric measurement methodology, followed by dielectric properties study of commercial products, focused on the formulation of liquid coupling medium, then proceeded to mass produce the coupling medium for the MWI system.

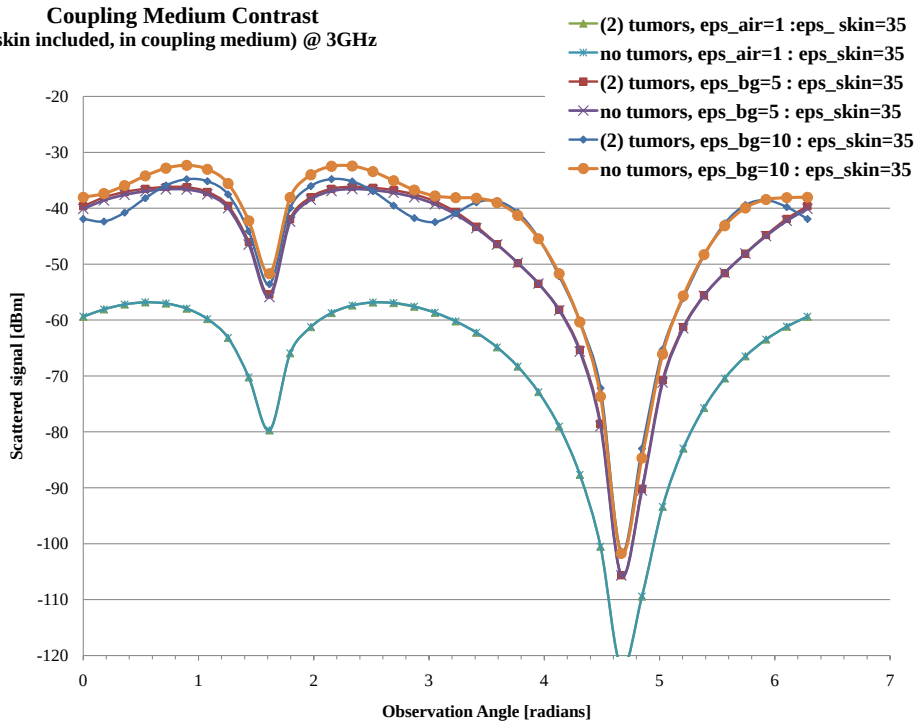

Figure 5.1: System analysis simulations show that permittivity of coupling medium must be matched to that of the skin's permittivity value.

The task at hand is to incorporate a coupling medium in the imaging system to minimize signal scattering losses due dielectric constant mismatch at the air and skin interface. ε_{skin} was measured to be ~ 35 [10] [11] [12]. When the incident field is coupled through 'free-space' medium, most of the signal would be scattered at the air-skin interface. The objective is to couple most of the incident power through the skin into the internal breast tissue, and measure the scattered signals due to the potential target tumors inside the breast tissue. The permittivity of the coupling medium should be designed to match the skin's permittivity. Having a compatible permittivity values to the skin is one requirement - the more difficult criteria to meet for this coupling medium is low conductive losses. Ideally, the coupling medium should be lossless. The commonly used coupling medium seems to be oil [2] [22] [23]. However, oil has a low permittivity value, in the $\varepsilon_{oil} \sim 2.5$, see Figure 5.5. Lastly, the physical properties of the coupling medium are driven by practical clinical issues: non-toxic for patients' skins, compatible with in-vivo imaging. The latter property implies

substances that are of liquid or gel forms rather than solids.

The research effort began with measuring liquids known to have the most lossy and least lossy properties in the microwave frequencies, namely water and oil respectively (see Figures 5.2 to 5.5). Part of the motivation of starting with well-quantified liquids, is the establishment of a reliable dielectric measurement technique. The Agilent Dielectric measurement kit was acquired for this purpose. The measurements of the various coupling medium samples were done using the Agilent Slim Form Probe.

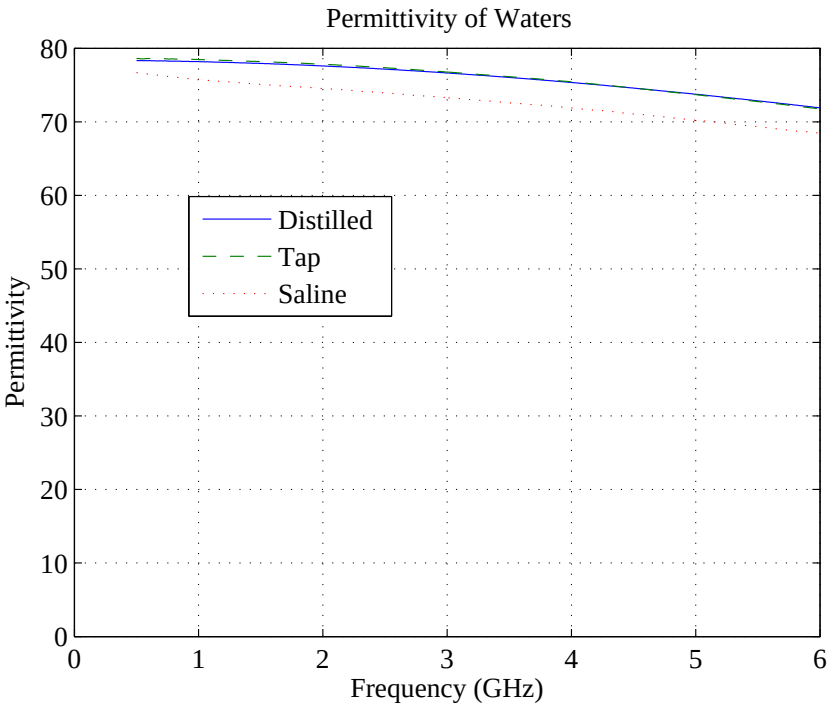

Figure 5.2: Relative permittivity of waters

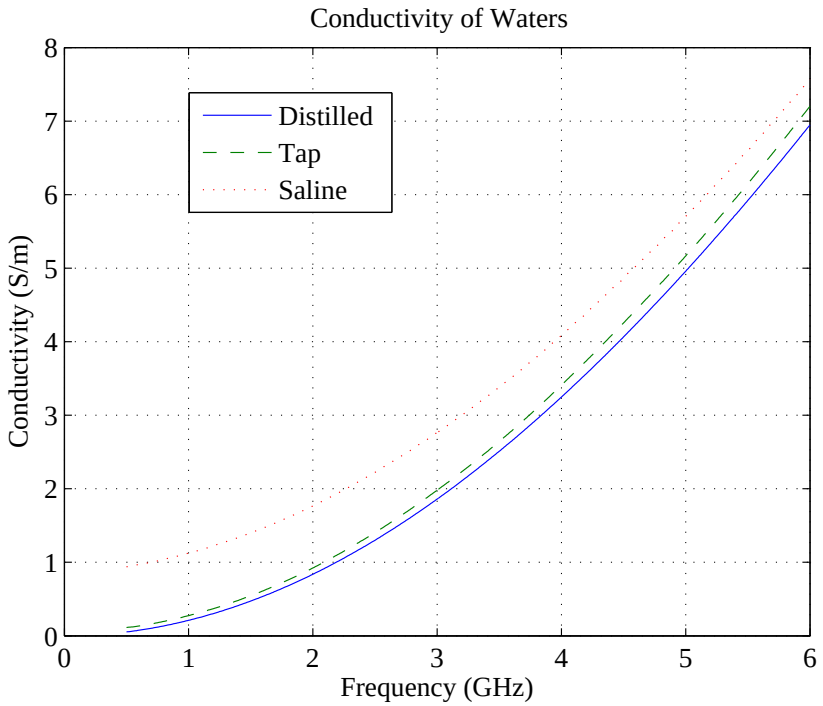

Figure 5.3: Conductivity [S/m] of waters

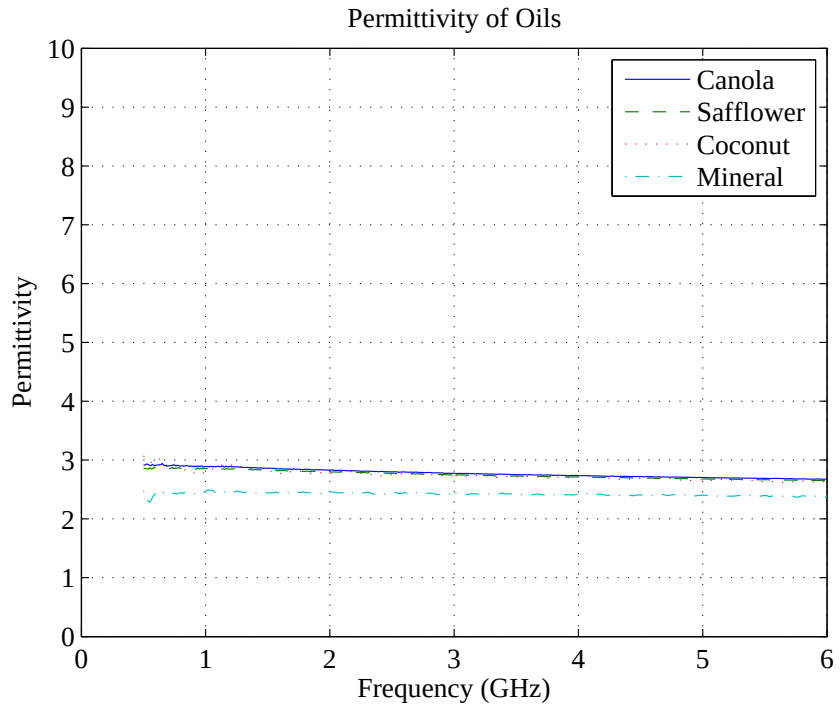

Figure 5.4: Relative permittivity of oils

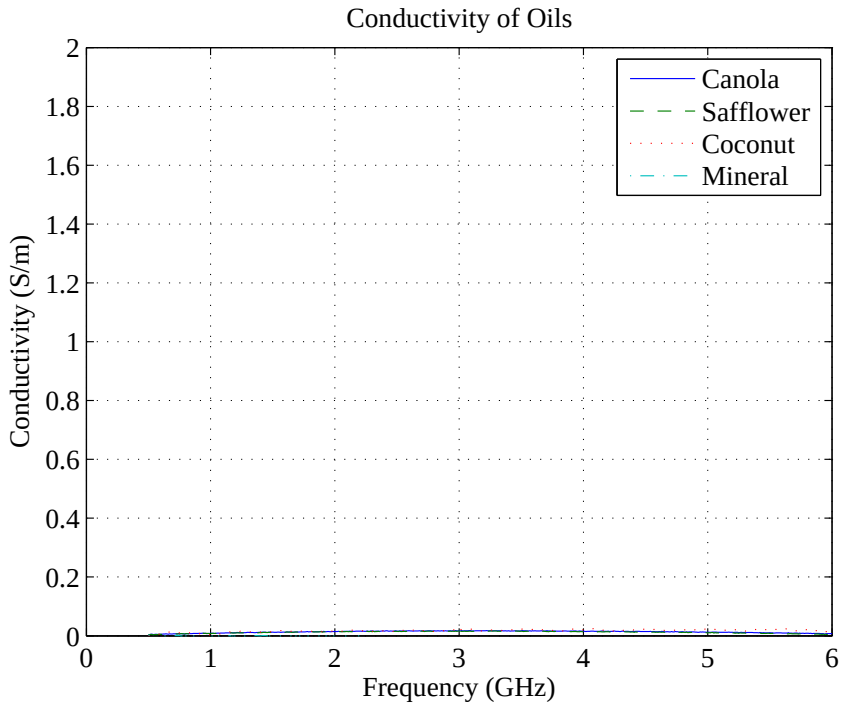

Figure 5.5: Conductivity [S/m] of oils

5.1 Dielectric Constant Data of Commercial Products

Proceeding forward, the strategy was to find a commercially available product which would have the required microwave permittivity and conductivity properties as detailed above. The idea here is that commercially available products have already gone through consumer safety inspection. A variety of personal care products and other household products were tested. Measured permittivity and conductivity data are included below. These measured data are consistent with expected results. Specifically, those products with water listed as the first ingredient, tend to have high permittivity values. Those products containing a significant percentage of oil would measure lower permittivity values.

This empirical study of measuring commercially available products did produce a handful of candidates for the imaging system's coupling medium. These candidates include a set of conditioners as shown in Figure 5.8, and the sunscreen lotion included in Figure 5.10. The conditioners have measured permittivities in the neighborhood of the skin's permittivity. However, their measured conductivities are not linear. This non-linearity would translate to increased dispersive behavior of the imaging system. The most promising candidate is the Coppertone Waterbabies SPF50 in Figure 5.10. The multiple unsuccessful attempts to secure donations from Coppertone and various local vendors only support the case of formulating an in-house coupling medium which can be economically mass produced. The sunscreen cost is about $1/oz. A more complete documentation of measured dielectric properties of various commercial products are included in the appendix section of this thesis. Design details of the coupling medium will follow in the next section.

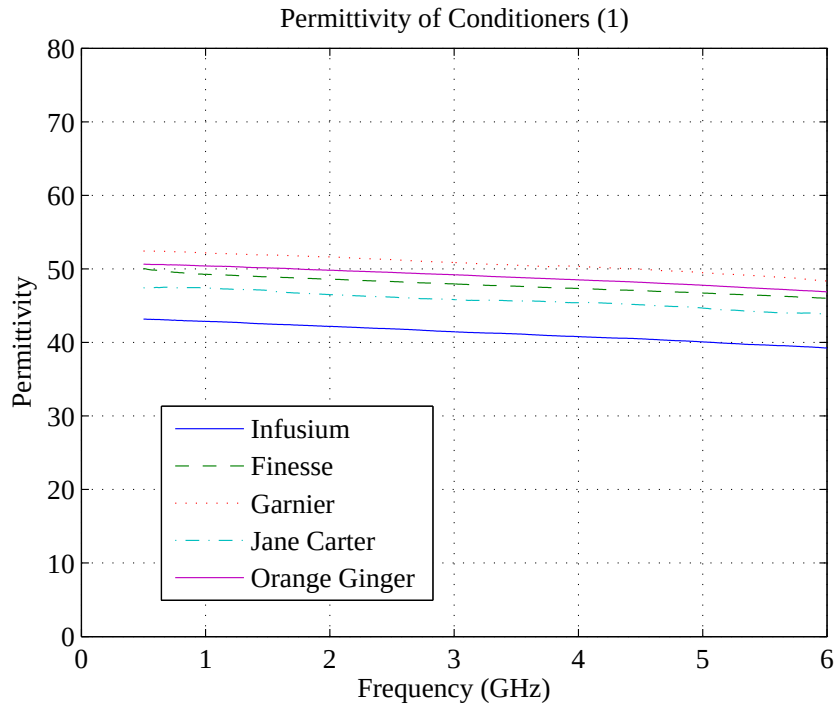

Figure 5.6: Relative permittivity of commercially available hair conditioners

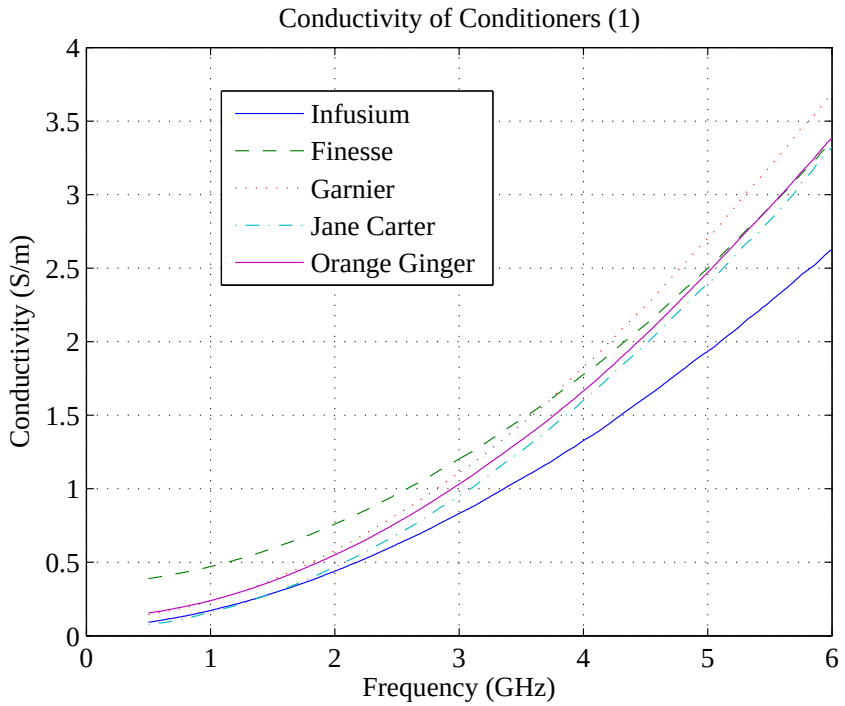

Figure 5.7: Conductivity [S/m] of commercially available hair conditioners

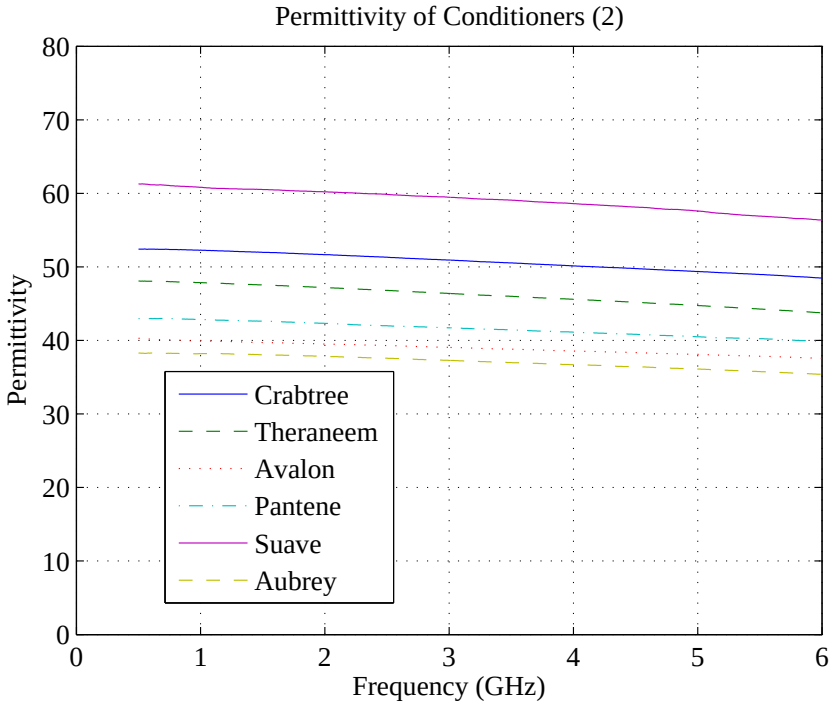

Figure 5.8: Relative permittivity of commercially available hair conditioners

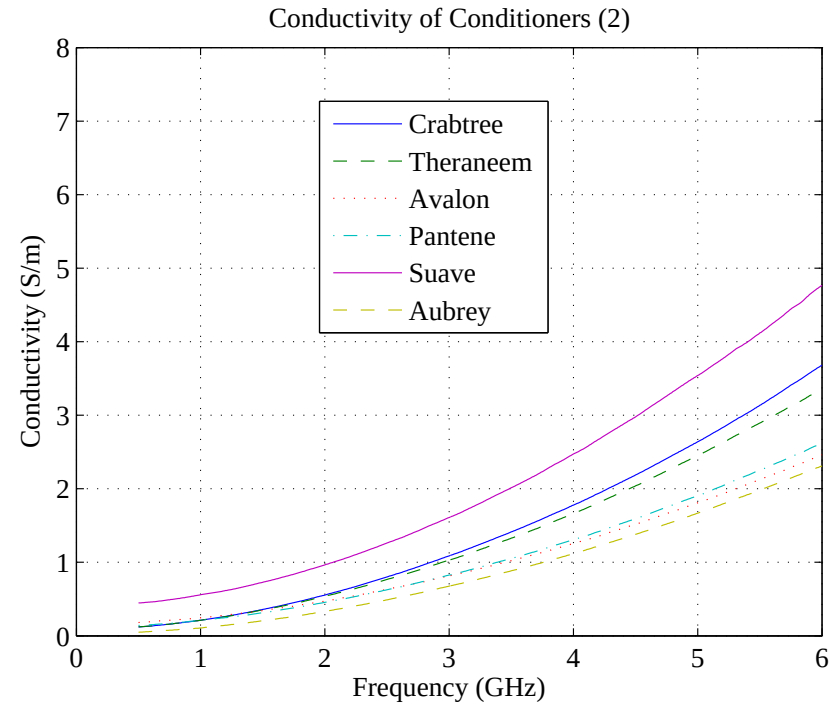

Figure 5.9: Conductivity [S/m] of commercially available hair conditioners

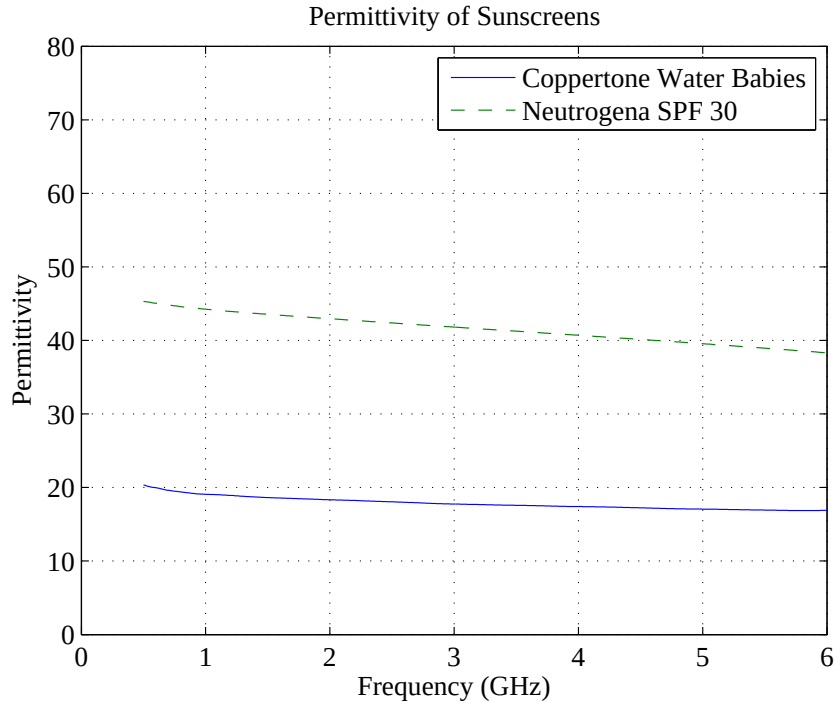

Figure 5.10: Relative permittivity of commercially available sunscreen lotions

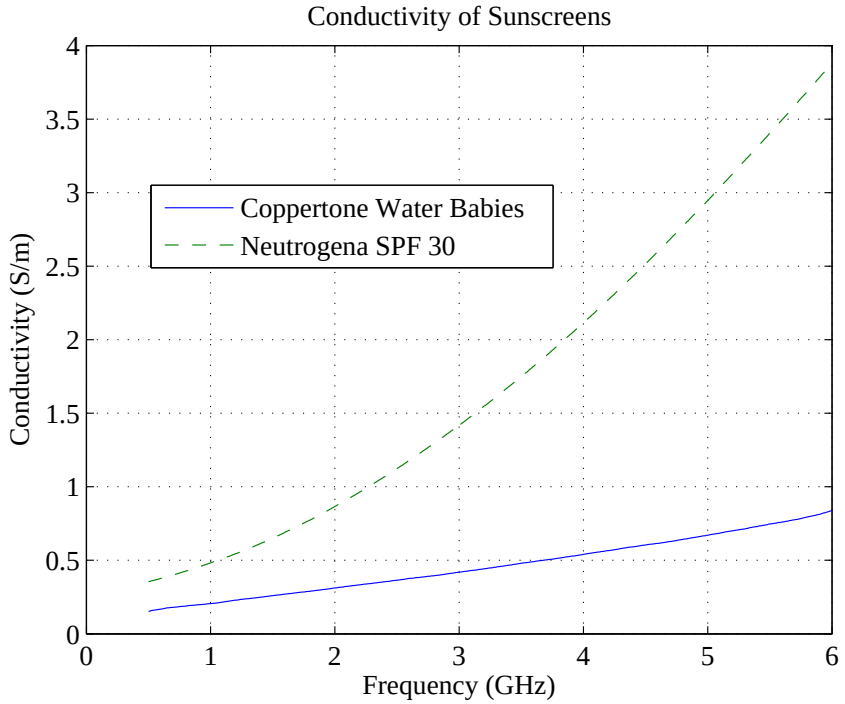

Figure 5.11: Conductivity [S/m] of commercially available sunscreen lotions

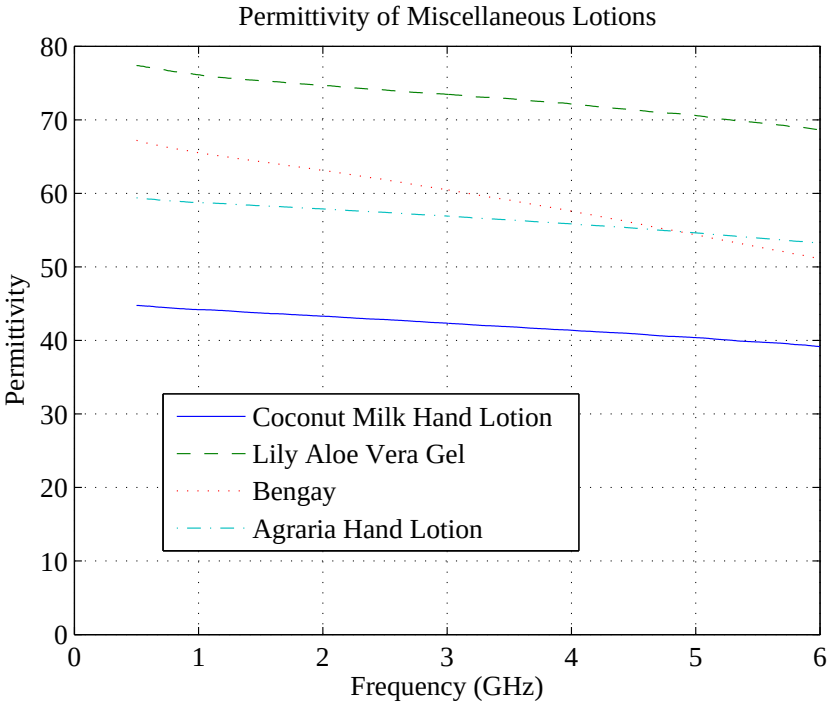

Figure 5.12: Relative permittivity of miscellaneous lotions

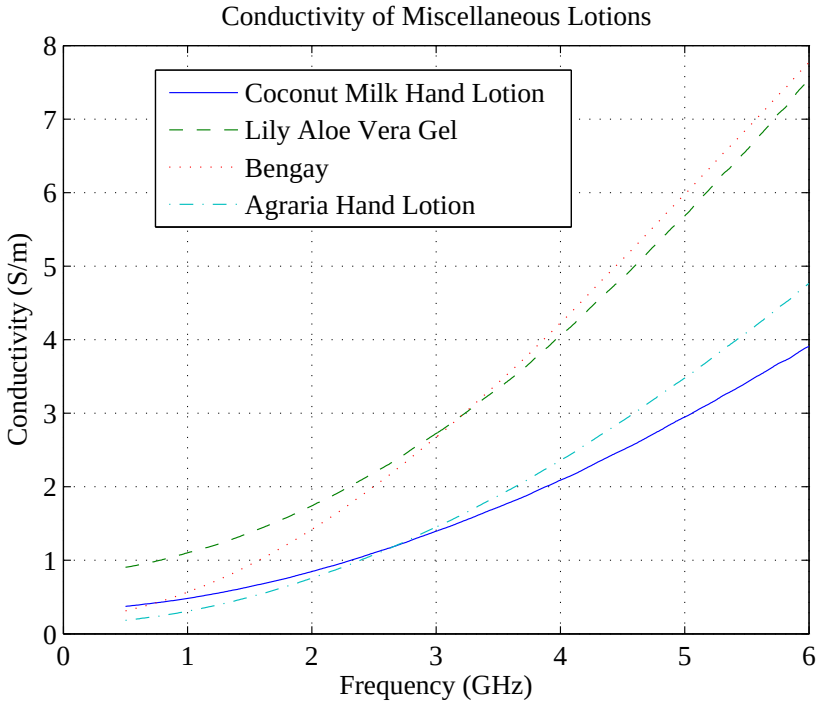

Figure 5.13: Conductivity [S/m] of miscellaneous lotions

5.2 Empirical Design of Tissue Coupling Medium

From these measured dielectric properties of commercial products, coupled with cost and availability issues, the focus of the research was directed to empirically design a liquid coupling medium. The two overriding factors for designing our own tissue-coupling-medium optimized for microwave imaging, are cost and commercial product availability. These commercial products are costly to procure, on the average, they cost $0.20 to $5 per fluid ounce. The imaging tank would need about 960 fluid ounces to fill. In the clinical setting, cost can perhaps be negotiated. The potentially more challenging factor is product availability. The progress of this research depends on the vendor offering of the commercial product of choice. Should the product be discontinued or changed in its chemical formulation, then the choice of the commercial product becomes obsolete. One additional motivation for developing our own imaging coupling medium is to attempt to develop a more viscous coupling medium - for potential dual-modality imaging application with ultrasound. The commercial product with the best dielectric properties for microwave imaging, namely the Coppertone Waterbabies SPF 50 sensitive 'pure and simple', is thick. The viscosity is not useful for ultrasound imaging.

The empirical design process took the following steps:

1. Start with main ingredients of Coppertone sunscreen

2. Conduct a set of chemistry experiments with : ZnO, TiO_2, various binding agents such as PEG (polyethelene glycol, PPG (polypropylene glycol), glycerin and water mixtures

3. Converge on oil-water mixtures with various proportions of hydrophilic-lipophilic factor (HLB) surfactants (HLB8, HLB10 and HLB12), using a handful of oil (Safflower, corn)

4. Repeat production of oil-water emulsion in 50ml batches, then in 1-liter batches.

5. Measure and collect dielectric data throughout the process

As expected with the water and oil mixture, higher water content increases permittivity and conductivity values, as observed in Figure 5.14. The proportion of surfactant seem to have little effect in both permittivity and conductivity of the emulsion, see Figures 5.16 and 5.17. These same data charts show that adding alcohol and sugar (manitol) increased the conductivity of the emulsion. Because lowering the percentage of water much below 50% (see Figures 5.14 and 5.15) does not seem to significantly decrease the conductivity, for ease of mass production it was decided to produce the 50% water - 50% oil emulsion. For completion, dielectric properties of the water and glycerin mixtures are included in Figures 5.20 and 5.21.

Up to this point, emulsion mixtures have been made in 50ml test tube batches. The next challenge is to prove that these mixtures can be produced in large-scale volumes. In producing the first 1-L batch, it was noted that sonification process would take an hour. Visual inspection of oil droplets on the surface of mixture was the method used to determine the completion of sonification. When mixing a 2-L batch was attempted, sonification time extended to nearly three hours. At this point, it was decided to proceed with the oil-water mixture production in 1-L batches. Several 1-liter batches were then produced and tested for dielectric properties repeatability.

Recipe for coupling medium emulsion: 500ml water, 500ml corn oil, 50ml HLB10 surfactant (46% volume Span80, 54% volume Tween80). The specific procedure for coupling medium production, 1-liter batch:

1. Centrifuge 500ml of water with 50ml of surfactant

2. Combine water and surfactant mixture with 500ml corn oil

3. Sonicate mixture for an hour

Measured data of the first set of liter batches are shown in Figures 5.18 and 5.19. Permittivity values range between 20-25, and conductivity values all fall below 0.5S/m at 3

GHz.

Once several liters of coupling medium emulsions were produced, they were combined in the imaging tank. Measurement of emulsion mix in the imaging tank are shown in Figures 5.22 and 5.23. The various lines on the chart reflect measurements taken on random locations inside the imaging tub (measurements taken with the Agilent Slim Form probe) to study the homogeneity of the mixture. More in depth discussion on this topic will follow in Chapter 6 where measurement results are presented.

Several observations should be noted here.

1. There is variation in permittivity values among the 1-liter batches. Several contributing factors include:

   (a) Manual production carries human error factor - sonification is done by hand

   (b) The viscocity of oil contributes to the repeatability of the amount of oil used - nearly impossible to drain the last bit of oil from measuring beaker

2. Chemical stability of the coupling medium needs further study. After 3-4 weeks, mold began to grow in the mixture. This issue was resolved by adding anti-bacterial and anti-fungal water treatment. Storing the coupling medium in refrigerators would help but not yet tested.

3. Particle size and density were tested for ultrasound imaging application, and was found to be adequate. This mixture appears to be too lossy for ultrasound imaging, however, likely due too high percentage of oil in the mixture. Average particle size is 1.6μm in diameter, density is 1 x 10E11 particles per ml, with 0.004% $>$ 10μm. Further work to quantify the acceptable ultrasound attenuation loss needs to be done, followed by studies into other water-oil formulations.

Although more work is necessary to meet the combined requirements of microwave and ultrasound imaging, the coupling medium developed here meets the requirements for MWI alone.

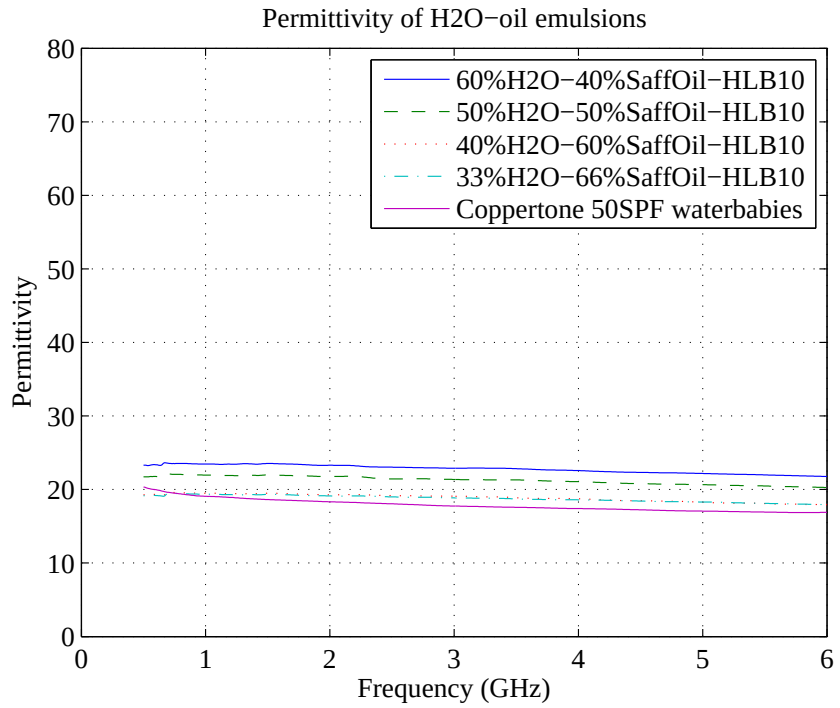

Figure 5.14: Relative permittivity of Water-Oil emulsions

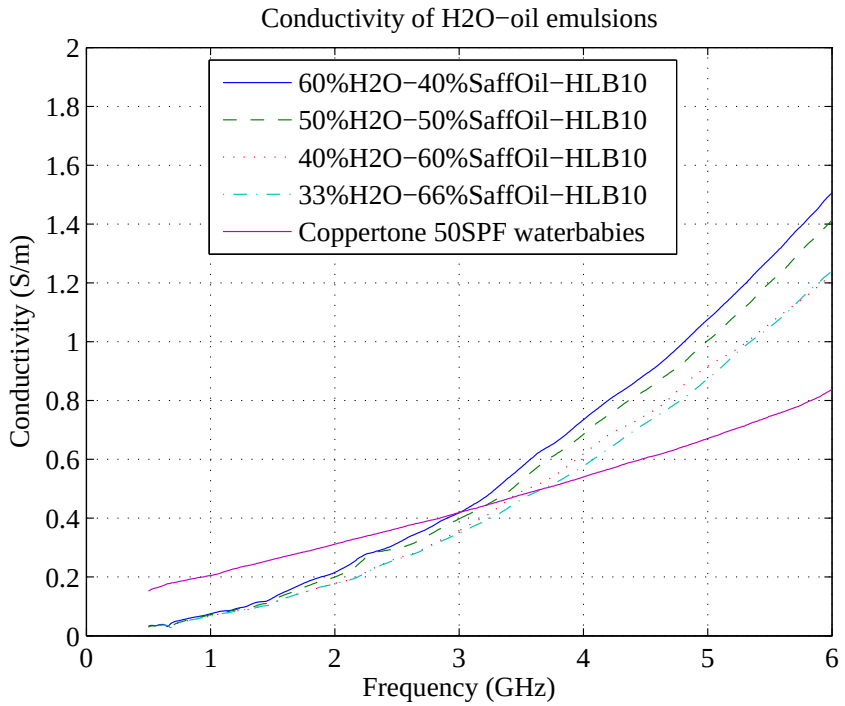

Figure 5.15: Conductivity [S/m] of Water-Oil emulsions

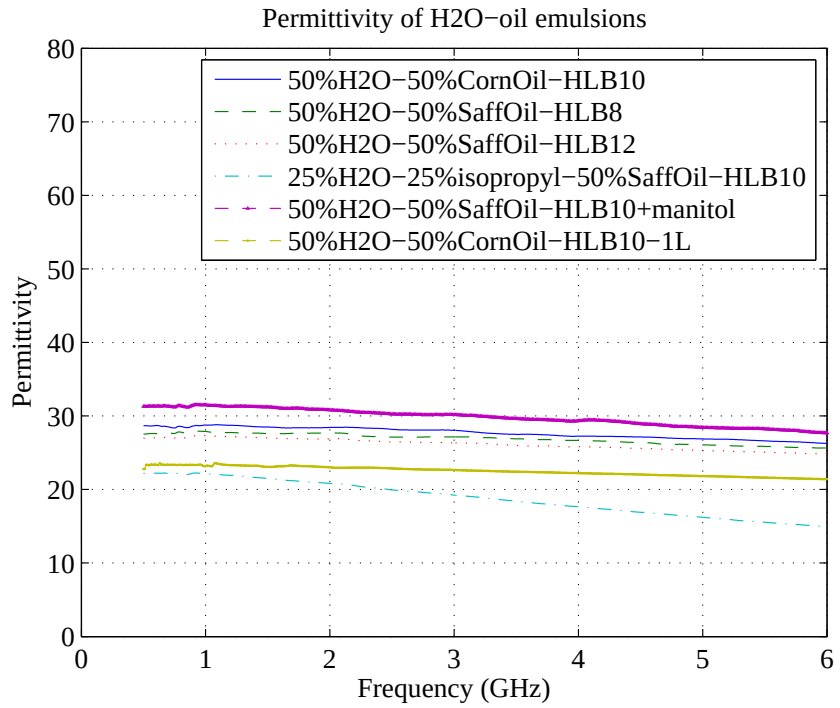

Figure 5.16: Relative permittivity of Water-Oil emulsions

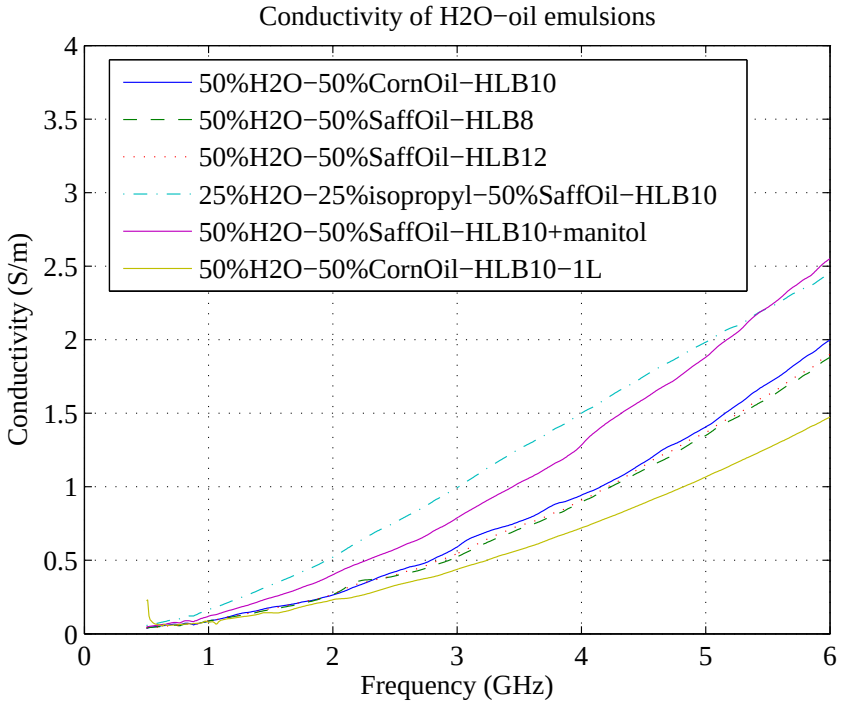

Figure 5.17: Conductivity [S/m] of Water-Oil emulsions

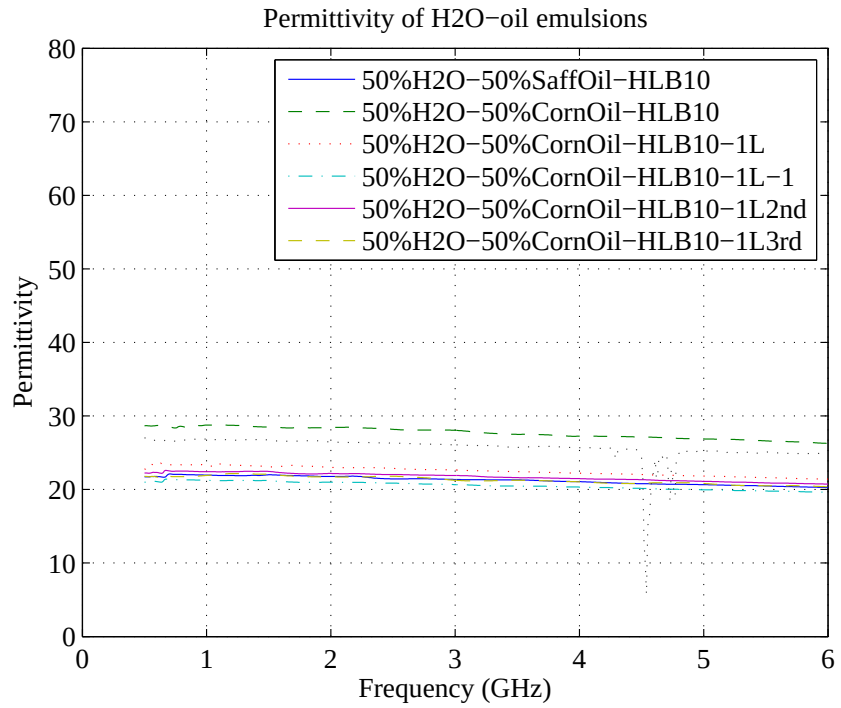

Figure 5.18: Relative permittivity of Water-Oil emulsions

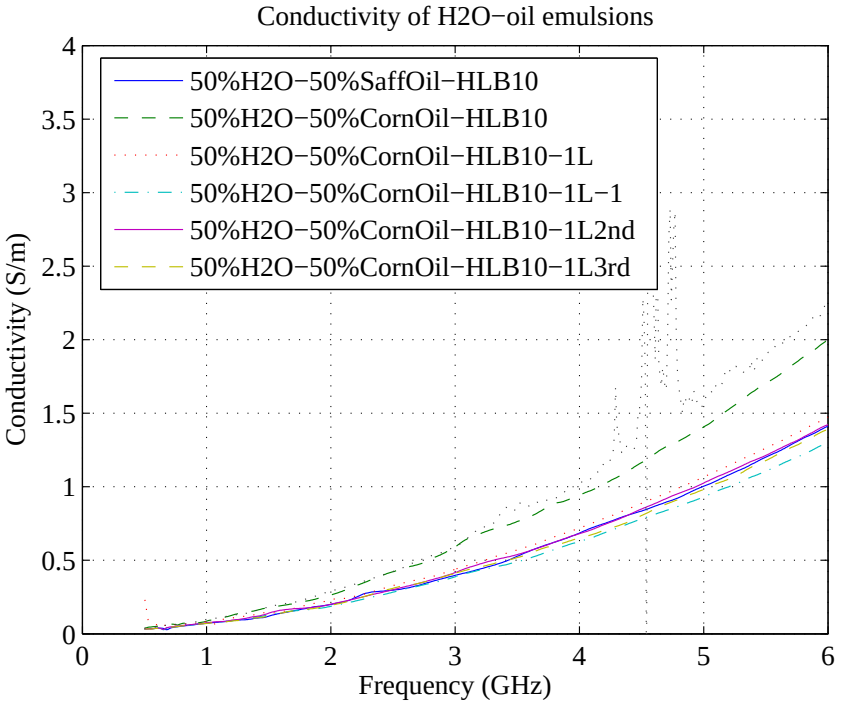

Figure 5.19: Conductivity [S/m] of Water-Oil emulsions

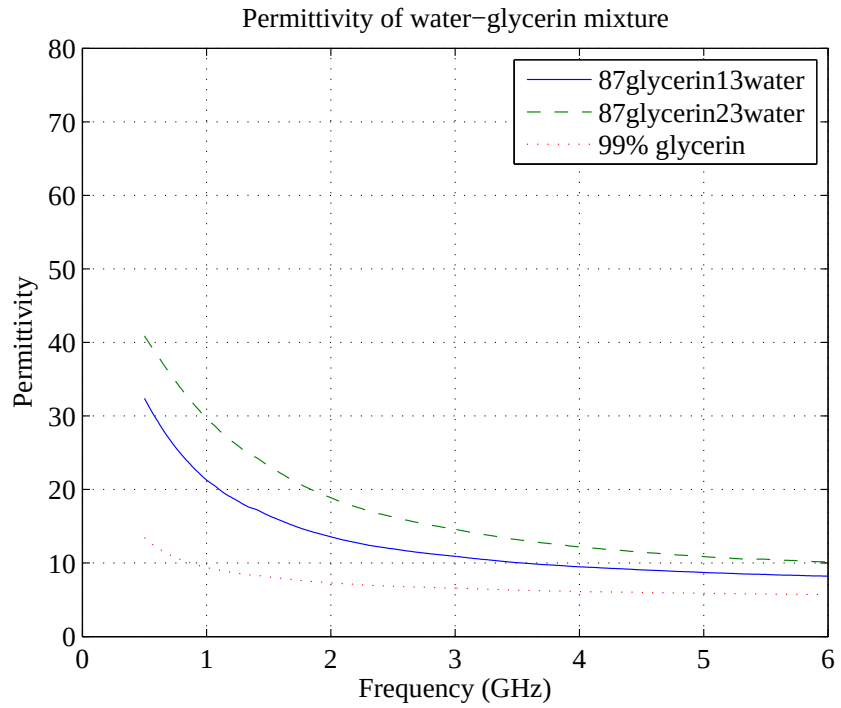

Figure 5.20: Relative permittivity of water and glycerin mixtures, and pure glycerin

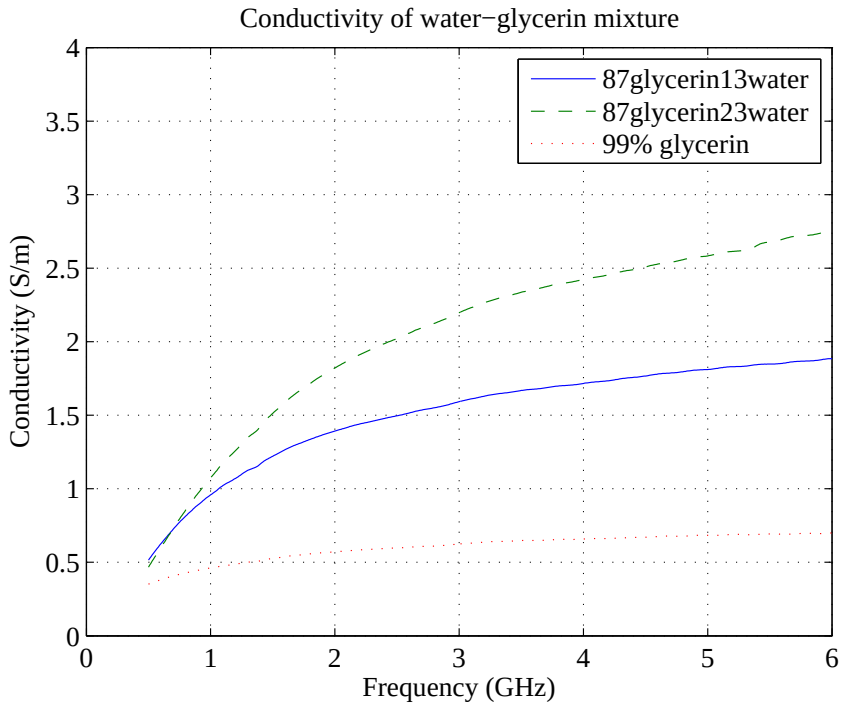

Figure 5.21: Conductivity [S/m] of water and glycerin mixtures, and pure glycerin

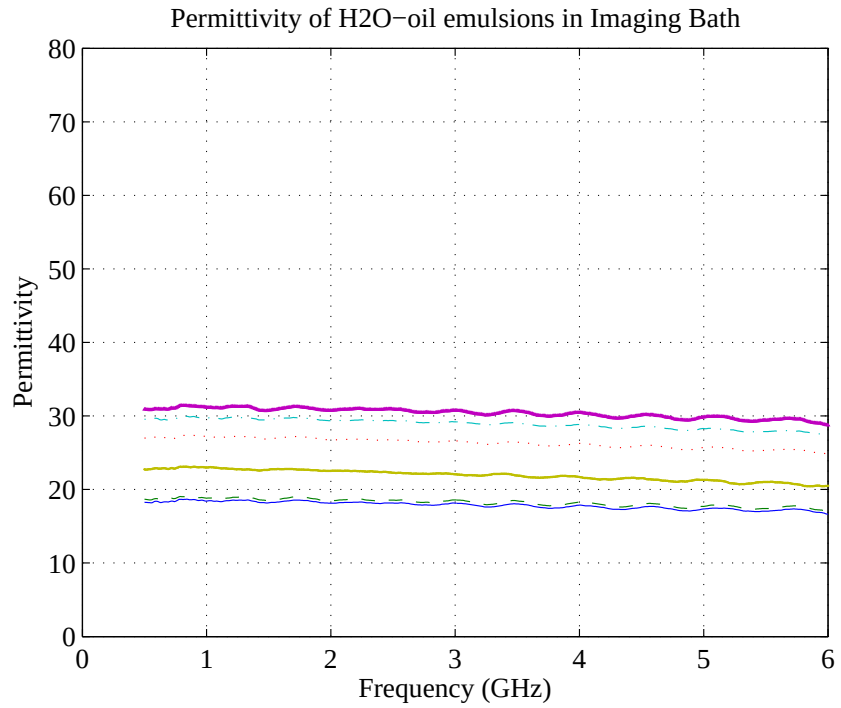

Figure 5.22: Relative permittivity of water-oil emulsions in imaging tank

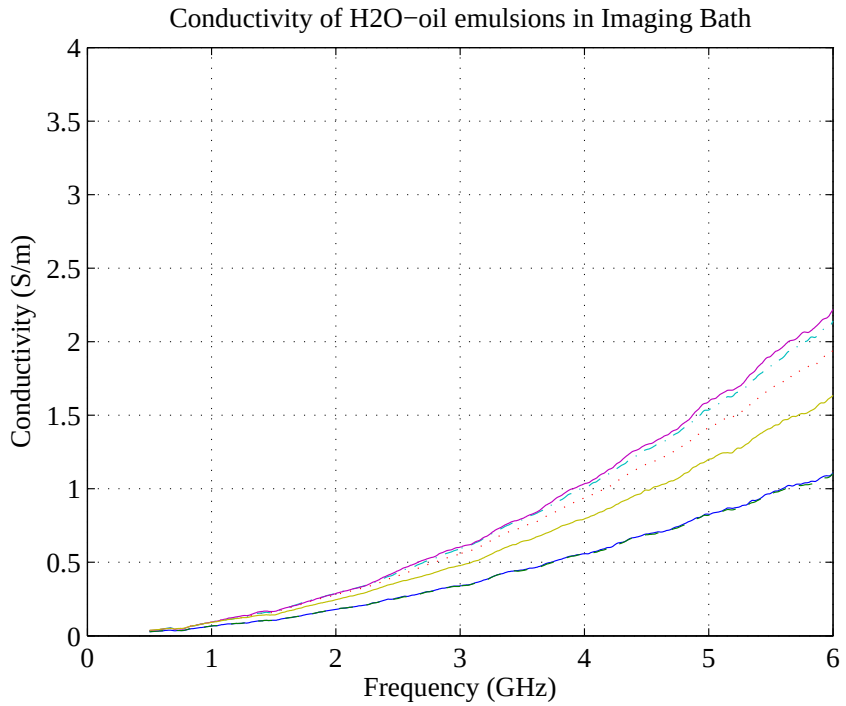

Figure 5.23: Conductivity [S/m] of water-oil emulsions in imaging tank

CHAPTER 6

Microwave Imaging

Integrated Hardware Experimental Test

6.1 Experiment Overview

The specific goal of this part of the dissertation is the proof-of-concept for a high-fidelity measurement of the scattered waves due to a transmitted ultra-wideband microwave signal, traveling through a 'microwave tissue-mimicking' environment including a matching medium and tumor-like phantoms. The critical components of the experimental system - antennas and coupling medium - have been described above. The task now is to integrate the system components with a vector network analyzer, and perform measurements of the scattered waves with various scattering objects. Photographs of measurement system is shown in Figures 6.1, 6.2, 6.3, and 6.4. As described in Chapter 4, four antenna designs were fabricated and tested:

- minor radius = 10mm, taper factor = 16mm
- minor radius = 10mm, taper factor = 26mm
- minor radius = 8mm, taper factor = 16mm
- minor radius = 8mm, taper factor = 26mm

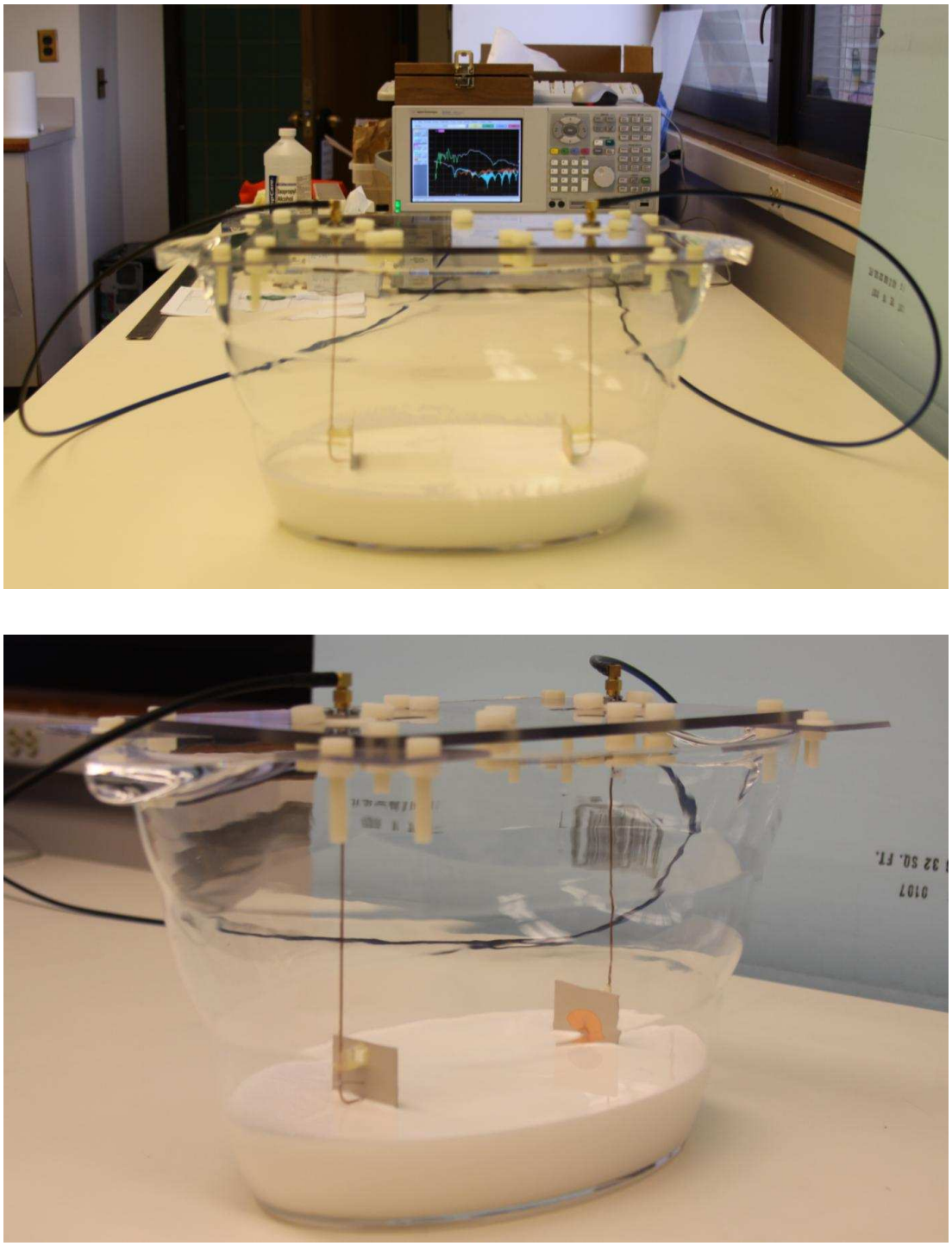

Figure 6.1: Microwave imaging system experimental set-up: imaging tank

For each design option, a pair of the antennas was tested: one antenna designated as the transmitter, the other as the receiver. The propagated signals, S21, were measured with the vector network analyzer, Agilent N 5230A PNA-L. In all cases, S21 transmission parameter was first measured with no scattering objects present between the antennas. This constitutes the incident field. Once the incident field was established, S21 transmission was measured again with various scattering objects placed between the antennas. The scattering objects include a 1cm and 6mm conducting spheres, and several dielectric spheres targets (tgt1, tgt2, tgt3, tgt4) summarized here:

1. tgt1 (3.5cm dia) = 42ml H2O and 7.3g gelatin, 6:1 ratio
2. tgt2 (2.5cm dia)= 50ml H2O and 5g gelatin, 10:1 ratio
3. tgt3 (2.5cm dia)= 50ml H2O and 8.2g gelatin, 6:1 ratio
4. tgt4 (2cm dia)= 50ml H2O and 8.2g gelatin, 6:1 ratio

The recipes for the dielectric spheres were derived empirically based on tissue-mimicking phantoms developed for ultrasound and magnetic resonance imaging [70] [71]. The tissue-mimicking phantoms described in these articles were designed with ultrasound properties that were not necessarily pertinent to microwave imaging - the acoustic properties to be specific. For microwave tissue-mimicking dielectric spheres, recipes were simplified to contain only water and gelatin. The measured permittivity and conductivity of these tumor-mimicking dielectric spheres are included in Figure 6.5 and 6.6. To note on these figures is the dielectric properties measurement repeatability. The last five sets of data shown is from one water/gelatin recipe, namely 50ml H2O and 8.2g gelatin. Various physical factors affect the measurement accuracy, including water content on the surface of the dielectric sphere, possible air gaps in the sphere as Agilent Slim Form probe is inserted into the sphere, heterogeneity of the 'hand-made' gelatin spheres.

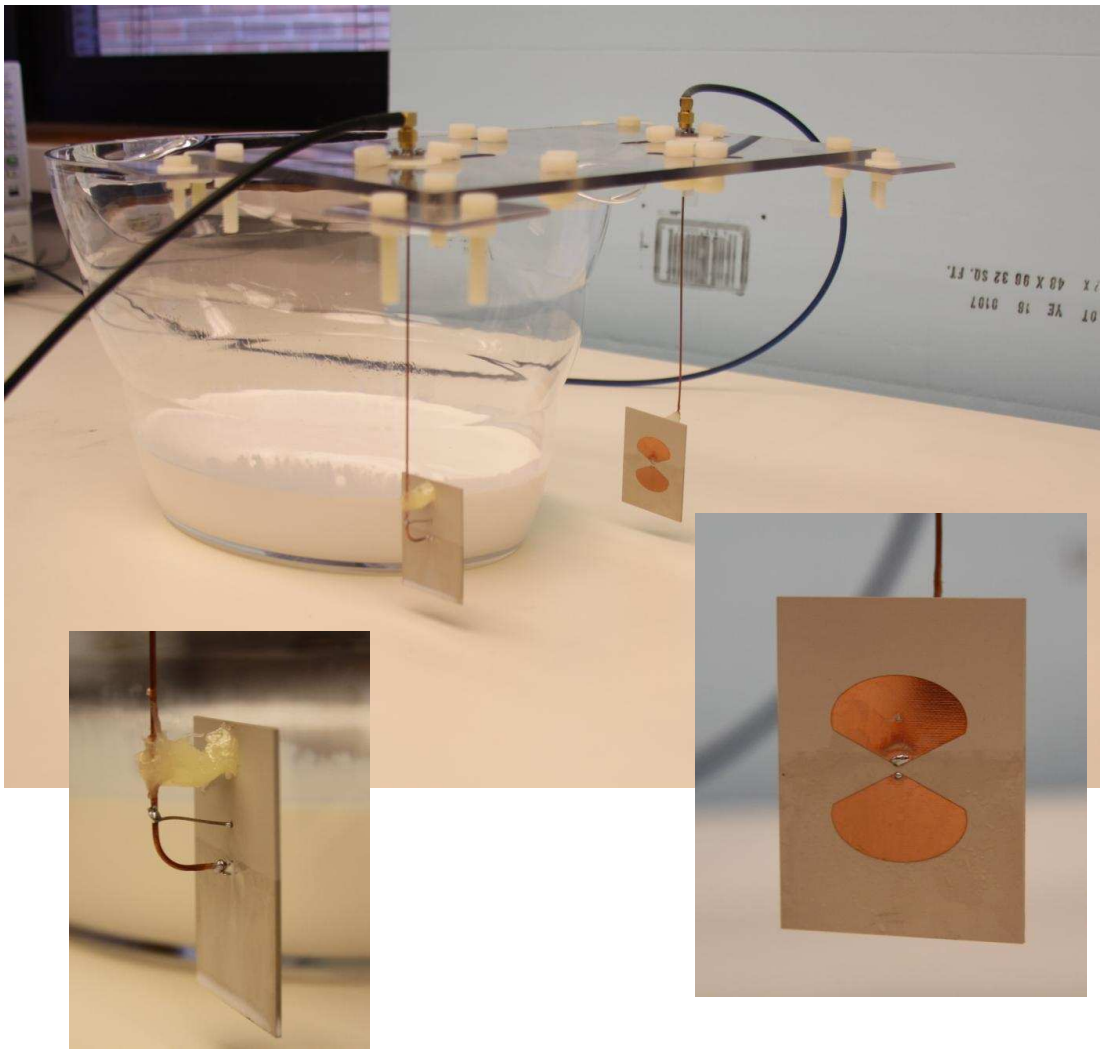

Figure 6.2: Microwave imaging system experiment set-up: imaging tank

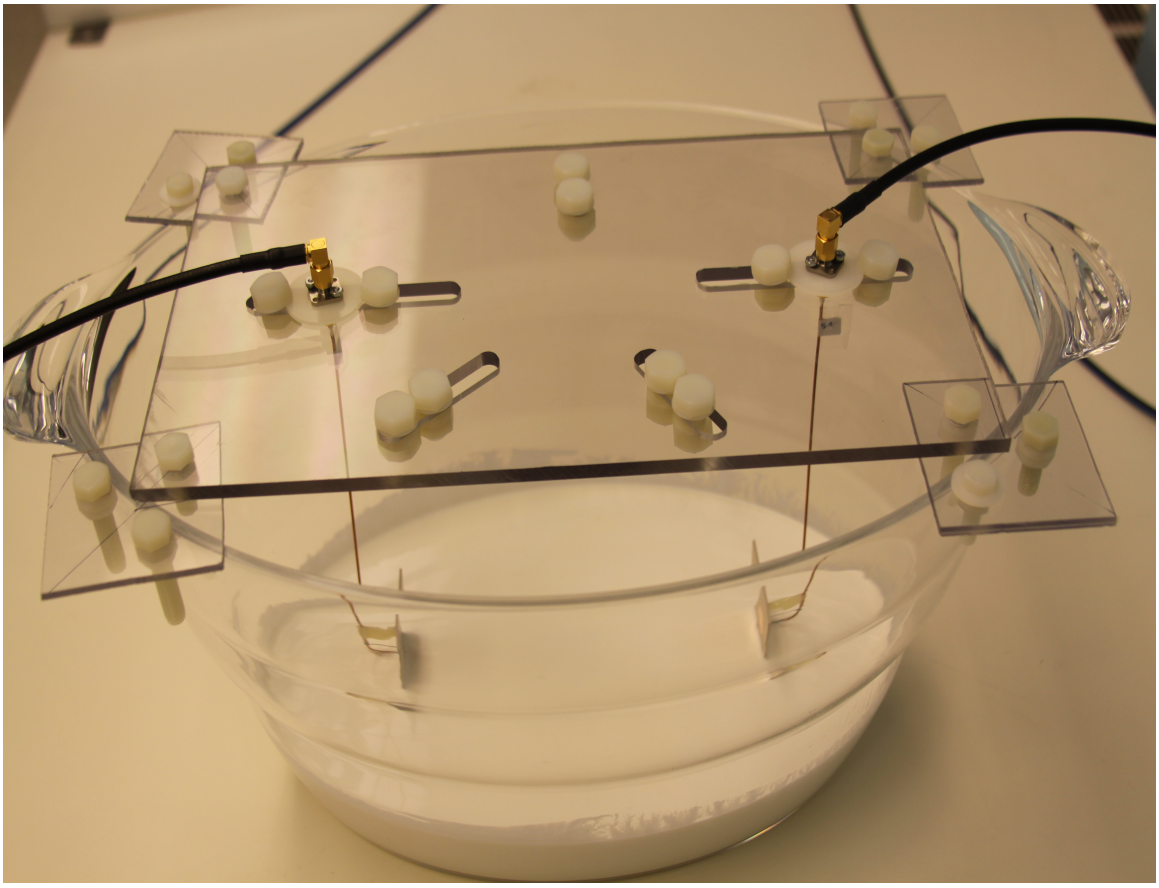

Figure 6.3: Microwave imaging system experiment set-up: imaging tank

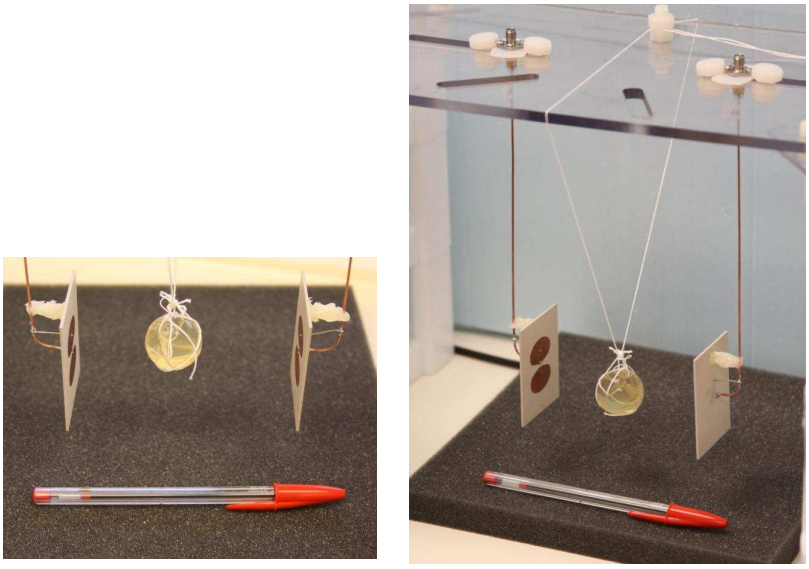

Figure 6.4: Microwave imaging system experiment set-up: a pair of antennas with a 2.5cm dielectric scattering target.

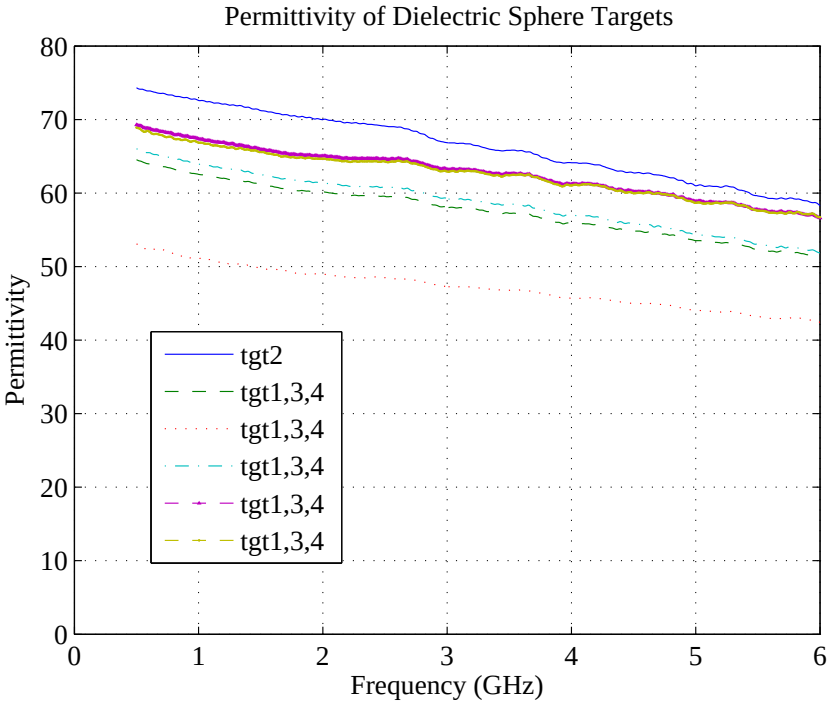

Figure 6.5: Permittivity of dielectric sphere scattering objects.

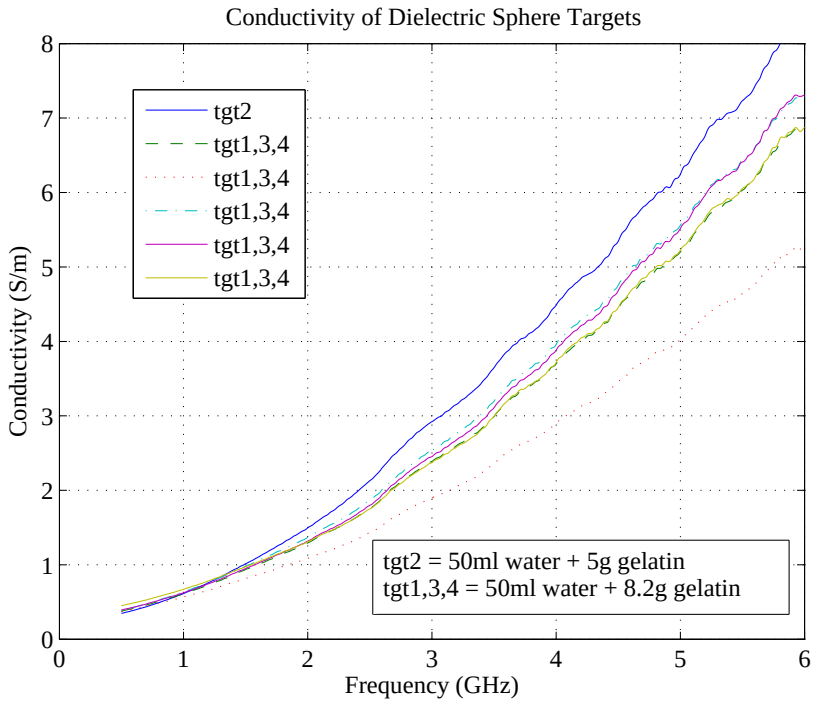

Figure 6.6: Conductivity of dielectric sphere scattering objects.

6.2 Microwave Imaging System Test Results

To preface the detailed discussion of individual system test cases, general observations are presented.

1. It was observed that little leakage current exists on the outer conductor of semi-rigid coaxial cable feed to the antennas. The balun was specifically integrated into the antenna design for this purpose. It was observed that behavior of antenna reflection loss is stable as load is applied to the semi-rigid coax cable.

2. As S21 transmission measurements were taken, the effects of the size of the imaging tank became apparent. In particular, oscillatory behavior at the low frequency end of the operating bandwidth was observed, which was attributed to scattering effect at the wall of the imaging tank shown in Figures 6.1, 6.2 and 6.3. The small tank size caused scattering at its wall due to permittivity mismatch between the coupling medium with $\varepsilon_{couplingmedium} \sim 22$ and free-space. When a larger tank was implemented, measured data show less scattering effect at the larger tank's wall - although not entirely absent.

3. Quantifying the effect of the coupling medium's conductive losses on phase linearity of the imaging system proved to be a challenge.

4. The measured reconstructed time-domain pulses agree with the simulated reconstructed pulses to varying degrees.

5. The selection of the time-domain input pulse has been arbitrary and can be changed as needed. This is demonstrated in the set of time-domain analysis plots. Each antenna design favors its own time-domain input pulse, one which would result in optimum reconstructed received pulse based on small variations in the antennas' frequency response. 'Optimum' is defined here as least dispersive behavior in the frequency content of the incident pulse. In future iterations of this microwave imaging

system, the addition of a waveform generator would allow for more rigorous design of the incident pulse.

6.2.1 Test Data from 'Small' Imaging Tank

Measured data presented in this subsection were taken when antennas were placed inside the imaging tank shown in Figures 6.1, 6.2, and 6.3. The top opening of this smaller tank has a major diameter = 39cm which narrows to 27cm at the bottom, and minor diameter = 27cm which narrows to 18cm at the bottom. Height of the tank is 22cm.

In testing the system with the first pair of antennas (minor radius = 10mm, tapering factor = 16mm), conducting spheres were used as scattering objects. For notation purpose, the conducting sphere scattering object will be referred to as perfect electric conductor (PEC) from here forward. The first set of data, Figures 6.7, 6.8, and 6.9, show measurements when the antennas were placed 10cm apart in a straight path facing each other, with and without a 1cm PEC scattering object present. Figures 6.8 and 6.9 show the time-domain reconstructed pulses - comparing measured versus simulated and measured data with and without presence of PEC, respectively. The photograph in Figure 6.4 illustrates the antennas' alignment but with a dielectric sphere shown instead. The scattered fields shown in Figure 6.7 shows the sensitivity of the imaging system to this small object, which is less than $\lambda\backslash 2$ at the highest frequency within the bandwidth.

The spacing between this pair of antennas (10mm radius, 16mm tapering factor) was then increased to 15cm which is similar to the spacing expected in a clinical system, keeping the 1cm PEC present as a scattering object. Scattered signal shown in Figure 6.10 is reduced between 10-20 dB compared to signal shown in Figure 6.7, as expected. Comparison of the measured and simulated reconstructed pulse, with no scattering objects present, is included in Figure 6.11. When the 1cm PEC is introduced, the reconstructed pulses with and without the presence of the PEC is shown in Figure 6.12

Keeping the antenna spacing at 15cm, a smaller PEC is placed between the antennas.

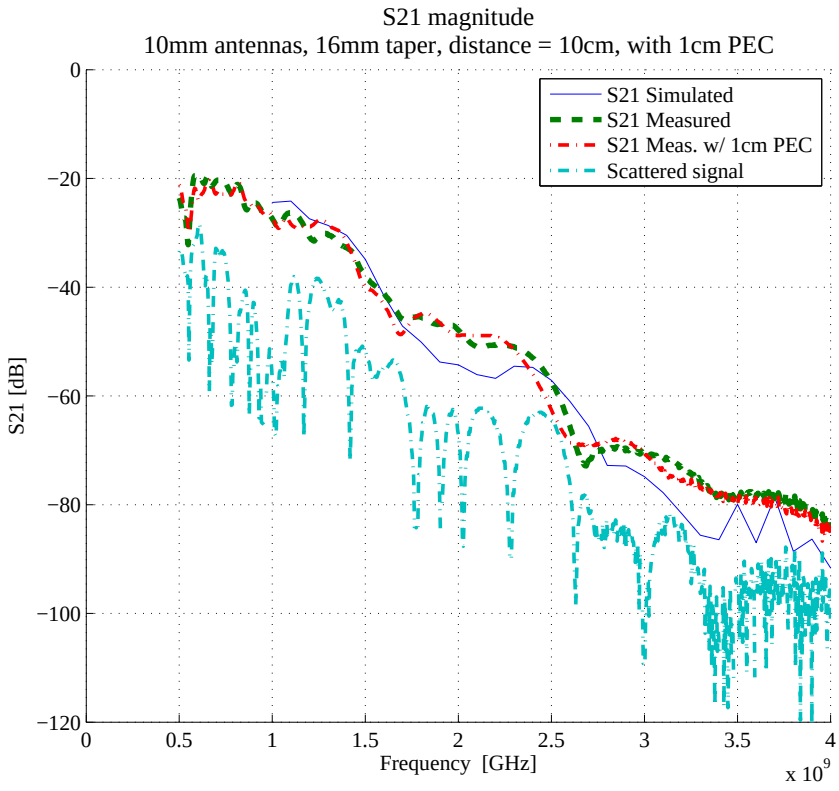

Figure 6.7: Measured vs. simulated propagated signal [S21]: radius = 10mm, taper = 16mm, antennas placed facing each other with a distance of 10cm, with a 1cm diameter PEC as scattering object

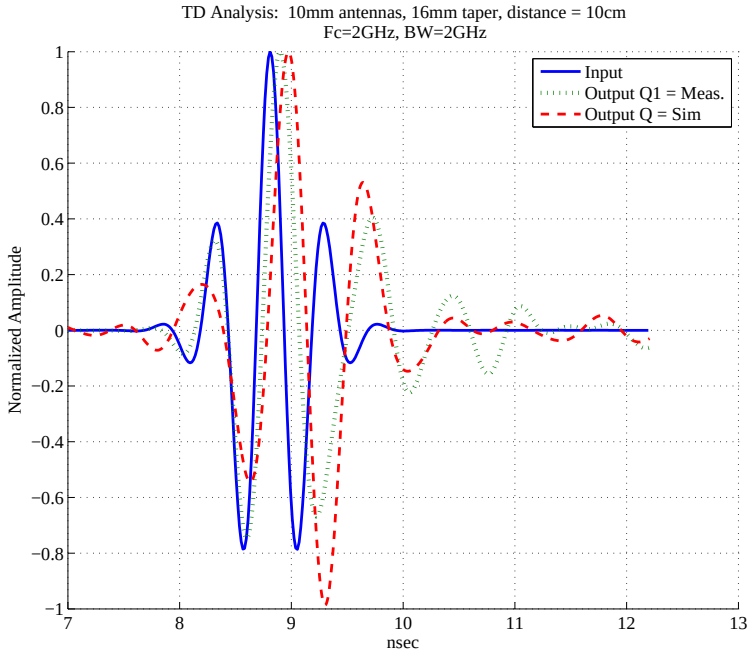

Figure 6.8: Measured vs. simulated wide-band pulse: radius = 10mm, taper = 16mm, antennas placed facing each other with a distance of 10cm, with no scattering objects in between, Gaussian pulse: BW = 2 GHz, Fc = 2 GHz.

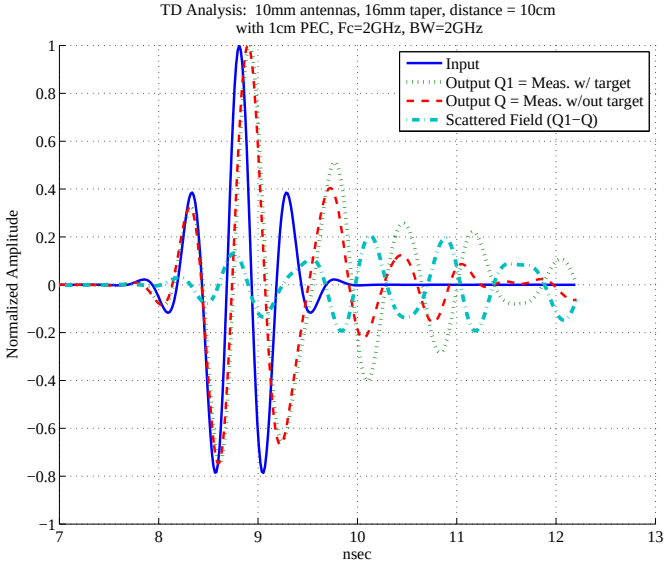

Figure 6.9: Measured wide-band pulse: radius = 10mm, taper = 16mm, antennas placed facing each other with a distance of 10cm, and a 1cm PEC sphere placed in between antennas, Gaussian pulse: Fc = 2 GHz, BW = 2 GHz.

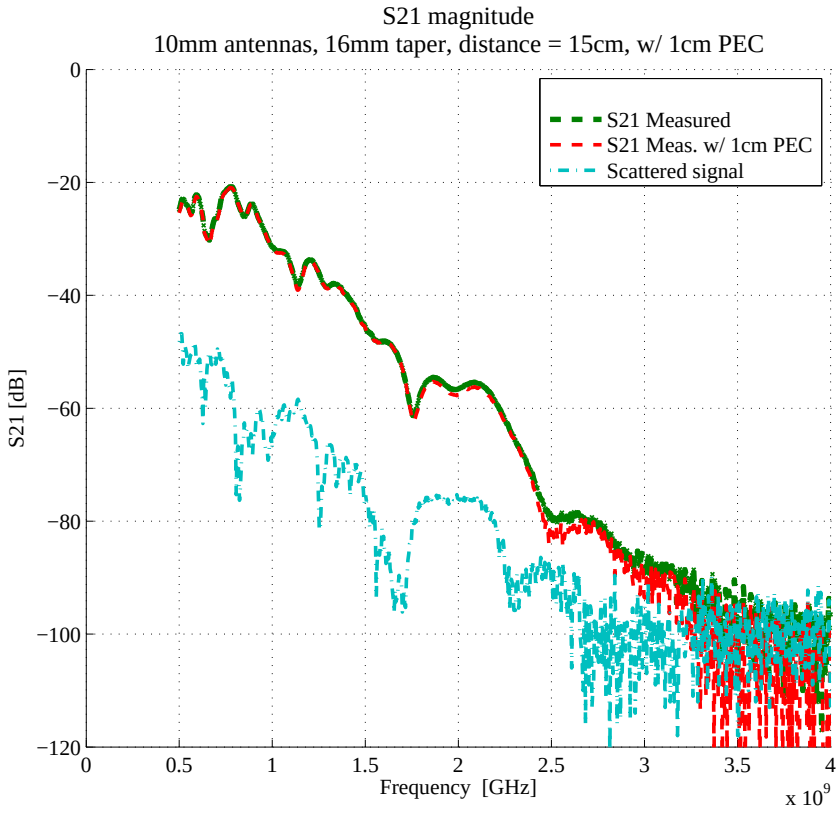

Figure 6.10: Measured propagated signal [S21]: radius = 10mm, taper = 16mm, antennas placed facing each other with a distance of 15cm, with a 1cm diameter PEC as scattering object.

The scattered fields shown in Figure 6.13 show that system can detect the presence of the 6mm PEC sphere, with even signal source output power of 0dBm. Comparison of the time-domain pulses, with and without the presence of the 6mm PEC sphere, are shown in Figures 6.11 and 6.14. The 6mm sphere represents $\sim \lambda\backslash 3$ target at the highest useful frequency of 4GHz.

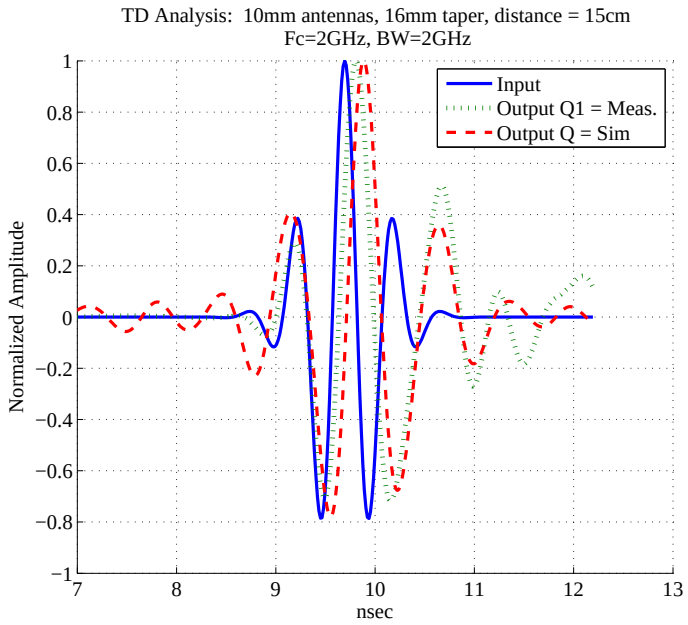

Figure 6.11: Measured vs. simulated wide-band pulse: radius = 10mm, taper = 16mm, antennas placed facing each other with a distance of 15cm, with no scattering objects in between, Gaussian pulse: Fc = 2 GHz, BW = 2 GHz.

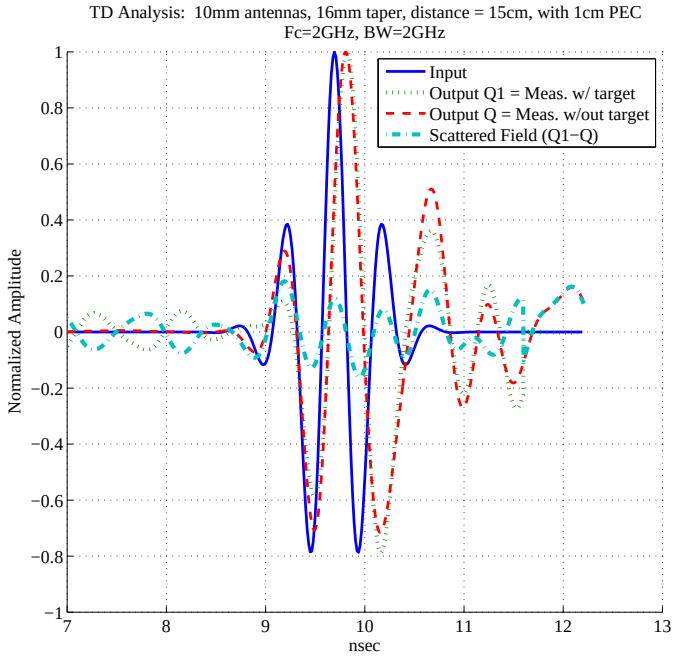

Figure 6.12: Measured wide-band pulse: radius = 10mm, taper = 16mm, antennas placed facing each other with a distance of 15cm, and a 1cm PEC sphere placed in between antennas, Gaussian pulse: Fc = 2 GHz, BW = 2 GHz.

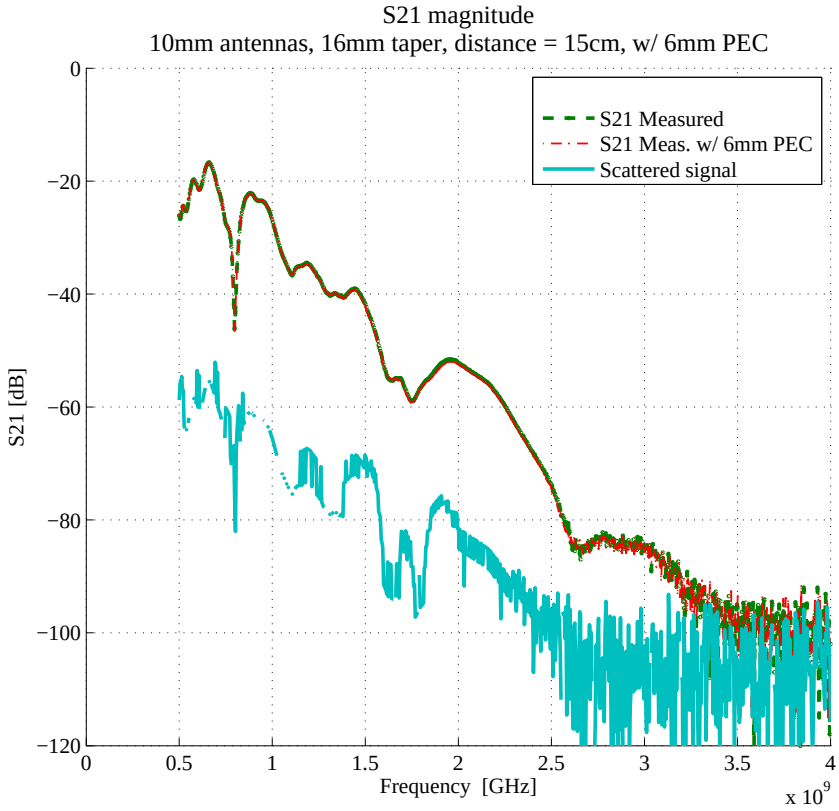

Figure 6.13: Measured propagated signal [S21]: radius = 10mm, taper = 16mm, antennas placed facing each other with a distance of 15cm, with a 6mm diameter PEC as scattering object.

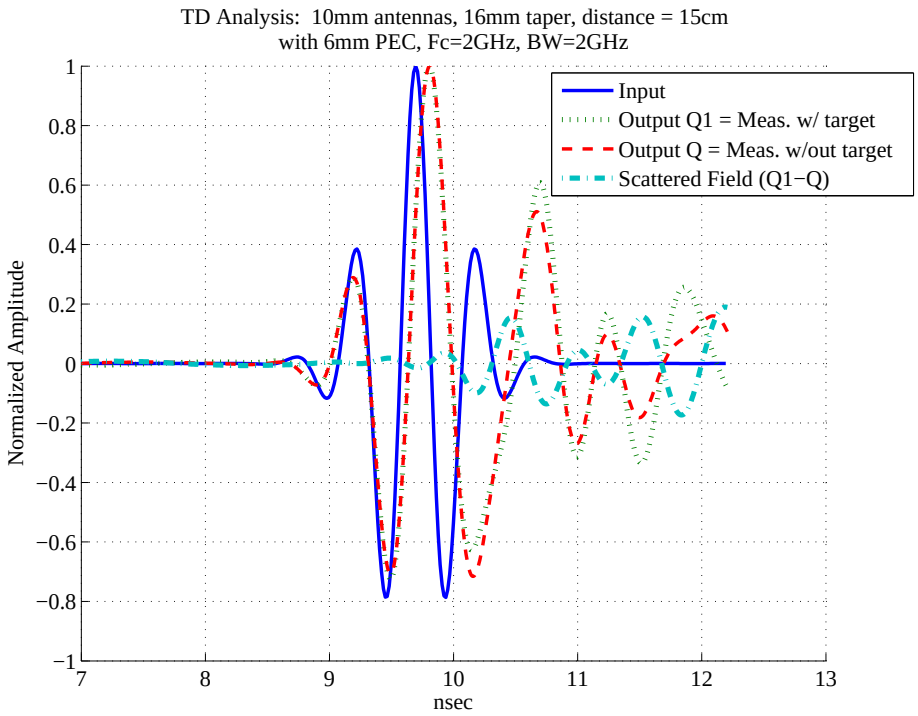

Figure 6.14: Measured wide-band pulse: radius = 10mm, taper = 16mm, antennas placed facing each other with a distance of 15cm, and a 6mm PEC sphere placed in between antennas, Gaussian pulse: Fc = 2 GHz, BW = 2 GHz.

Next are the measured S21 and the corresponding time-domain behavior of the propagated signal for antenna of minor radius = 10mm, with tapering factor = 26mm, shown in Figures 6.15 and 6.16. No measurement with scattering object was taken for this pair of antennas.

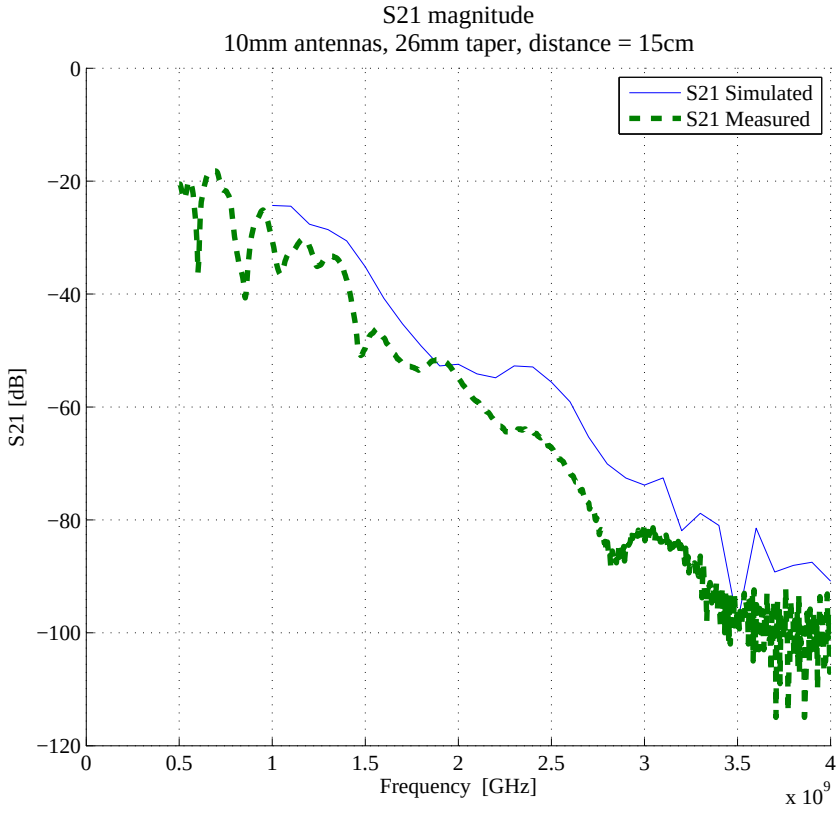

Figure 6.15: Measured propagated signal [S21]: radius = 10mm, taper = 26mm, antennas placed facing each other with a distance of 15cm

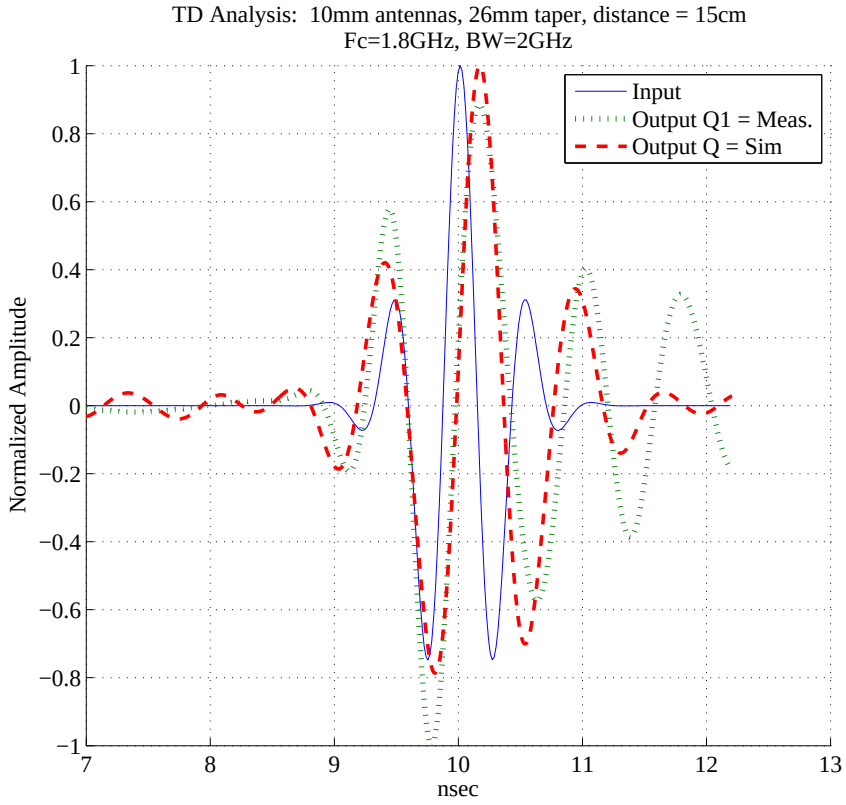

Figure 6.16: Measured vs. simulated wide-band pulse: radius = 10mm, taper = 26mm, antennas placed facing each other with a distance of 15cm, with no scattering objects in between, Gaussian pulse: Fc = 1.8 GHz, BW = 2 GHz.

The next few charts show the measured data with the smaller radii antennas, minor radius = 8mm, starting with tapering factor of 16mm. With these set of measurements, a 3.5cm dielectric sphere scattering object was introduced. The 3.5cm dielectric sphere is designated as 'tgt1;' its composition is listed above.

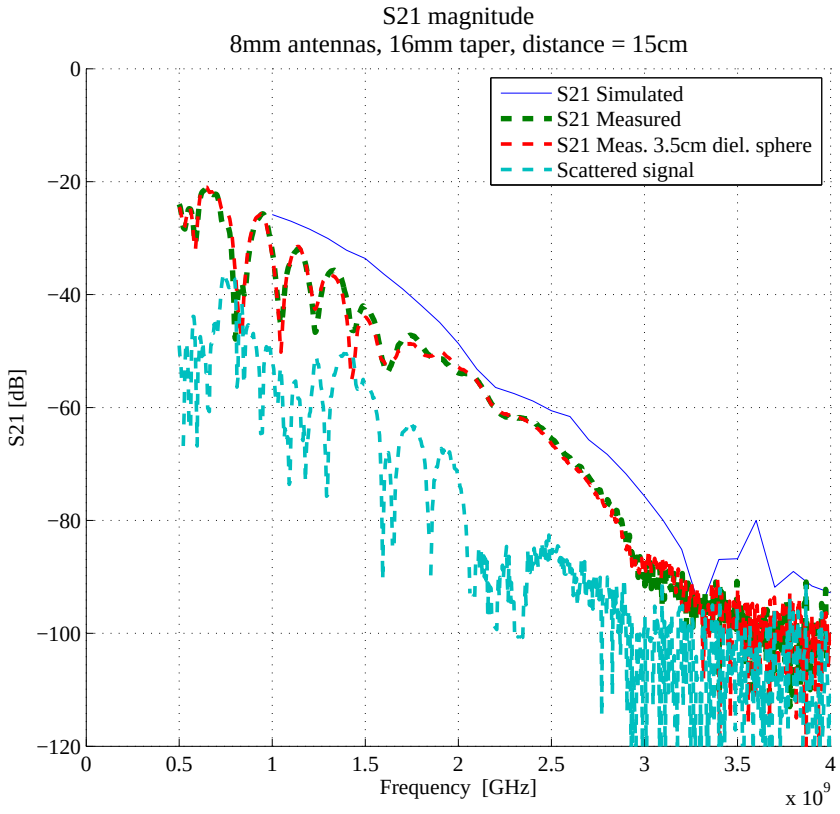

Figure 6.17: Measured propagated signal [S21]: radius = 8mm, taper = 16mm, antennas placed facing each other with a distance of 15cm, with a 3.5cm diameter sphere placed in between antennas, ε_{sphere} = 60. Simulated S21 does not include scattering objects.

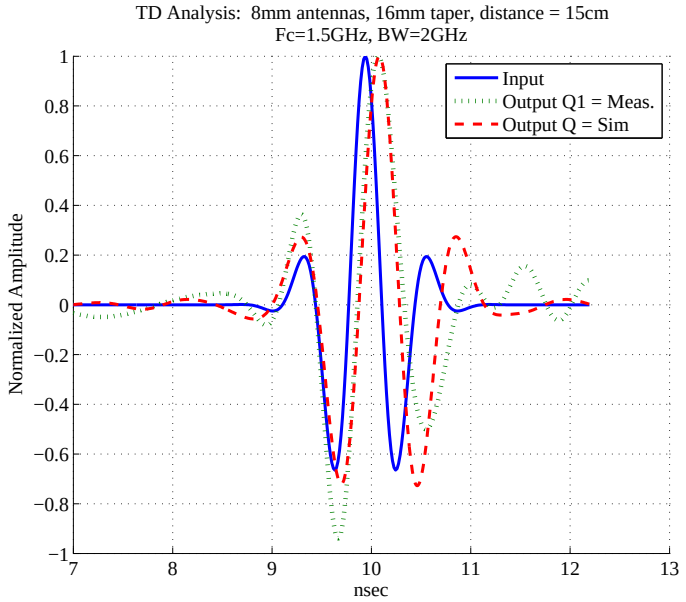

Figure 6.18: Measured vs. simulated wide-band pulse: radius = 8mm, taper = 16mm, antennas placed facing each other with a distance of 15cm, with no scattering objects in between, Gaussian pulse: Fc = 1.5 GHz, BW = 2 GHz.

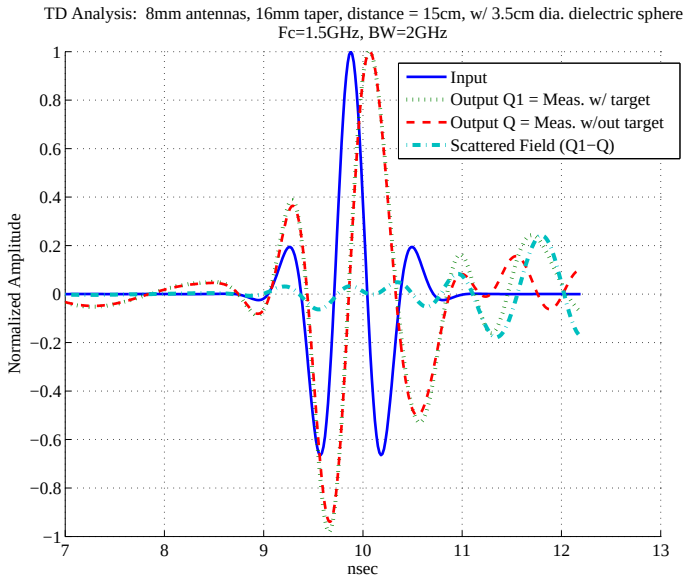

Figure 6.19: Measured wide-band pulse: radius = 8mm, taper = 16mm, antennas placed facing each other with a distance of 15cm, and a 3.5cm diameter sphere placed in between antennas, ε_{sphere} = 60, Gaussian pulse: Fc = 1.5 GHz, BW = 2 GHz.

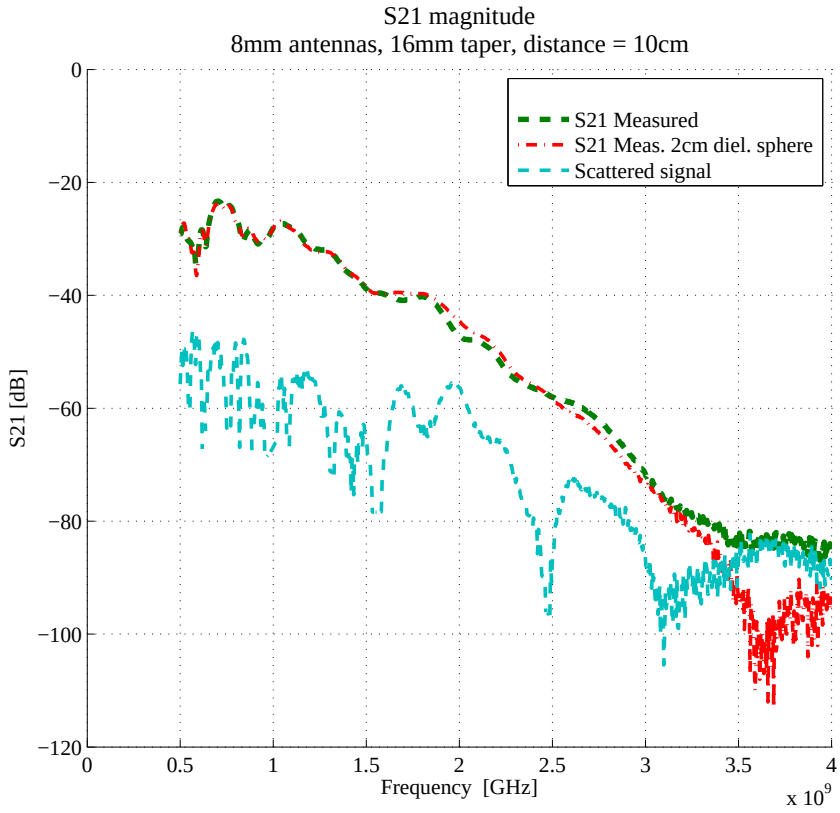

Figure 6.20: Measured vs. simulated propagated signal [S21]: radius = 8mm, taper = 16mm, antennas placed facing each other with a distance of 10cm, with a 2cm diameter sphere placed in between antennas, ε_{sphere} 60

To further test the system's dynamic range, a 2cm dielectric sphere was placed between a pair of 8mm-radius antennas of 16mm-tapering factor placed 10cm apart. Measured S21 is included in Figure 6.20. Figure 6.21 shows the simulated and measured time-domain pulse with no scattering object present, and Figure 6.22 shows the contrast between reconstructed pulses when no scattering sphere is present and with the 2cm dielectric present.

The last set of antennas are the 8mm radius with tapering factor of 26mm. Figure 6.23 shows the measured S21 with a 3.5cm diameter dielectric sphere placed between the antennas which were spaced 15cm apart. Important to note on this S21 chart is resonance behavior in the lower frequencies. As stated earlier, this is a result of the imaging tank's size being too small. Scattering off the wall of the imaging tank due to contrast between free-space and coupling medium's permittivities show up as these resonance peaks towards

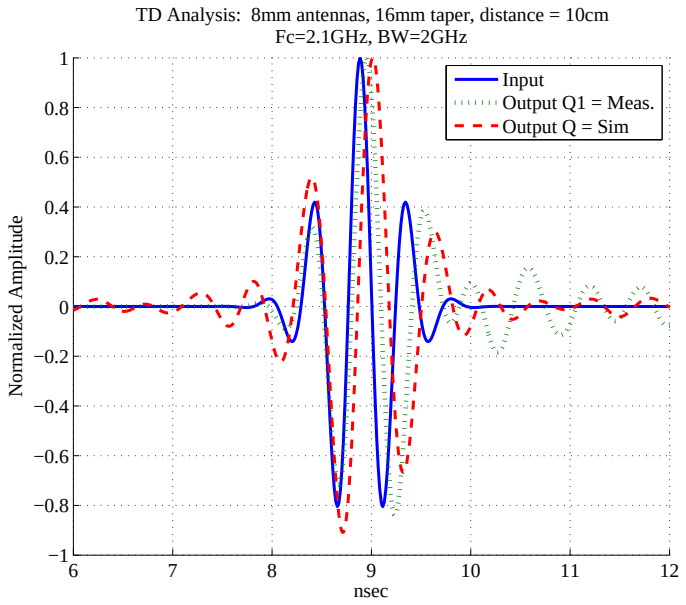

Figure 6.21: Measured vs. simulated wide-band pulse: radius = 8mm, taper = 16mm, antennas placed facing each other with a distance of 10cm, no scattering object present, Gaussian pulse: Fc = 2.1 GHz, BW = 2 GHz.

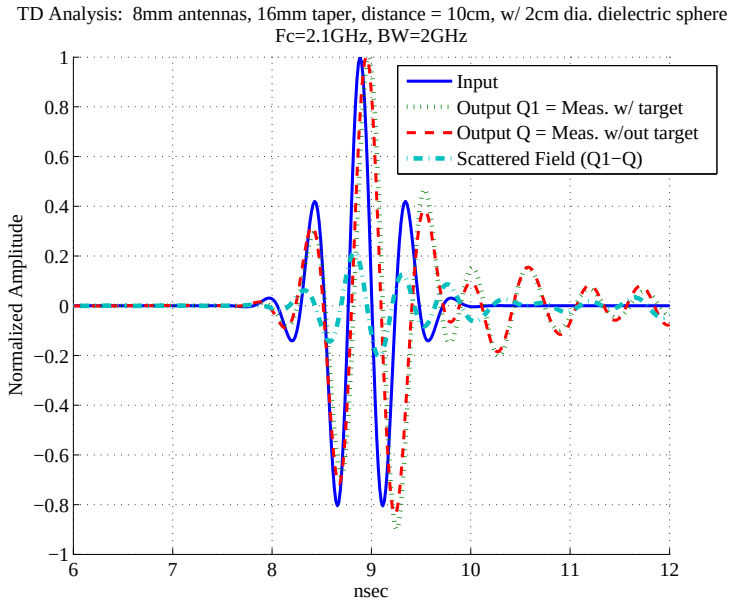

Figure 6.22: Measured wide-band pulse: radius = 8mm, taper = 16mm, antennas placed facing each other with a distance of 10cm, and a 2cm diameter sphere placed in between antennas, ε_{sphere} = 60, Gaussian pulse: Fc = 2.1 GHz, BW = 2 GHz.

the lower end of the operating frequencies. The net result is poor time-domain pulse reconstruction in late time, showing late-arriving multipath effects as can be seen in Figures 6.24 and 6.25.

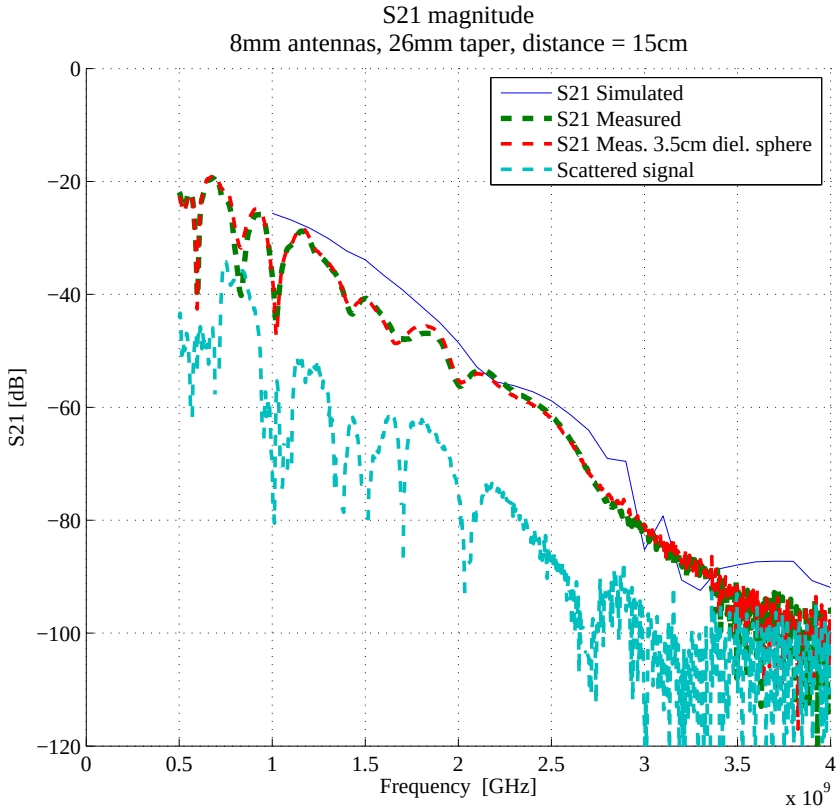

Figure 6.23: Measured propagated signal [S21]: radius = 8mm, taper = 26mm, antennas placed facing each other with a distance of 15cm, with a 3.5cm diameter sphere placed in between antennas, ε_{sphere} = 60. Simulated S21 does not include scattering objects.

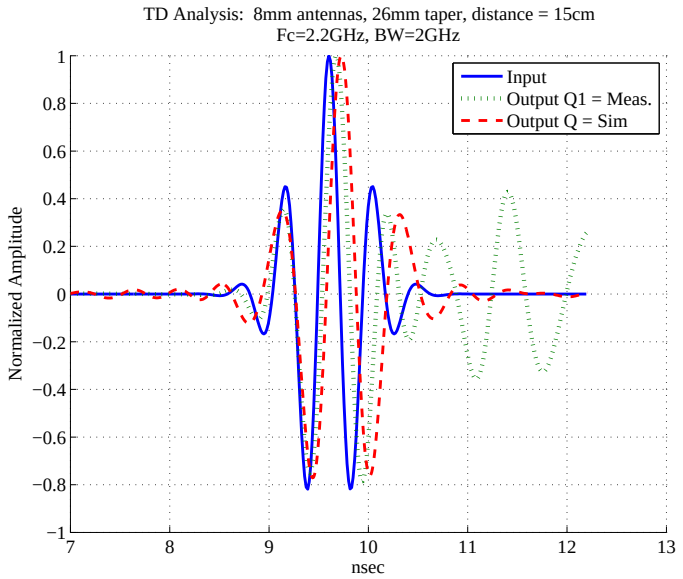

Figure 6.24: Measured vs. simulated wide-band pulse: radius = 8mm, taper = 26mm, antennas placed facing each other with a distance of 15cm, with no scattering objects in between, Gaussian pulse: Fc = 2.2 GHz, BW = 2 GHz.

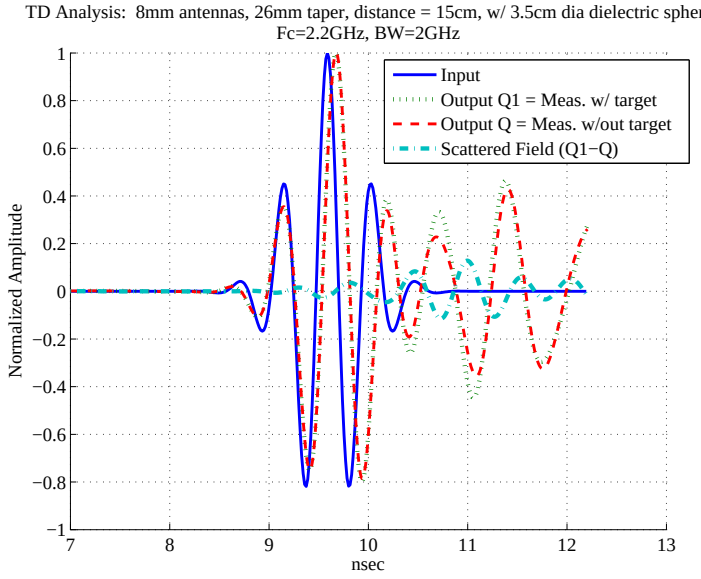

Figure 6.25: Measured wide-band pulse: radius = 8mm, taper = 26mm, antennas placed facing each other with a distance of 15cm, and a 3.5cm diameter sphere placed in between antennas, ε_{sphere} = 60, Gaussian pulse: Fc = 2.2 GHz, BW = 2 GHz.

At this point, all four antenna designs have been tested. In examining Figures 6.11, 6.16, 6.18, and 6.24, it is observed that the antenna design having minor radius of 8mm and tapering factor of 26mm seems to show the least dispersive behavior. Simulation results showed that tapering factor of 16mm would be less dispersive than 26mm tapering factor, but measured results showed otherwise. This measured result of the antenna behavior in the coupling medium showed agreement with the measured behavior of antennas in free-space - specifically, adding tapering factor improves phase linearity. In the case of the 8mm antenna with 26mm tapering factor, its measured pulse spreading of 14% is barely within the maximum 16% pulse spreading allowed for image reconstruction.

Summary of the measured and simulated pulse spreading of the four antenna designs:

- radius=10mm, taper=16mm
  - Simulated: 54 %
  - Measured: 54 %
- radius=10mm, taper=26mm
  - Simulated: 36 %
  - Measured: 36 %
- radius=8mm, taper=16mm
  - Simulated: 28 %
  - Measured: 28 %
- radius=8mm, taper=26mm
  - Simulated: 40 %
  - Measured: 14 %

Figure 6.26: Microwave imaging system experiment set-up: 'large' imaging tank

6.2.2 Test Data from 'Large' Imaging Tank

In attempt to remove the scattering effects at the walls of the smaller imaging tank, a larger, glass round imaging tank (diameter = 45cm) was used, Figure 6.26. As observed in the measured S21 data (Figures 6.28, 6.29, 6.30, and 6.31), scattering effects are reduced - though not entirely eliminated. Some resonance behavior can still be seen.

Data shown in this section also include measurements of pairs of antennas oriented at various imaging angles with respect to each other, namely 180 degrees (straight line), 130 degrees, 90 degrees, and 45 degrees - illustrated in Figure 6.27. In all cases below, a 2.5cm dielectric sphere was used as the scattering object for the 10mm antennas with tapering factor of 16mm. For the time domain analysis, a 2GHz bandwidth pulse was used.

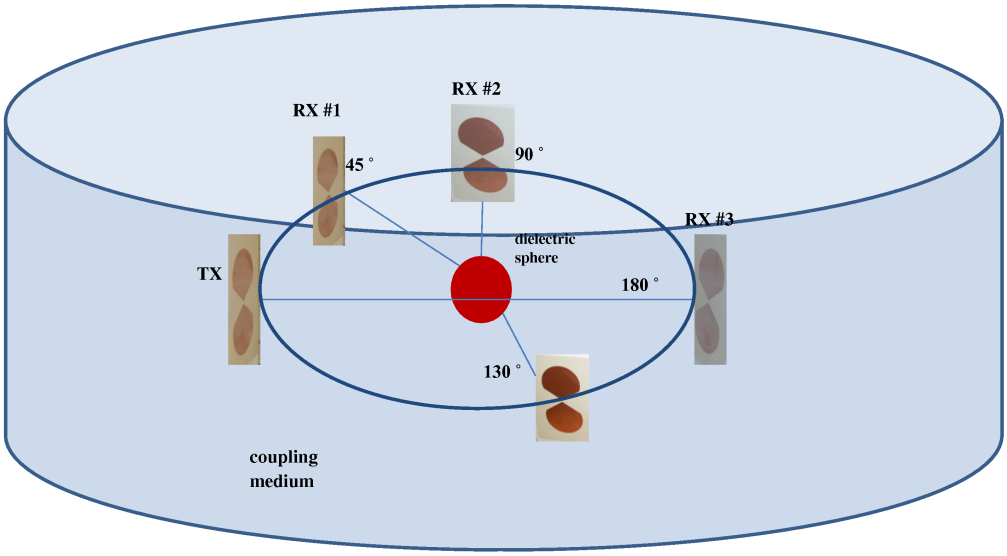

Figure 6.27: Antenna orientation: In each test case, a pair of antennas is used. The transmit antenna is paired with one of the receive antennas.

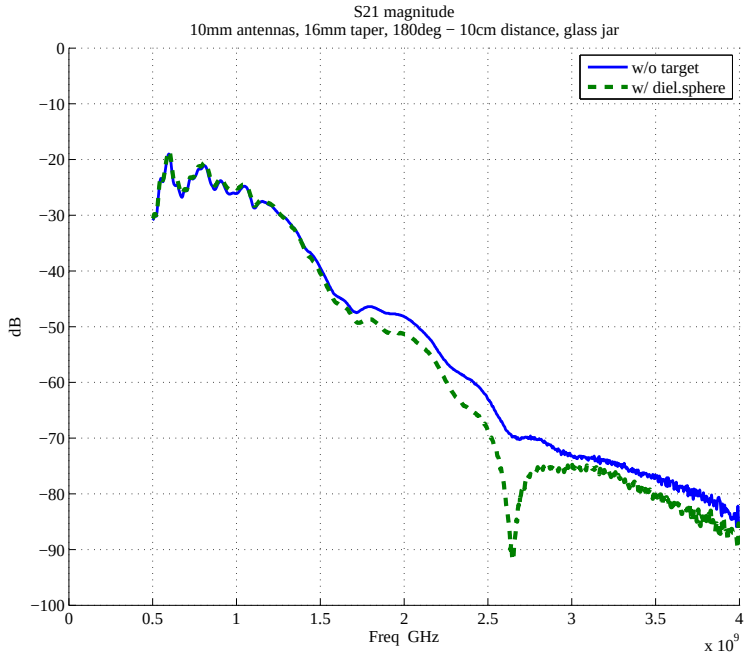

Figure 6.28: Measured propagated signal [S21]: radius = 10mm, taper = 16mm, antennas placed facing each other (180 degrees) with a distance of 10cm, with a 2.5cm diameter sphere placed in between antennas, $\varepsilon_{sphere} = 60$.

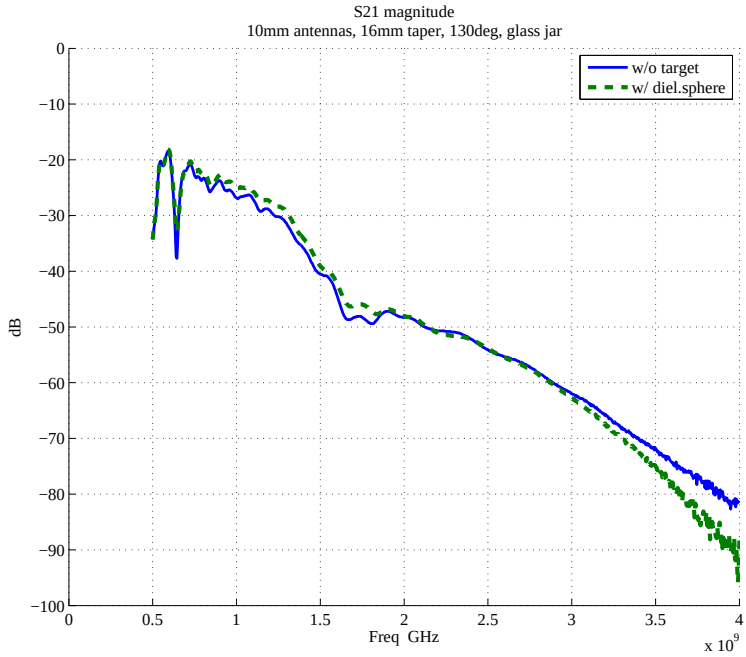

Figure 6.29: Measured propagated signal [S21]: radius = 10mm, taper = 16mm, antennas placed at 130 degree angle orientation with respect to each other, with a 2.5cm diameter sphere scattering object, $\varepsilon_{sphere} = 60$.

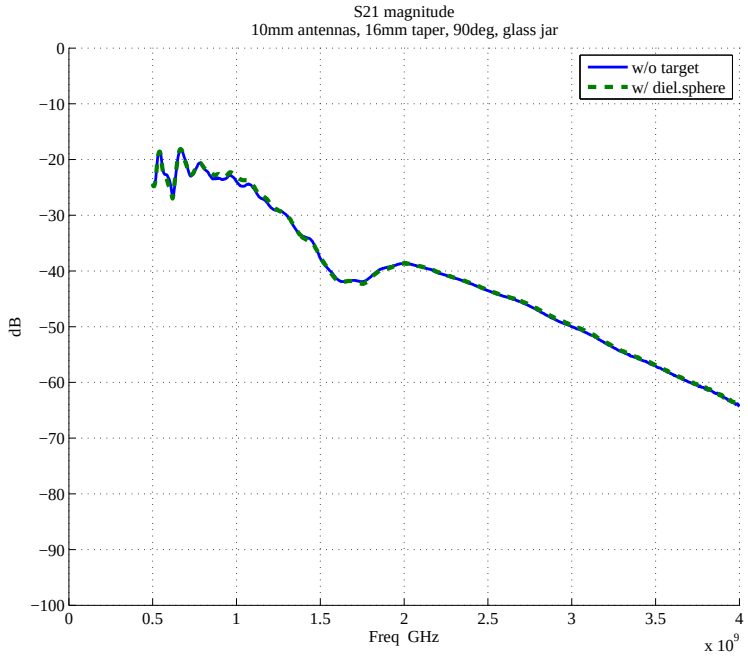

Figure 6.30: Measured propagated signal [S21]: radius = 10mm, taper = 16mm, antennas placed at 90 degree angle orientation with respect to each other, with a 2.5cm diameter sphere scattering object, $\varepsilon_{sphere} = 60$.

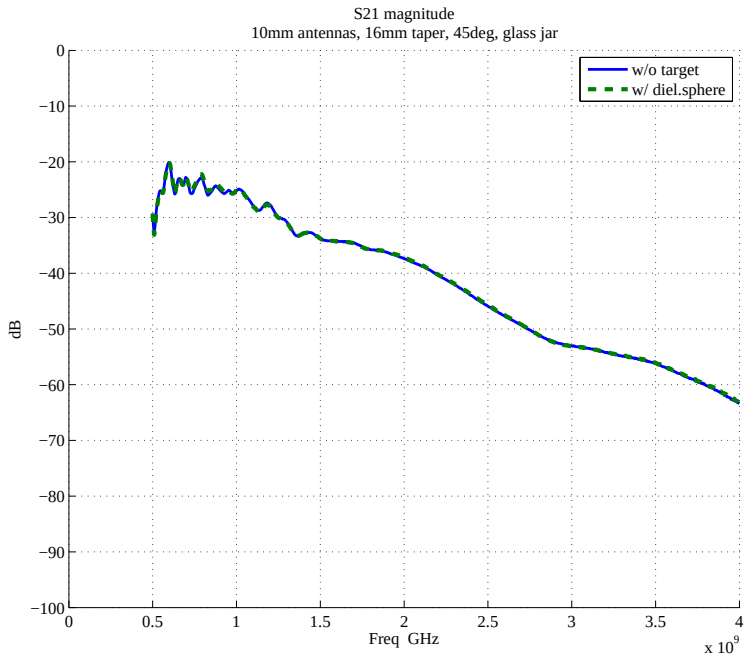

Figure 6.31: Measured propagated signal [S21]: radius = 10mm, taper = 16mm, antennas placed at 45 degree angle orientation with respect to each other, with a 2.5cm diameter sphere scattering object, $\varepsilon_{sphere} = 60$.

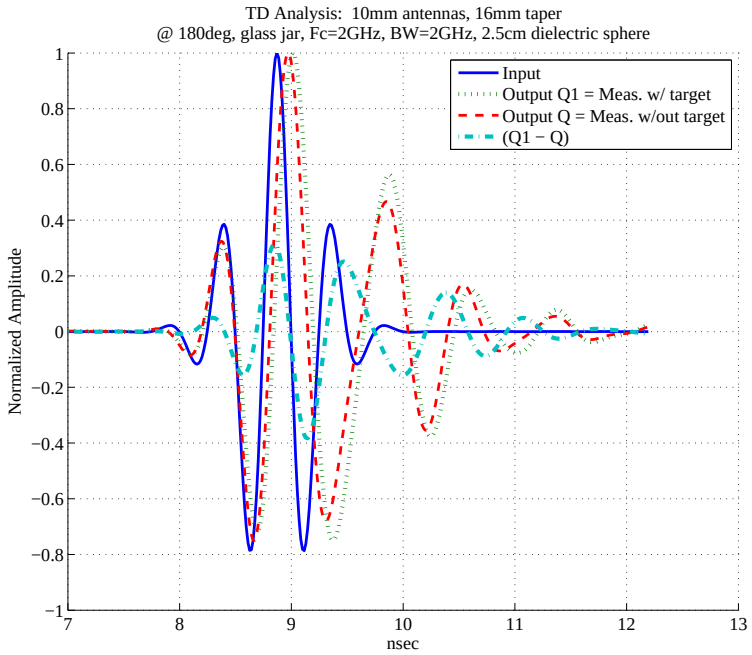

Figure 6.32: Measured wide-band pulse: radius = 10mm, taper = 16mm, antennas placed facing each other (180 degrees) with a distance of 10cm, with a 2.5cm diameter sphere placed in between antennas, $\varepsilon_{sphere} = 60$.

The time domain analysis plots (Figures 6.32, 6.33, 6.34, and 6.35) show that scattering object was more visible at the observation angles in the forward scatter direction - 180 degrees and 130 degrees.

Observations of measured data taken in the 'large' imaging tank:

- In the forward scattering direction of 180 degrees, the largest scattered signals were received (see Figure 6.32). This is to be expected as system sensitivity studies in Chapter 3 have shown.

- As receive antenna location is moved to 130 degrees and 90 degrees, with respect to the transmit antenna (see Figure 6.27), less scattered signals were measured. At the 45 degrees antennas orientation, hardly any scattered signal was detected (see Figure 6.36).

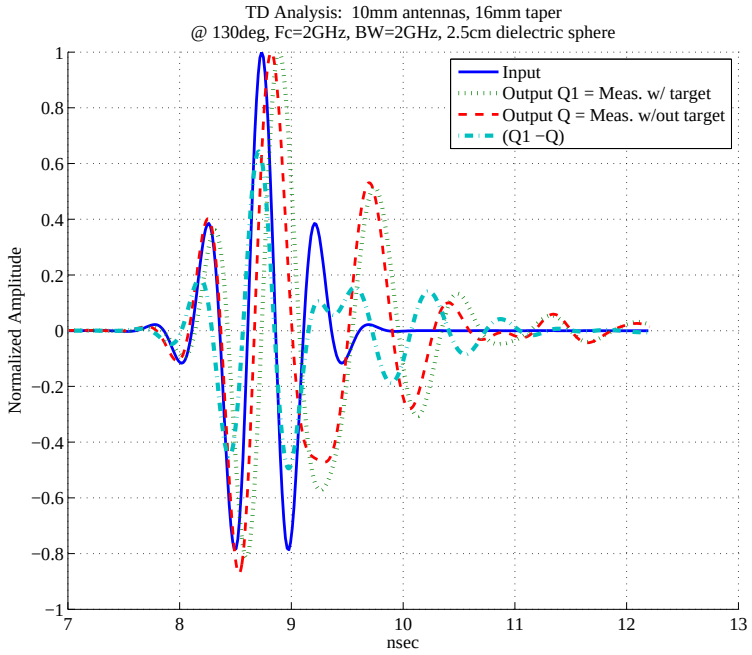

Figure 6.33: Measured wide-band pulse: radius = 10mm, taper = 16mm, antennas placed at 130 degree angle orientation with respect to each other, with a 2.5cm diameter sphere scattering object, $\varepsilon_{sphere} = 60$.

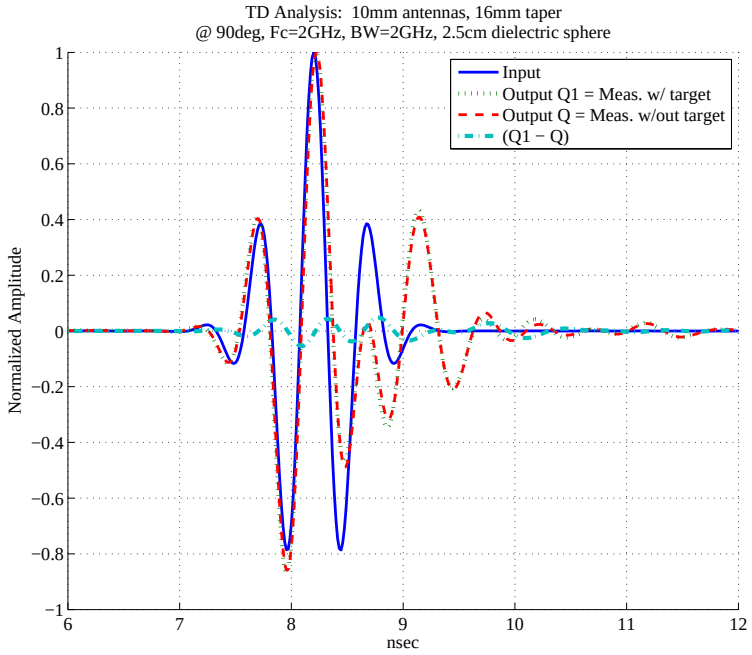

Figure 6.34: Measured wide-band pulse: radius = 10mm, taper = 16mm, antennas placed at 90 degree angle orientation with respect to each other, with a 2.5cm diameter sphere scattering object, $\varepsilon_{sphere} = 60$.

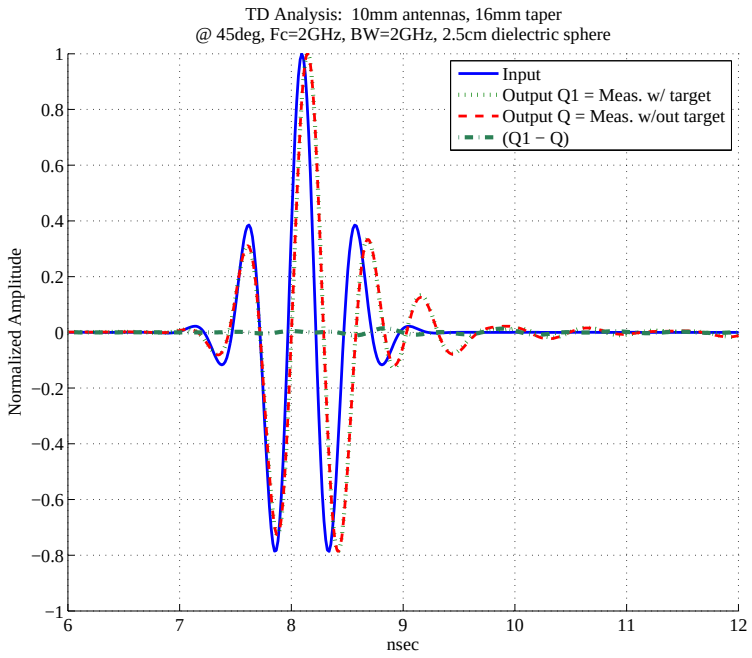

Figure 6.35: Measured wide-band pulse: radius = 10mm, taper = 16mm, antennas placed at 45 degree angle orientation with respect to each other, with a 2.5cm diameter sphere scattering object, $\varepsilon_{sphere} = 60$.

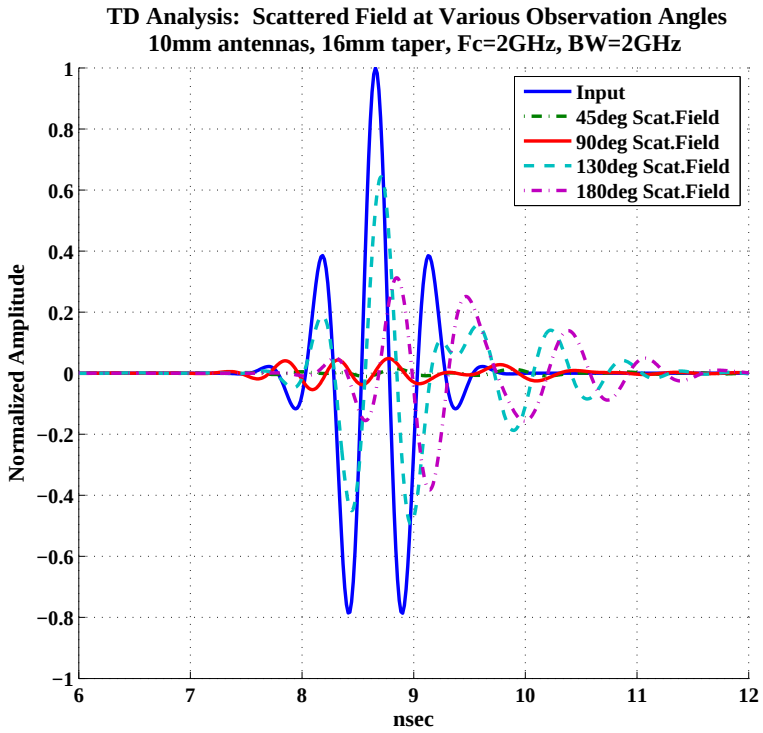

Figure 6.36: Measured wide-band pulses of a pair of antennas with radius = 10mm and taper = 16mm. One antenna is stationary, the other is swept at locations depicted in Figure 6.27 around a 2.5cm diameter sphere scattering object of ε_{sphere} = 60.

6.3 Discussion of Test Results

The experimental microwave imaging measurement system was constructed using small low-dispersion ultrawideband antennas, a biologically compatible coupling medium, conducting and dielectric targets, and a vector network analyzer. The measurement results were quite encouraging, and showed that this system is capable of detecting electrically small targets and in particular targets that are in the same size scale as required for early detection of breast cancer. To be more specific, the system was capable of detecting both conducting and dielectric (3:1 contrast with respect to coupling medium) spherical objects that were 6mm in diameter. Even though irregularly shaped objects were not tested, it is expected that scattering from such objects will be even more pronounced than spherical targets, and it might be possible to detect even smaller targets.

The pulse reconstructions, when the measurements were carried out without the object but in the coupling medium, showed that the antennas can indeed operate with very low dispersion across a wide frequency band, even though the high end of the bandwidth was found to be lower than the original design. Overall, this experiment confirmed the choice of the coupling medium, antenna design, and overall system design parameters. There were several issues identified in the course of the experiment:

- Homogeneity and stability of the coupling medium: The emulsion, which was described in Chapter 5, showed signs of oil and water separating during the 3-month experiment period. The separation extent was small - roughly 2 tablespoons per liter of emulsion - but it slightly impacted the electrical properties of the emulsion, especially the conductivity. The exact nature of this effect needs to be further studied. Furthermore, since the emulsion had to be made in small batches, after mixing the different batches some inhomogeneity is expected to have remained. Measurements shown in Figure 5.22 and 5.23 reveal such inhomogeneity.

- Size and shape of the imaging container: Two different tanks were used to carry

out the scattering measurements. The first and smaller container had an oval shape and tapered from top to bottom, which introduced asymmetries in the measurement scheme. The measurements such as those shown in Figure 6.23 show the effect of the small domain size, where mismatches between the walls and the air outside are quite evident. The second, larger, container was used to remove some of the issues related to the wall mismatches. The larger container did result in significantly less wall mismatch and multipath issues, but the problem was not totally resolved. It is proposed that appropriate absorbers be designed and used in the future implementations of the system.

- No actual images were formed (nor was it the intention of this thesis to do so); however, with the successful measurements carried out here, the road has been paved for the next step of using these measurements in the time-domain 3D inversion algorithm to show the super-resolution concept experimentally. This work will be carried out in the future in collaboration with other group members.

CHAPTER 7

Summary and Future Research Studies

7.1 Summary

The work presented in this dissertation contributes to the overarching goal of developing a more effective diagnostic and screening tool for detecting breast cancer in its earliest stages. The specific goal of this MWI system has been to take major steps towards achieving specificity of tumor masses, lower cost, patient comfort, and safe non-ionizing radiation. The combination of these factors, if achieved, provides for an attractive complementary tool for breast cancer detection, especially in remote or underprivileged areas. At the time of this writing, four technical publications are in preparation [4] [5] [6] [7].

7.2 Future Work

Perhaps the most critical study is the in-situ verification of tissue dielectric properties. All measurements done so far have been in-vitro [20] [3]. In progress at University of Michigan is the research effort to collect in-situ dielectric constant data during breast biopsies. Given the currently large number of breast biopsies - 70% of which do not result in surgery - and the fact that access to the patient is already provided while performing these biopsies, in-situ dielectric constant measurements are deemed more realistic to achieve.

Since such a study is also truly in-situ, the conclusions about dielectric properties of various masses are also expected to be much more credible. Research into the appropriate electrical probe and work on Institutional Review Board legalities are in progress.

Another major issue that needs to be addressed and resolved is the microwave system imaging noise. The noise present in the measured scattered fields almost always results in degradation of the resolution of the imaging system. Wideband systems are especially sensitive to system noise, since as the signal bandwidth increases, so does the noise present in the receiver. Noise could be due to the measurement system imperfections and the background, as well as to the effective unwanted multiple scattered waves from the walls and edges of various hardware components. These factors are exacerbated by the fact that, with the proposed MWI system, the required level of scattered signal levels to enable high-resolution detection and characterization of tumors is so low. The effects of system noise and multiple scattering would directly impact the fidelity of the inversion algorithm. Two potential near-future studies are: (1) surround the microwave imaging system with a physical perfectly matched boundary wall; and (2) enclose the microwave imaging system inside a conducting cavity equipped with absorbing material on the inside wall.

In the longer term, this MWI system needs to be developed as a stand-alone microwave transmit-receive system, much like a radar, instead of the current network analyzer-based implementation. By using high quality custom components for the active microwave imaging system, it will be possible to control the incident signal strength and to control the receiver sensitivity and noise floor. The knowledge gained through this dissertation can guide the design of such a future system.

Another area of future investigation is the study of polarization effects in the measurements. For the spherical targets considered in the measurements carried out in this thesis, such effects are not expected to be as important as they will be for non-symmetric objects and those objects with large aspect ratios, edges, and tips.

Finally, the ultimate objective of developing better versions of this system is using

its data to form high-resolution, high-fidelity, high-specificity images. A near-term study is needed to show that the data from this MWI setup can be used as input to the nonlinear super-resolution imaging algorithm, and to assess the effects of experimental imperfections on the quality of retrieved breast tissue maps. The measurement geometry investigated in the laboratory experiments consisted of a pair of receivers swept in a planar 'ring' configuration. In a future clinical system, multiple rings, either of the same radii or of successively smaller radii, must be considered in order to capture the scattered fields from all accessible sides of the breast tissue. This results in a more complete spatial representation of the scattered field and is known to result in better image reconstruction. The implementation of such a 3D measurement geometry is therefore another important follow-on research topic.

APPENDIX

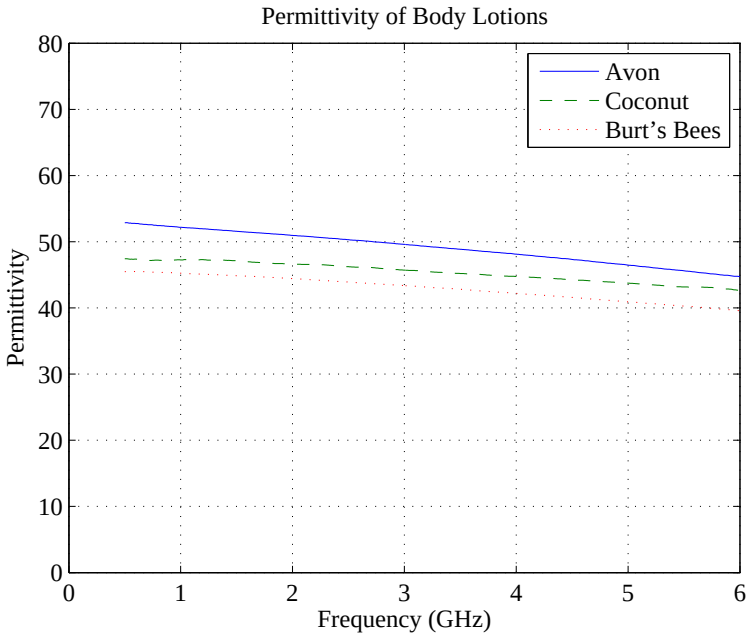

Figure 7.1: Relative permittivity of commercially available body lotions

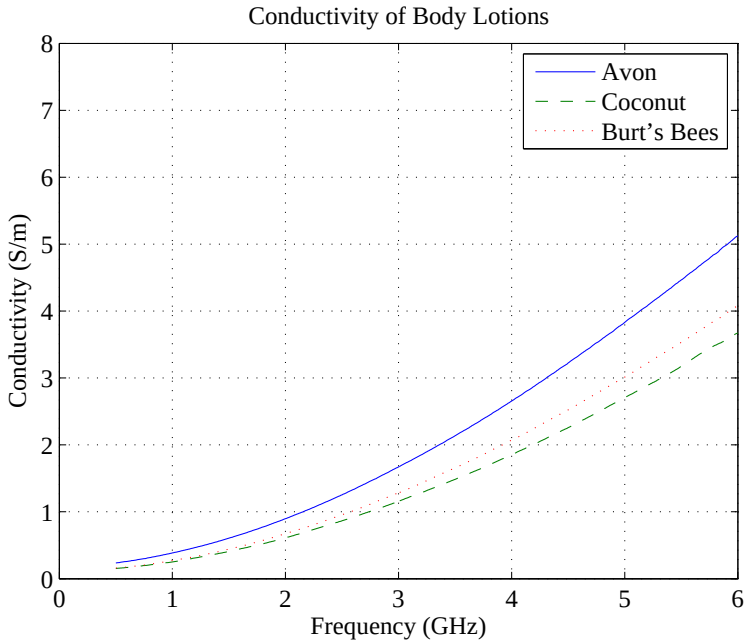

Figure 7.2: Conductivity [S/m] of commercially available body lotions

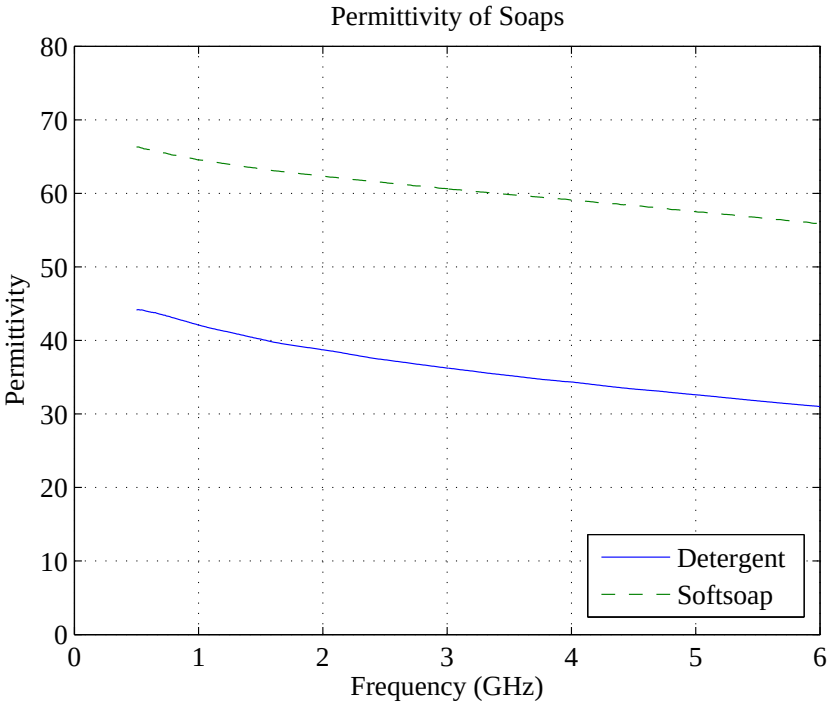

Figure 7.3: Relative permittivity of commercially available soaps

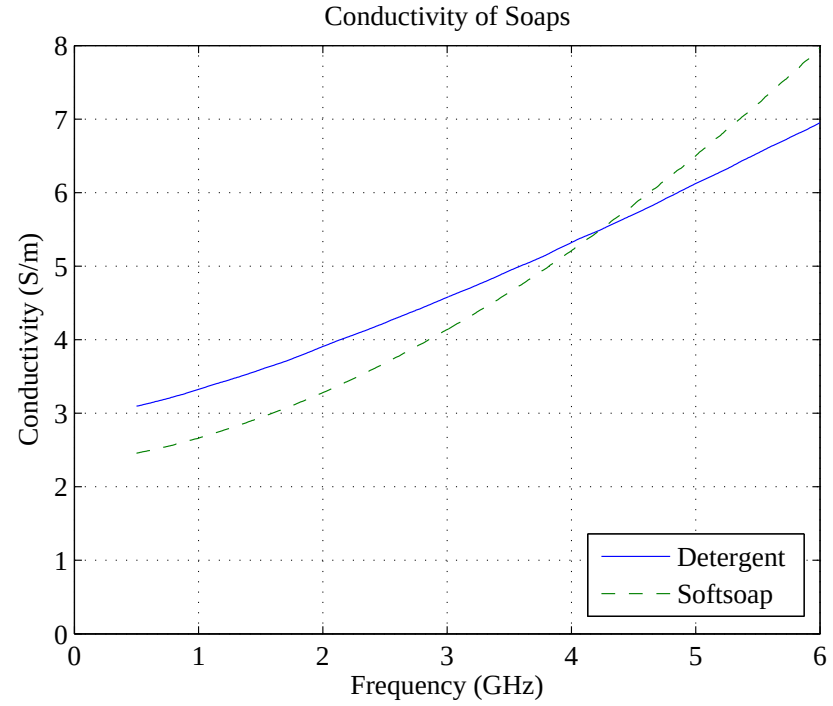

Figure 7.4: Conductivity [S/m] of commercially available soaps

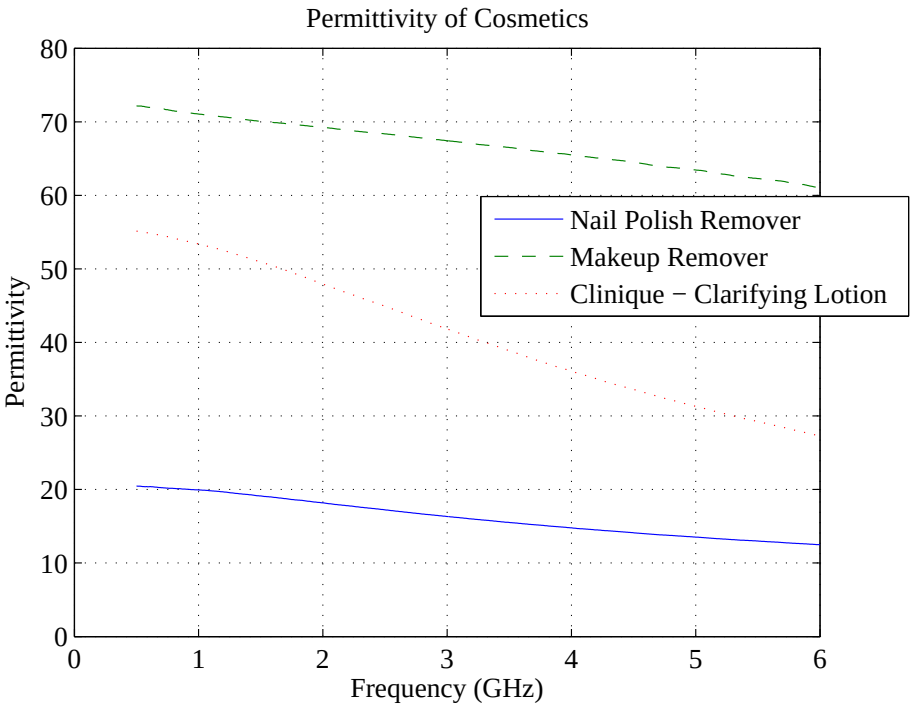

Figure 7.5: Relative permittivity of facial cosmetics

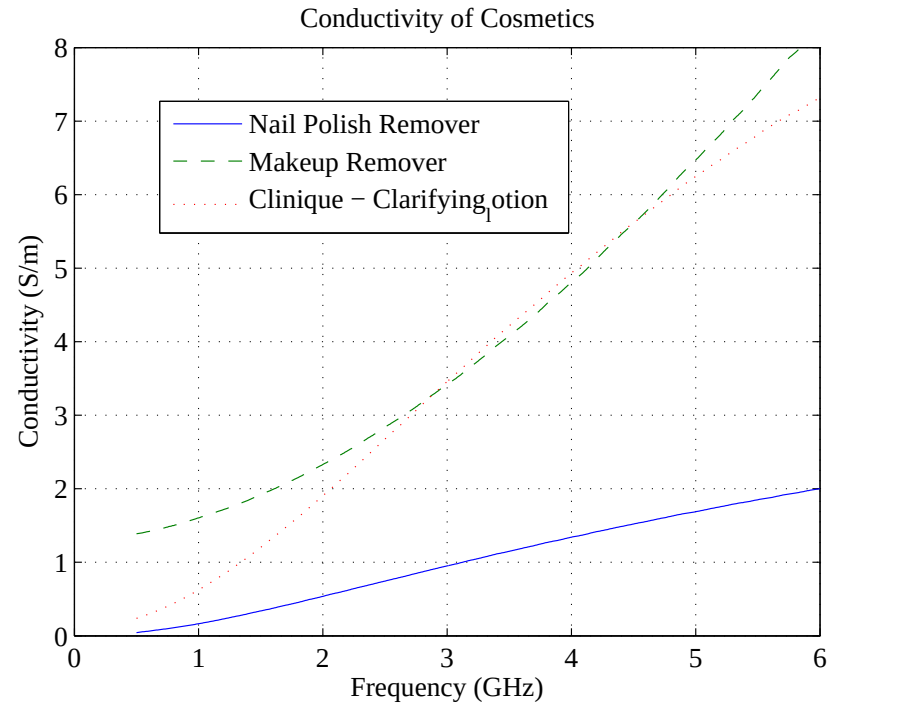

Figure 7.6: Conductivity [S/m] of facial cosmetics

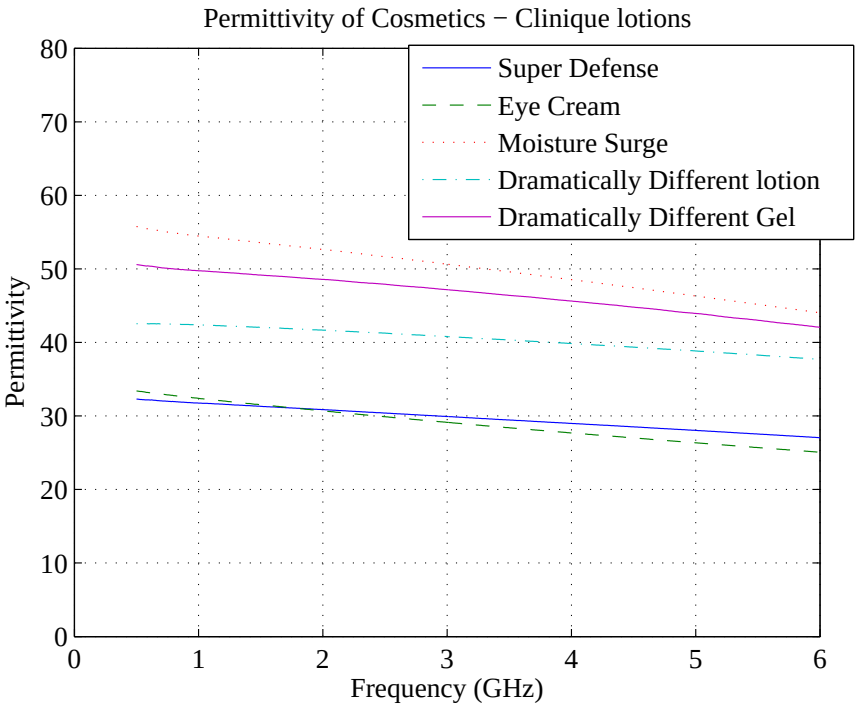

Figure 7.7: Relative permittivity of facial cosmetics

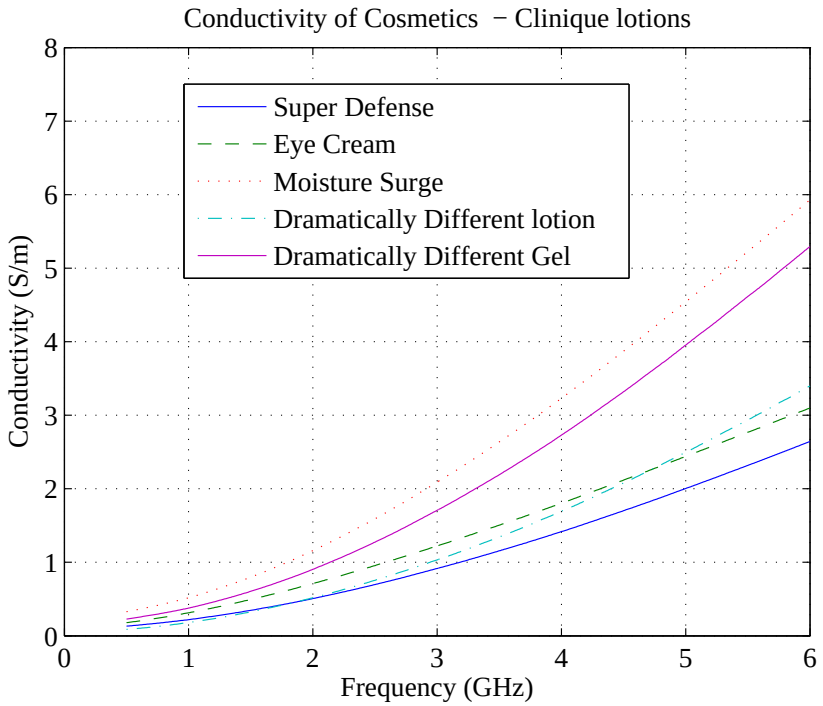

Figure 7.8: Conductivity [S/m] of facial cosmetics

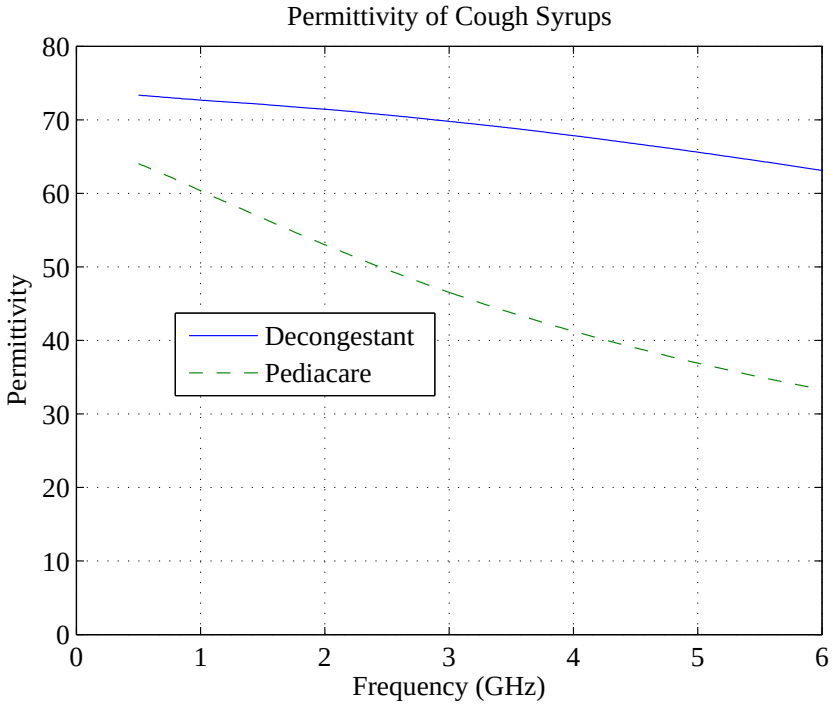

Figure 7.9: Relative permittivity of over-the-counter cold medicine

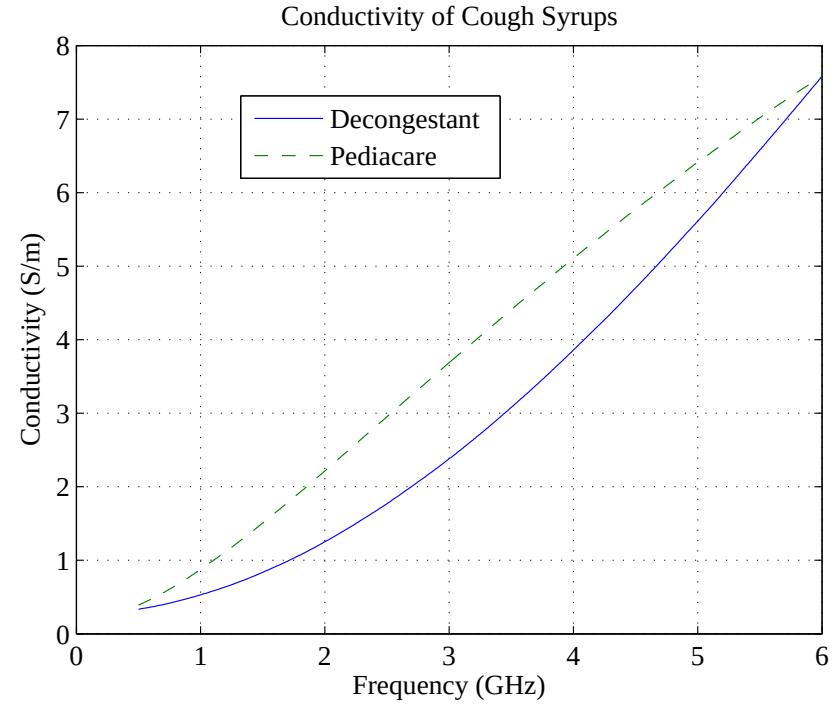

Figure 7.10: Conductivity [S/m] of over-the-counter cold medicine

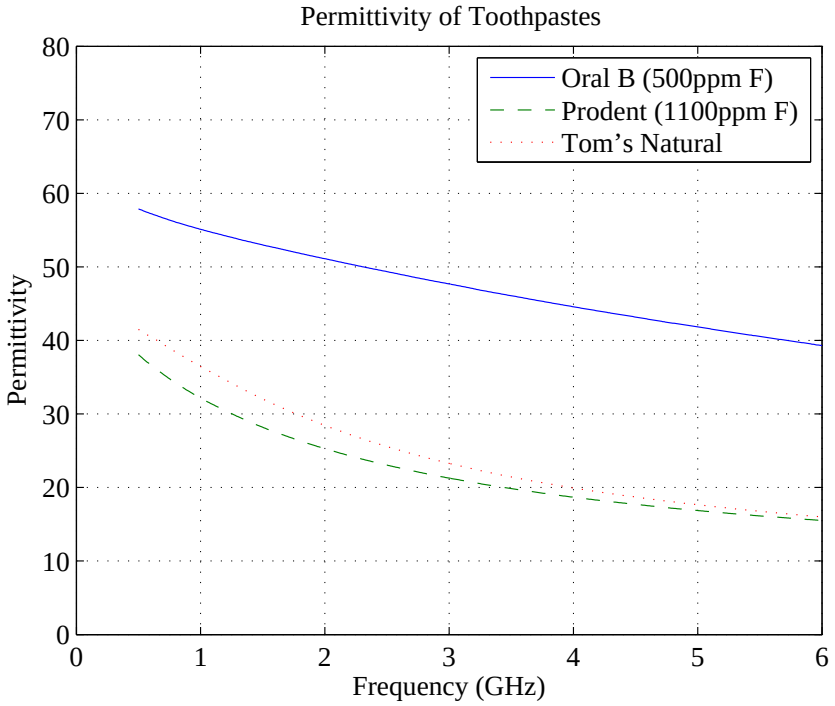

Figure 7.11: Relative permittivity of commercially available toothpaste

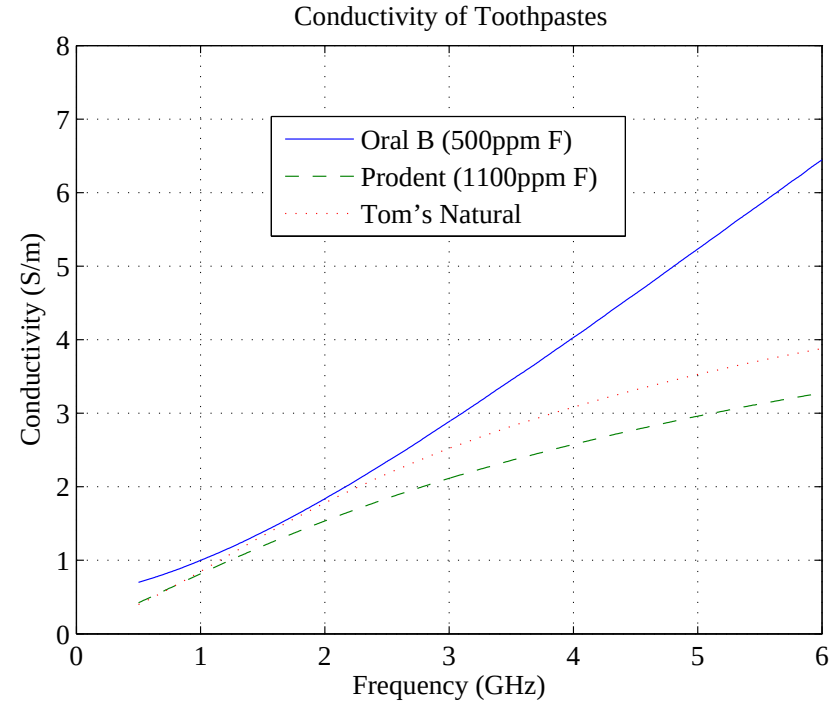

Figure 7.12: Conductivity [S/m] of commercially available toothpaste

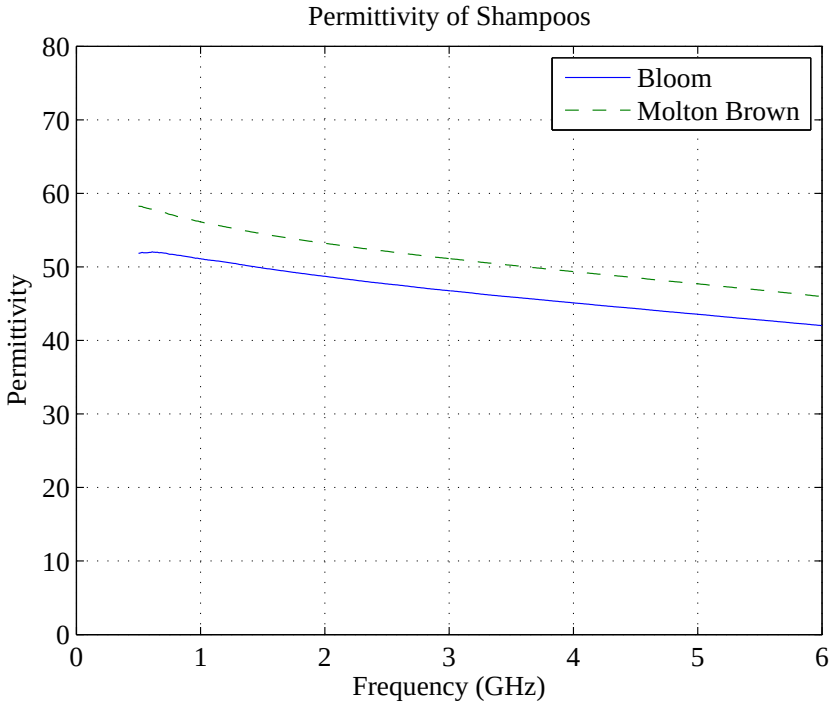

Figure 7.13: Relative permittivity of commercially available hair shampoo

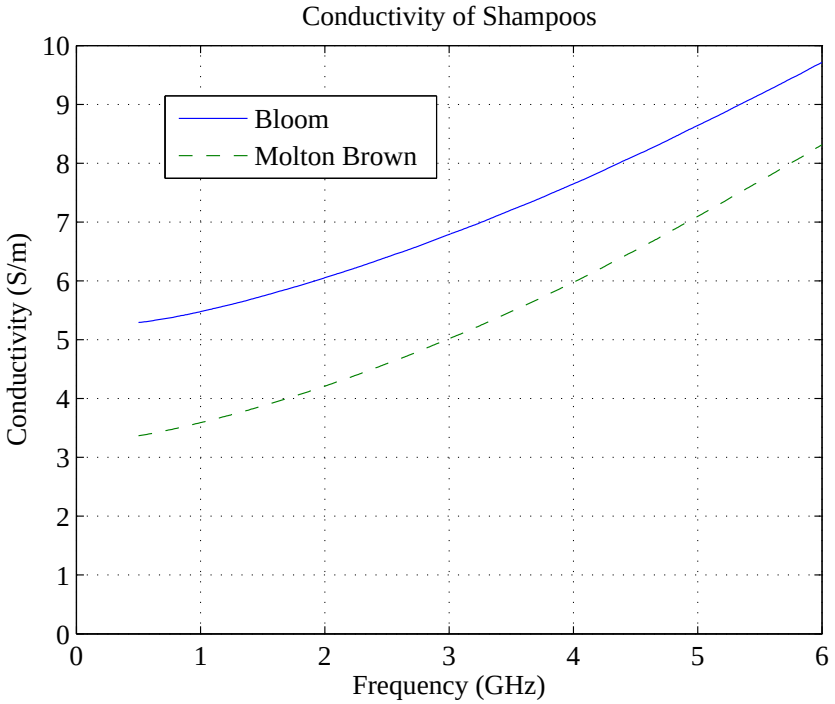

Figure 7.14: Conductivity [S/m] of commercially available hair shampoo

BIBLIOGRAPHY

BIBLIOGRAPHY

[1] "Screening for Breast Cancer: U.S. Preventive Services Task Force Recommendation Statement," *Annals of Internal Medicine*, U.S. Preventive Services Task Force, Nov. 2009, vol. 151, no. 10, pp. 726-737.

[2] X.Li and S. Hagness, "A confocal microwave imaging algorithm for breast cancer detection," *IEEE Microwave and Wireless Components Letters*, vol. 11, no. 3, pp. 130–132, Mar. 2001.

[3] M.Lazebnik, L. McCartney, D. Popovic, C. Watkins, M. Lindstrom, J. Harter, S. Sewall, A. Magliocco, J. Booske, M. Okoniewski, and S. Hagness, "A large-scale study of the ultrawideband microwave dielectric properties of normal breast tissue obtained from reduction surgeries," *Physics. Med. Biol.*, vol. 52.

[4] L. van Nieuwstadt and M. Moghaddam, "Imaging system sensitivity analysis based on an aggregate 3D T-Matrix model," *in preparation*.

[5] ——, "Planar UWB antenna for microwave imaging: Design and parametric dispersion study," *submitted August 2010*.

[6] J. Stang, L. van Nieuwstadt, and M. Moghaddam, "Clinical component of microwave breast cancer imaging: liquid coupling medium," *in preparation*.

[7] L. van Nieuwstadt and M. Moghaddam, "Microwave measurement system for breast cancer imaging: an experimental prototype," *in preparation*.

[8] "Screening for Breast Cancer: U.S. Preventive Services Task Force Recommendation Statement," *Annals of Internal Medicine*, U.S. Preventive Services Task Force, Nov. 2009, vol. 151, no. 10, pp. 716-726.

[9] C. Lee and *et. al.*, "Breast cancer screening with imaging: Recommendations from the society of breast imaging and the acr on the use of mammography, breast mri, breast ultrasound, and other technologies for the detection of clinically occult breast cancer," *American College of Radiology*, vol. 7, no. 1, pp. 18–27, Jan. 2010.

[10] C. Gabriel, S. Gabriel, and E. Corthout, "The dielectric properties of biological tissues: I. literature survey," *Physics. Med. Biol.*, vol. 41, pp. 2231–2249, Apr. 1996.

[11] S. Gabriel, R. Lau, and C. Gabriel, "The dielectric properties of biological tissues: II. measurements in the frequency range 10 hz to 20ghz," *Physics. Med. Biol.*, vol. 41, pp. 2251–2269, Apr. 1996.

[12] C. Gabriel, S. Gabriel, and E. Corthout, "The dielectric properties of biological tissues: III. parametric models for the dielectric spectrum of tissues," *Physics. Med. Biol.*, vol. 41, pp. 2271–2293, Apr. 1996.

[13] A. Campbell and D. Land, "Dielectric properties of female human breast tissue measured in vitro at 3.2 GHz," *Physics. Med. Biol.*, vol. 37, no. 1, pp. 193–210, June 1992.

[14] A. Surowiec, S. Stuchly, J. Barr, and A. Swarup, "Dielectric properties of breast carcinoma and the surrounding tissues," *IEEE Transactions on Biomedical Engineering*, vol. 35, no. 4, pp. 257–263, Apr. 1988.

[15] T. England, "Dielectric properties of the human body for wavelengths in the 1-10cm range," *Nature*, no. 166, pp. 480–481, Sept. 1950.

[16] S. Chaudhary and J. T. R.K. Mishra, A. Swarup, "Dielectric properties of normal and malignant breast tissue at radiowave and microwave frequencies," *Indian Journal of Biochemistry and Biophysics*, vol. 21, pp. 76–79, Feb. 1984.

[17] W. Joines, Y. Zhang, C. Li, and R. Jirtle, "The measured electrical properties of normal and malignant human tissues from 50 to 900 MHz," *Med. Phys. Journal*, vol. 21, no. 4.

[18] A. Rosen, M. Stuchly, and A. V. Vorst, "Applications of RF/Microwaves in medicine," *IEEE Transactions on Microwave Theory and Techniques*, vol. 50, no. 3, pp. 963–974, Mar. 2002.

[19] S. Poplack, T. Tosteson, W. Wells, B. Pogue, P. Meaney, A. Hartov, C. Kogel, S. Soho, J. Gibson, and K. Paulsen, "Electromagnetic breast imaging: Results of a pilot study in women with abnormal mammograms," *Radiology*, vol. 243, no. 2, pp. 350–359, May 2007.

[20] L. Sha, E. Ward, and B. Stroy, "A review of dielectric properties of normal and malignant breast tissue," in *Proceedings IEEE SoutheastCon*, 2002, pp. 457–462.

[21] P. Meaney, M. Manning, D. Li, S. Poplack, and K. Paulsen, "A clinical prototype for active microwave imaging of the breast," *IEEE Transactions on Microwave Theory and Techniques*, vol. 48, pp. 1841 – 1853, Nov. 2000.

[22] X.Li, S. Davis, S. Hagness, D. van der Weide, and B. V. Veen, "Microwave imaging via space-time beamforming: Experimental investigation of tumor detection in multilayer breast phantoms," *IEEE Transactions on Microwave Theory and Techniques*, vol. 52, no. 8, pp. 1856–1865, Aug. 2004.

[23] X.Li, E. Bond, B. V. Veen, and S. Hagness, "An overview of ultra-wideband microwave imaging via space-time beamforming for early-stage breast-cancer detection," *IEEE Antennas and Propagation Magazine*, vol. 47, no. 1, pp. 19–34, Feb. 2005.

[24] E. Bond, X. Li, S. Hagness, and B. V. Veen, "Microwave imaging via space-time beamforming for early detection of breast cancer," *IEEE Transactions on Antennas and Propagation*, vol. 51, no. 8, pp. 1690–1705, Aug. 2003.

[25] J. Bourqui, M. Campbell, J. Sill, M. Shenouda, and E. Fear, "Antenna performance for ultra-wideband microwave imaging," *IEEE Radio and Wireless Symposium RWS 2009*, pp. 522–525, Jan. 2009.

[26] E. Fear and M. Stuchly, "Microwave detection of breast cancer," *IEEE Transactions on Microwave Theory and Techniques*, vol. 48, no. 11, pp. 1854–1863, Nov. 2000.

[27] E. Fear, S. Hagness, P. Meaney, M. Okoniewski, and M. Stuchly, "Enhancing breast tumor detection with near-field imaging," *IEEE Microwave Magazine*, pp. 48–56, Mar. 2002.

[28] K. Carr, P. Cevasco, P.Dunlea, and J.Shaeffer, "Radiometric sensing: An adjuvant to mammography to determine breast biopsy," *IEEE Transactions on Microwave Theory and Techniques*.

[29] E. Fear, X. Li, S. Hagness, and M. Stuchly, "Confocal microwave imaging for breast cancer detection: Localization of tumors in three dimensions," *IEEE Transactions on Biomedical Engineering*, vol. 49, no. 8, pp. 812–822, Aug. 2002.

[30] P. Meaney, M. Manning, T. Reynolds, C. Fox, Q. Fang, C. Kogel, S. Poplack, and K. Paulsen, "Initial clinical experience with microwave breast imaging in women with normal mammography," *Acad Radiol.*, vol. 14, no. 2, pp. 207–218, Feb. 2007.

[31] P. Meaney, K. Paulsen, and J. Chang, "Near-field microwave imaging of biologically-based materials using a monopole transceiver system," *IEEE Transactions on Microwave Theory and Techniques*, vol. 46, no. 1, pp. 31–45, Jan. 1998.

[32] P. Meaney, K. Paulsen, A. Hartov, and R. Crane, "An active microwave imaging system for reconstruction of 2-D electrical property distributions," *IEEE Transactions on Biomedical Engineering*, vol. 42, no. 10, pp. 1017–1026, Oct. 1995.

[33] P. Kosmas and C. Rappaport, "Fdtd-based time reversal for microwave breast cancer detection - localization in three dimensions," *IEEE Transactions on Microwave Theory and Techniques*, vol. 54, no. 4, pp. 1921–1927, Apr. 2006.

[34] ——, "Time reversal with the FDTD method for microwave breast cancer detection," *IEEE Transactions on Microwave Theory and Techniques*, vol. 53, no. 7, pp. 2317–2322, July 2005.

[35] J. Stang, "A 3D active microwave imaging system for breast cancer screening," Ph.D. dissertation, Duke University, Durham, North Carolina, 2008.

[36] Q. Liu, Z. Zhang, T. Wang, J. Bryan, G. Ybarra, L. Nolte, and W. Joines, "Active microwave imaging I - 2-D forward and inverse scattering methods," *IEEE Transactions on Microwave Theory and Techniques*, vol. 50, no. 1, pp. 123–133, Jan. 2002.

[37] Z. Zhang, Q. Liu, C. Xiao, E. Ward, G. Ybarra, and W. Joines, "Microwave breast imaging: 3-D forward scattering simulation," *IEEE Transactions on Biomedical Engineering*, vol. 50, no. 10, pp. 1180–1189, Oct. 2003.

[38] Z. Zhang and Q. Liu, "Three-dimensional nonlinear image reconstruction for microwave biomedical imaging," *IEEE Transactions on Biomedical Engineering*, vol. 51, no. 3, pp. 544–548, Mar. 2004.

[39] D. Kurrant, E. Fear, and D. Westwick, "Tumor response estimation in radar-based microwave breast cancer detection," *IEEE Transactions on Biomedical Engineering*, vol. 55, no. 12, pp. 2801–2811, Dec. 2008.

[40] J. Sill and E. Fear, "Tissue sensing adaptive radar for breast cancer detection - experimental investigation of simple tumor models," *IEEE Transactions on Microwave Theory and Techniques*, vol. 53, no. 11, pp. 3312–3319, Nov. 2005.

[41] T. Williams, E. Fear, and D. Westwick, "Tissue sensing adaptive radar for breast cancer detection - investigations of an improved skin-sensing method," *IEEE Transactions on Microwave Theory and Techniques*, vol. 54, no. 4, pp. 1308–1314, Apr. 2006.

[42] M. Ali and M. Moghaddam, "3D time-domain nonlinear super-resolution microwave inversion technique for breast cancer detection," *IEEE Antennas and Propagation Society International Symposium AP-S 2008*, pp. 1–4, July 2008.

[43] W. Chew, J. Friedrich, and R. Geiger, "A multiple scattering solution for the effective permittivity of a sphere mixture," *IEEE Transactions on Geoscience and Remote Sensing*, vol. 28, no. 2, pp. 207–214, Mar. 1990.

[44] W. Chew, *Waves and Fields in Inhomogeneous Media*. New York: Van Nostrand Reinhold, 1990.

[45] R. Harrington, *Time-Harmonic Electromagnetic Fields*. New York: Wiley-Interscience, 2001.

[46] L. van Nieuwstadt and M. Moghaddam, "A microwave breast imaging system simulator and sensitivity analyses," in *IEEE URSI/APS Conference Proceedings*, June 2009.

[47] J. Auger and B. Stour, "A recursive centered T-matrix algorithm to solve the multiple scattering equation: numerical validation," *Journal of Quantitative Spectroscopy and Radiative Transfer*, no. 79-80.

[48] H. Schantz, *The Art and Science of Ultrawideband Antennas*. Artech House, 2005.

[49] D. Ghosh, A. De, M. Taylor, T. Sarkar, M. Wicks, and E. Mokole, "Transmission and reception by ultra-wideband (UWB) antennas," *IEEE Antennas and Propagation Magazine*, vol. 48, no. 5, pp. 67–99, Oct. 2006.

[50] M. Peyrot-Solis, G. Galvan-Tejada, and H. Jardon-Aguilar, "State of the art in ultra-wideband antennas," in *2nd International Conference on Electrical and Electronics Engineering (ICEEE) and XI Conference on Electrical Engineering (CIE 2005)*, Mexico City, Mexico, 2005, pp. 101–105.

[51] H. Schantz, "Planar elliptical element ultra-wideband dipole antennas," *IEEE Antennas and Propagation Society International Symposium*, vol. 3, pp. 44–47, June 2002.

[52] N. Azenui and H. Yang, "A printed crescent patch antenna for ultrawideband applications," *IEEE Antennas and Wireless Propagation Letters*, vol. 6, pp. 113–116, 2007.

[53] C. Ying and Y. Zhang, "Integration of ultra-wideband slot antenna on LTCC substrate," *Electronics Letters*, vol. 40, no. 11, May 2004.

[54] U. Bombale and S. Gupta, "Design of ultra wideband microstrip antenna," in *IEEE Antennas and Propagation Society International Symposium*, 2006, pp. 3705–3708.

[55] S. Zhong and X. Liang, "Progress in ultra-wideband planar antennas," *Journal of Shanghai University*, vol. 11, no. 2, pp. 95–101, 2007.

[56] A. Mehdipour, K. Mohammadpour-Aghdam, and R. Faraji-Dana, "A new planar ultra wideband antenna for UWB applications," *IEEE Antennas and Propagation Society International Symposium*, pp. 5127–5130, 2007.

[57] S. Nikolaou, G. Ponchak, J. Papapolymerou, and M. Tentzeris, "Conformal double exponentially tapered slot antenna (DETSA) on LCP for UWB applications," *IEEE Transactions on Antennas and Propagation*, vol. 54, no. 6, pp. 1663–1669, June 2006.

[58] K. Aghdam, R. Faraji-Dana, and J. Rashed-Mohassel, "Compact dual-polisation planar log-periodic antennas with integrated feed circuit," *IEEE Proceedings on Microwave Antennas Propagation*, vol. 152, no. 5, pp. 359–366, Oct. 2005.

[59] R. Olsson, P. Kildal, and S. Weinreb, "The eleven antenna: A compact low-profile decade bandwidth dual polarized feed for reflector antennas," *IEEE Transactions on Antennas and Propagation*, vol. 54, no. 2, pp. 368–375, Feb. 2006.

[60] A. Papió-Toda, W. Sorgel, J. Joubert, and W. Wiesbeck, "UWB antenna transfer property characterization by FDTD simulations," *IEEE 2nd International ITG Conference on Antennas, INICA 2007*, pp. 81–85, 2007.

[61] N. Hecimovic and Z. Marincic, "The improvements of the antenna parameters in ultra-wideband communications," *IEEE*.

[62] I. Bahl, S. Stuchly, and M. Stuchly, "A new microstrip radiator for medical applications," *IEEE Transactions on Microwave Theory and Techniques*, vol. 12, no. MTT-28, pp. 1464–1468, Dec. 1980.

[63] H. Kanj and M. Popović, "Miniaturized microstrip-fed 'dark eyes' antenna for near-field microwave sensing," *IEEE Antennas and Wireless Propagation Letters*, vol. 4, pp. 397–401, 2005.

[64] X. Li, S. Hagness, M. Choi, and D. van der Weide, "Numerical and experimental investigation of an ultrawideband ridged pyramidal horn antenna with curved launching plane for pulse radiation," *IEEE Antennas and Wireless Propagation Letters*, vol. 2, no. 1, pp. 259–262, 2003.

[65] Khaleghi, *IEEE Microwave*, Oct.

[66] A. Alomainy, A. Sani, A. Rahman, J. Santas, and Y. Hao, "Transient characteristics of wearable antennas and radio propagation channels for ultrawideband body-centric wireless communications," *IEEE Transactions on Antennas and Propagation*, vol. 57, no. 4, pp. 875–884, Apr. 2009.

[67] J. Tyo, "Self-compensating antenna concept for a dispersionless UWB propagation channel," *IEEE Transactions on Antennas and Propagation*, vol. 56, no. 5, pp. 1491–1494, May 2008.

[68] M. Armanious and J. Tyo, "UWB self-compensating antennas: Numerical demonstration of the electromagnetic working principle," *submitted to IEEE*, Oct. 2009.

[69] H. Schantz, "Dispersion and UWB antennas," *Proceedings 2004 International Workshop on Ultra Wideband Systems*, pp. 161–165, May 2004.

[70] E. Madsen, G. Frank, T. Krouskop, T. Varghese, F. Kallel, and J. Ophir, "Tissue-mimicking oil-in-gelatin dispersions for use in heterogeneous elastography phantoms," *Ultrasonic Imaging*, vol. 25.

[71] E. Madsen, M. Hobson, G. Frank, H. Shi, J. Jiang, T. Hall, T. Varghese, M. Doyley, and J. Weaver, "Anthropomorphic breast phantoms for testing elastography systems," *Ultrasound Med. Biol.*, vol. 32, pp. 857–874, June 2006.